ABSTRACT

KOLANJIYIL, ARUN VARGHESE. Deposited Nanomaterial Mass Transfer from Lung Airways to Systemic Regions. (Under the direction of Dr. Clement Kleinstreuer).

Particle retention and clearance is a major concern in the treatment of pulmonary diseases. Inhaled materials into the nasal and lung airways include gases/vapors, liquid droplets and soluble/insoluble particulate matter which can be toxic or therapeutic (or both). For example, nanoparticles (NPs), as part of nanomedicine, are now being used as drug carriers for passive and active targeting of solid tumors and inflamed tissue. However, natural and especially manmade NPs can also be harmful, such as carbon nanotubes (CNTs), asbestos fibers and ambient toxic pollutants, based on epidemiological and pathological studies of occupational and environmental exposures. In fact, ultrafine particles have been found to pose a higher toxicity impact than larger particles made of the same material, mainly due to the more uniform deposition patterns in lung airways and easier migration across several barriers into the systemic system.

Thus, investigations related to the deposition and removal of inhaled nanomaterial are of great importance because accumulation and retention of toxic NPs can result in serious lung diseases, e.g., chronic bronchitis, lung fibrosis, silicosis, asbestosis, lung cancer, etc. In case of polymeric nanostructures for disease detection, imaging and drug targeting, a thorough knowledge base of multifunctional nanoparticle formulation, delivery and uptake is crucial as well. Mathematical models and associated computer simulations, which can predict realistic particulate lung burden for specific parameters of exposure conditions, can offer valuable assistance in developing new preventive strategies. Optimal drug-aerosol targeting requires suitable physical drug-particle characteristics, appropriately controlled delivery to a

predetermined site, and an accurate assessment of the deposited medicine. Given realistic local (or regional) NP-depositions, computer simulations of nanomaterial transfer from the lung airways ultimately into organs (or tumors) are important for both application areas.

In this study a multi-compartmental model representing the bio-kinetics of nanoparticle translocation and retention in key segments of the human lung as well as connected tissue and vasculature was created. The model describes via a set of differential equations the transfer of nanomaterial between compartments, i.e., lung airway, mucus layer, epithelial barrier, capillaries, arteries, and organs. The initial deposition of nanoparticles in key segments of the human lung and upper airways was calculated using Computational Fluid-Particle Dynamics.

This study provides critical insight into nanomaterial deposition in lung airways and distribution to systemic regions from lungs. The results of this study can be used in fields like toxicology and pharmacology, to analyze risk to a given nanomaterial exposure and assist in developing new pulmonary drugs.

Deposited Nanomaterial Mass Transfer from Lung Airways to Systemic Regions

by
Arun Varghese Kolanjiyil

A thesis submitted to the Graduate Faculty of
North Carolina State University
in partial fulfillment of the
requirements for the degree of
Master of Science

Mechanical Engineering

Raleigh, North Carolina

2013

APPROVED BY:

_____
Dr. Clement Kleinstreuer
Committee Chair

_____ _____
Dr. Tarek Echekki Dr. Yun Jing

DEDICATION

I dedicate this thesis to my parents for their

unconditional love and support.

BIOGRAPHY

Arun Varghese Kolanjiyil was born on 2 June 1987 in Kerala, India. He completed his schooling at the Sobhana School, Kothamangalam and his secondary schooling from Mar Basil HSS, Kothamangalam. He attended the Mahatma Gandhi University, Kerala, India, for his undergraduate studies and earned a Bachelor of Technology (B.Tech) in Mechanical Engineering in May 2009. He enrolled in the graduate program in Mechanical Engineering in the Department of Mechanical and Aerospace Engineering at North Carolina State University in Raleigh, NC in fall 2010.

ACKNOWLEDGMENTS

First and foremost, I would like to express my deep gratitude to my advisor, Dr. Clement Kleinstreuer, for his encouragement, guidance, and support throughout my graduate study. This work has been possible only due to the enormous support and patience provided by him.

I would also like to express my gratitude to Dr. Tarek Echekki and Dr. Yun Jing for taking time from their schedule to be a part of my thesis committee.

I would like to take this opportunity to thank the people who have helped me in various ways during my work on this master's thesis. First of all I would like to thank Dr. Zhe Zhang, Dr. Jie Li, Emily Childress, Yu Feng, Luke Xu and Tejas Umbarkar for all the help, support and explanations. I am very thankful to my friends who have been very supportive and accommodating.

I would like to thank my family for all their support throughout my education, with special thanks to my beloved parents for their love, advice and financial support.

I thank the ALMIGHTY for having bestowed the blessings on me.

TABLE OF CONTENTS

LIST OF TABLES

LIST OF FIGURES

ABBREVIATIONS AND SYMBOLS

ρ	Density
ρ_s	Density of the solid
ω	Pseudo-vorticity
ν	Kinetic viscosity
μ	Dynamic viscosity
λ	Mean free path
σ_Y	Turbulent Schmidt number
σ_{ij}^s	Stress tensor
ε_{kl}	Strain matrix
AM	Alveolar macrophages
BW	Body weight
C_C	Cunningham correction factor
C_{lim}	Clip factor
CFPD	Computational Fluid Particle Dynamics
d	Distance from the field point to the nearest wall
d_p	Particle diameter
D	Diffusion constant
DBU	Double Bifurcation Unit
DE	Deposition Efficiency
DF	Deposition fraction

E_{ijkl}	Elasticity tensor
ICRP	International Commission on Radiological Protection
$j_{wall,i}$	Particle flux at the local wall cell
k	Turbulence kinetic energy
k_B	Boltzmann constant
LRN	Low Reynolds number
MPPD	Multiple Path Particle Dosimetry
MSE	Mean Square Error
NP	Nanoparticles
P	Pressure
POCK	Physiology Oriented Compartmental Kinetics
RANS	Reynolds-Averaged Navier-Stokes
t	Time
TB	Tracheobronchial region
TBU	Triple Bifurcation Unit
TKE	Turbulent Kinetic Energy
u	Velocity
$\bar{u}_i$	Time-averaged velocity
u_i	Velocity vector (same for uj)
Y	Mass fraction
Yin	Inhaled particle concentration

CHAPTER 1
INTRODUCTION AND LITERATURE REVIEW

1.1 Introduction

Inhalation carries gases, liquid droplets and soluble and insoluble particulate materials in to the lung airways. Some material can be useful, for example when aerosol droplets containing inflammation-reducing steroids are inhaled to treat asthma. Unfortunately, they can also be harmful, such as when asbestos fibers (or other toxic materials) are inhaled by workers. Removal of these aerosols from the lungs depends mainly on the degree of exhalation as well as the chemical properties and physical structure of the aerosols. If it is a gas or a liquid, clearance process depends on solubility, but removal of a solid particle mostly depends on the diameter. Also different regions of the lungs have different removal mechanisms. Elimination of the deposited soluble and insoluble particles from the respiratory tract is necessary to keep its mucosal surfaces clean and functionally intact. Studies related to particle deposition and removal from the lung are of great importance since accumulation and retention of these particles can result in serious lung diseases like chronic bronchitis, lung fibrosis, silicosis, asbestosis, lung cancer etc. Mathematical models and associated computer simulations which can predict possible particulate lung burden for specific parameters of exposure conditions can offer valuable assistance in developing preventive strategies. Also these models could be used in developing new concepts for pulmonary administration of drugs.

1.2 Lung structure

The lung is similar to a tree. The structure of a tree comprises of bark, branches and leaves. The airways (trachea, bronchi, and bronchioles) are analogous to the bark and branches of the tree and the air-sacs or alveoli are analogous to the leaves of the tree. Like the tree, the branches of the lung have thick walls, and the alveoli have thin walls. Also like the tree, the thickness of the airway gets thinner and thinner as they approach the alveoli. The surface area of the branching system is small compared to the gas exchange surface. Air enters through the mouth or nose then passes through (in order): the pharynx (the throat), the larynx (the voice box), and the trachea (the wind pipe). The trachea splits to form two bronchi each of which feed air to one of the lungs. Each bronchus splits to form bronchioles, which, in turn, split to form smaller bronchioles, and so on. Bronchioles extend about 16 levels of branching, reach the terminal bronchioles. After the terminal bronchioles there are several generations of respiratory bronchioles, alveolar ducts and alveolar sacs, which collectively are known as the acinus. Acinus is the region where gas exchange occurs. The airways other than acinus have a mucous layer over the ciliated epithelium. Mucus layer composed of a sol phase of low viscosity (hypo-phase) in which the cilia beat, and a blanket of an overlaying gel phase of high viscosity (epi-phase) which is thought to be moved by ciliary motion towards the pharynx.

Alveoli are the smallest unit in the lung and there are approximately 300 million of them in each lung. Although alveoli are tiny structures, they have a very large surface area in total (~100 m^2) for performing efficient gas exchange. The lungs are supplied by the pulmonary

arteries and drained by the pulmonary veins. The smallest units of the pulmonary vasculature are the pulmonary capillaries. The blood barrier between the alveolar space and the pulmonary capillaries is a very thin layer of tissue, consisting of capillary endothelial cells, basement membrane, and airway epithelial cells. This thin layer easily allows rapid gas exchange. During inspiration, oxygen diffuses through the alveoli walls and the interstitial space, into the blood. Carbon dioxide diffuses in the opposite direction during exhalation.

1.3 Overview of clearance mechanisms

In the tracheobronchial region the clearance process is mainly due to the mucociliary movement. The region consists of a ciliated epithelium with a mucous layer on top of it. This layer is composed of a sol phase of low viscosity in which the cilia beat, and a overlaying gel phase of high viscosity which is thought to be moved by ciliary motion towards the pharynx. Soluble particles depositing in the tracheobronchial tree are mainly cleared by absorptive mechanisms. Clearance of insoluble particles depositing in the tracheobronchial region occurs through phagocytosis by airway macrophages. Another clearance mechanism for insoluble particles is penetration of particles of submicron size through the epithelium, very likely due to endocytosis by epithelial cells of the conducting airways. Another efficient clearance mechanism in the upper generations of the conducting airways is cough.

Smaller particles may not be stopped by the mucous in the trachea and bronchi as they travel through the various branches of the airways and eventually reach the alveoli. Aerosols that reach the inner smaller airways and alveolar region are cleared by transferring to the blood and lymph capillaries or by phagocytosis by alveolar macrophages. Soluble substances are

cleared by inter-cellular and trans-cellular diffusional transport through alveolar epithelial cells to the blood capillaries. The rates at which these absorptive processes occur are controlled by the lipophilicity and hydrophilicity of the solutes and their molecular size. Insoluble particles are removed mainly by phagocytosis by alveolar macrophages. These alveolar macrophages which have phagocytized insoluble particles will move upwards to the ciliated airways from where particles are removed by mucociliary escalation process. Some alveolar macrophages carry the particles to the lymphatic capillaries. We do not have a clear understanding regarding the movement of phagocytized alveolar macrophages. Smaller insoluble particles diffuse through the alveolar epithelium to reach the interstitium. These particles will be phagocytized by the lymphatic endothelium and transferred to the lymphatic capillaries. Most of the foreign particles in the lymphatic capillaries will be filtered out and retained at the regional lymph nodes. Those particles which are not filtered out will penetrate the lymph node to the blood circulation leading to a widespread systemic distribution. Many of the insoluble particles after getting phagocytized by the alveolar macrophages dissolve due to the low PH level (Lundborg et al., 1984). Thus, many solid particles are cleared from the lungs involving mechanisms for solutes.

1.4 Journal review

1.4.1 Micron and sub-micron particle clearance

Several recent review articles provide detailed descriptions and discussions of different processes governing the removal of inhaled solid and solute particles after deposition in the respiratory tract. Particle clearance in the tracheobronchial (TB) region may occur by various

mechanisms including mucociliary transport, coughing, penetration into epithelium, or phagocytosis. As mentioned earlier, the most effective way of removing particles from the tracheobronchial region is by mucous escalator (Albert et al., 1969). Mucociliary transport or escalation is the transport of foreign material deposited on the lung airway surfaces by a layer of mucous that covers the walls of the conducting airways of the lung. The constant beat of the cilia forces the mucous layer to move up against gravity to the glottis from where it will be swallowed to gastrointestinal tract or will be removed by coughing (Basser et al., 1989). Mucociliary transport rates are highly variable through the ciliated airways. Clearance rates are high for larger airways with more number of cilia than less ciliated smaller airways (Hilding et al., 1957; 1961; Aasmundsson et al., 1970). The rate of mucous transport also depends on the viscosity, elasticity, and depth of the upper viscoelastic layer and the viscosity and depth of the peri-ciliary layer (Ross et al., 1974). Iravani and Van (1972) suggested a discontinuous layer of mucous and the thickness reduces from trachea towards the terminal bronchioles. The thickness of the mucous layer varies by location in the conducting airways, from $8.3\mu m$ in thickness in the trachea to about $1.8\mu m$ in small bronchioles (Mercer, Russell, & Crapo, 1992). There are many conflicting views on the continuity of the thickness of the mucous layer. Mercer, Russell, & Crapo, (1992) found that the mucous layer to be continuous in larger human bronchial airways, but consisting of discontinuous patches in smaller bronchi and bronchioles. Moreover, their results suggest that the mucous layer in most bronchial airways is covered by a surfactant lining layer similar to that in the alveolar region.

Soluble particulates, depending on their physicochemical properties, may either be incorporated into the mucous, be taken up by the airway epithelium, or pass through it to be cleared by the bronchial and pulmonary circulations. It has been suggested that some insoluble particles (sub-micron) may penetrate the mucous and enter epithelial cells (Brain et al., 1977). Experimental studies conducted by Patrick & Stirling (1977), Patrick et al., (1979), Gore & Patrick (1978), Watson and Brain (1979) suggested that deposited particles may penetrate the tracheobronchial (TB) airway epithelium and stay there for periods longer than 30 days. But the number of particles removed by this process is less than 1% of the total particle deposited. Also it depends on the size of the particle. For smaller particles the penetration will be much easier than for larger particles. So as the size of the particle reduces the number of particle penetrating the epithelium will be higher.

There are many models which predict the particle removal by mucociliary escalation. In the earlier stages of lung clearance model development, many used mathematical models which predict the TB clearance using a simplified symmetric lung model (Lee et al., 1979; Hofmann & Daschil 1986; Yu et al., 1986; Cuddihy & Yeh 1988; Gradon & Porgorski 1992). Yu et al., (1986) modeled clearance in the TB-region as the movement of an escalator clearing the deposited material from one generation to the next. Particles deposited in the first generation cleared first and those in the terminal airway generation cleared last after traveling through all the more proximal generations. Using a retention curve, a clearance rate and mucous velocity was obtained for each airway generation. Cuddihy and Yeh (1988) constructed a cumulative deposition-per-generation curve along with a retention curve for the TB region to calculate the clearance time of deposited particles in each airway generation of

the human conducting tree. Mucous velocities were then calculated by dividing the airway length in each generation by the clearance time for that generation. Asgharian et al., (2001) used an asymmetric stochastic lung model to predict the TB clearance. They calculated the mucous velocities in all conducting airways from the principle of mass balance for the mucus. These velocities were used to calculate particle residence time in all the airways of the conducting tree. Smith et al., (2006) developed a viscoelastic traction layer model in which the mucus was represented by a linearly viscoelastic fluid, the mat of cilia was modeled as an 'active porous medium'. The propulsive effect of the cilia was modeled by a time-dependent force acting in a shear-thinned 'traction layer' between the mucus and the periciliary fluid. Sturm et al., (2006) developed a multi-compartment model for the clearance of insoluble particles from the tracheobronchial tree of the human lung. He developed compartments for accumulation of particulate mass in the periciliary sol layer and gel layer, an uptake of stored particles by airway macrophages and the endocytosis of deposited mass by epithelial cells. The particles where transferred and accumulated finally in gastrointestinal tract, lymph nodes, and blood capillaries.

Aerosols that reach the inner smaller airways and alveolar region are cleared by transferring to the blood and lymph capillaries or by phagocytosis by alveolar macrophages (AM). The most effective clearance mechanism for insoluble particles in the alveolar region is phagocytosis by alveolar macrophages (Morrow et al., 1973; Brain et al., 1986, 1988). These alveolar macrophages which have phagocytized insoluble particles will move upwards to the ciliated airways from where particles are removed by mucociliary escalation process (Harmsen et al., 1985). Some alveolar macrophages carry the particles to the lymphatic

capillaries (Snipes, Chavez, Muggenburg et al., 1984). Some smaller insoluble particles diffuse through the alveolar epithelium to reach the interstitium. Endocytosis by alveolar epithelium and subsequent exocytosis to the interstitium is another way of removing insoluble particles from the alveoli. Once they have reached the interstitium, several mechanisms can contribute to their further removal. These include phagocytosis by interstitial macrophages (IM), endocytosis and luminal exocytosis of small ($< 0.1\mu m$) particles by endothelial cells of the lymph and blood capillaries (Morrow et al., 1972). The rate of phagocytosis depends on particle size, with an optimum size around 1.5-3 μm and a slower rate of phagocytosis occurring for smaller and for larger particles (Hahn et al., 1977). Most of the foreign particles in the lymphatic capillaries will be filtered out and retained at the regional lymph nodes (Morrow et al., 1972). Those particles which are not filtered out will penetrate the lymph node to the blood circulation leading to a widespread systemic distribution (Oberdörster et al., 1988).

Sanchis et al., (1972) measured the removal of aerosol droplets (radioactive human serum albumin) of aerodynamic mass median diameter 3μm from the lung. The radioactivity of serum albumin was captured using a scintillation camera interfaced to a data collection system. They divided the lung to perihilar, intermediate and peripheral zones based on the mucociliary activity. The perihilar region includes the larger airways with the fastest mucociliary clearance rate. The intermediate zone includes the ciliated and non-ciliated airways other than the larger airway. The peripheral region includes non-ciliated lung (alveolar region) and small ciliated airways. They presented the aerosol removal data in terms of clearance curves for each zones. Also they postulated that deposition of particles

with diameter smaller than 4μm, mainly takes place in the peripheral airways and alveoli. Experimental observations by Altshuler et al., (1967); Albert & Lippmann (1969); Morrow et al., (1970); Newhouse et al., (1970) support similar particle diameter dependency theory on deposition patterns. Snipes et al., (1983) measured the clearance rate of radioactive Aluminosilicate particles over 700 days. They noticed that the retention half times increased with time. A similar prolongation in retention halftimes in rats with time was reported by Bailey et al., (1985a), with halftimes of 32 days in the early phase of clearance and of 173 days after one year. Clearance curves were developed from these retention data by separating each phases in time. Cuddihy and Yeh (1988) proposed a mathematical model which makes use of variable clearance rates that are expressed in terms of the remaining fractions of the lung tissue burdens. They suggested that the mechanical clearance rates for insoluble particles in man vary as an exponential curve. After the initial rapid clearance the clearance rate approaches a constant like an exponential curve. Toxicity and lung burden are two important factors which affect the alveolar particle clearance. Biologically toxic materials like silica, asbestos could lead to impairment of alveolar macrophages. Also high concentration of insoluble particles results in lung burden which can lead to significant retardation of particulate lung clearance. For example, it was reported that the elimination of particles from the alveolar compartment was decreased in rats exposed chronically to high concentrations of TIO_2 particles (Bellmann et al., 1986; Muhle et al., 1988). Ferin et al., (1977) reported increased amount of particulate matter in the lymph capillaries at high lung particle concentration. Retardation of clearance process due to lung burden does not depend on the material property of the particulate matter. So a threshold concentration of particulates

can be calculated above which the effects of “overloading” occur. This concentration seems to be above 1 mg of dust per gram lung tissue (Bolton et al., 1983; Morrow and Mermelstein, 1988). Morrow (1988) postulated that the phagocytized alveolar macrophages can impair the phagocytizing process under conditions of lung overload. According to this hypothesis, a maximum phagocytized volume would incapacitate AM movement. He suggested that this volume is about 60% of the normal macrophage volume. It was noticed that after the threshold lung mass burden, the particle accumulation had increased linearly and the particle removal rate had dropped down linearly. Morrrow (1988) described this maximum phagocytized volume of particles as the "volumetric limit" of the AM. Also it has been noted that in humans, high lung burden results in reduction in particle clearance which eventually leads to lung fibrosis. Freedman and Robinson (1988) found that in coal workers a decreased clearance of the inhaled coal dust is an effect of chronic exposure. Cytotoxic materials like asbestos and silica can create the same pathologic features (called ‘asbestosis and silicosis’) of lung burden with less amount.

Many researchers have tried to formulate a model which can explain the overload related clearance phenomena. Yu and Morrow (1987) created a nonlinear mathematical model in which the clearance rate is a function of mass burden in the lung. Smith et al., (1985) proposed a bio-mathematical model for predicting the clearance of insoluble particles from the inner lung. He assumed that the particle clearance from the alveolar region by macrophages follows a form of Michaelis-Menten kinetics. He experimentally verified the independency of macrophage clearance rate at high particle concentration rate. This model was specifically developed for describing the clearance kinetics of quartz particles and the

related development of fibrosis. Strom et al., (1988) modeled the overload effects by introducing a sequestration compartment represented by aggregated AM with a very long retention halftime. The contents of the sequestration compartment within the pulmonary region would not be transferred to other compartments. So as the lung burden increases the amount of particle trapped inside the sequestration compartment increases. Stober et al., (1989) used a multi-compartmental model to define the various clearance processes. They defined specific compartments for overload (sequestration compartment) and free particle (release from dying AM with subsequent re-phagocytosis). Katsnelson et al., (1992) developed a multi compartmental model for the kinetics of dust retention in the pulmonary region of the lung and in the tracheobronchial lymph nodes. They considered the neutrophil clearance and transfer of particles to mucociliary airways through inner lymph capillaries. Trans et al., (1999) developed a compartmental model similar to that of Stober et al., (1989). Besides the alveolar macrophage clearance pathway they also considered the interstitial macrophage clearance pathway in their model. An improved multi-compartmental model was developed recently by Gregoratto et al., (2010). In this model they used two alveolar compartments with more interstitial particle sequestration instead of the usual three alveolar compartmental model (called Human Respiratory Tract Model-HRTM) developed by International Commission on Radiological Protection (ICRP).

1.4.2 Ultrafine particle clearance

Inhalation of fine particulates in the atmospheric air especially nanoparticles have reported to produce adverse health problems. Deposition, retention and clearance of ultrafine particles

are different from that of micro level particles (see Fig. 1.1). As previously mentioned phagocytosis by AM depends on the size of the particle. Studies have shown that ultrafine particles are not easily phagocytized by AM and the situation can lead to lung overload. In such cases, referred to as particle "overload," it is conceivable that activated AM release excessive amounts of mediators that are subsequently involved in the pathogenesis of acute and chronic lung injury. These injuries include fibrosis and even lung tumors (Oberdörster et al., 1992). Also in these situations an excessive amount of particles have been spotted in the interstitial spaces and lymphatic capillaries. Such interstitialization is likely to depend on the size of the particles and on the particulate lung burden (Ferin and Feldstien, 1978). Ferin, Oberdörster and Penney, (1992) reported that particles that are not phagocytized by AM are taken up by the type I epithelial cells and then enter the pulmonary interstitium, and that with increasing numbers of particles deposited, the entry of particles into the interstitium increases. Some of the particles are phagocytized from the interstitial space by interstitial macrophages and some are absorbed in to the lymphatic system. Ferin and Oberdörster (1992) proposed another clearance pathway involving macrophages for interstitialized particles. According to this postulate particle laden interstitial macrophages move through interstitial spaces and the lymphatics, and enter the lumens of the airways at the junctions of respiratory and terminal bronchioles. Semmler et al., (2004 and 2007) found evidence for transfer of nanoparticles from alveolar epithelial surface to interstitial space. Also they hypothesized that the increased fraction of nanoparticle concentration in the rat excretion was due to the nanoparticle transport to the larynx from the nanoparticle fraction being re-entrained from the interstitium to the luminal side of the airway epithelium. Kreyling et al.,

(2002) found that ultrafine poorly soluble ^{192}Ir particles were predominantly retained in the rat lungs during the first week after inhalation. The nanoparticles deposited in thoracic airways and lung peripheries were cleared predominantly via airways and larynx into the gastrointestinal tract (GIT) and feces. Nemmar et al., (2001) exposed human subjects by inhalation to 99*m*Tc-labeled ultrafine carbon particles (Technegas) and observed translocation of 99*m*Tc into the blood compartment. Studies conducted on rats by Oberdörster et al., (2002) with intravenously injected ultrafine particles have shown that the liver is the major organ of their uptake from the blood circulation. Takenaka et al., (2003) had shown that ultrafine Ag particles translocated from the luminal side into and beyond the epithelial membrane of the lung, including uptake in type I epithelial cells, endothelial cells, and the alveolar septum. According to current knowledge, nanoparticles translocation and accumulation in extra-pulmonary organs like liver, heart, brain is less compared to macrophage mediated nanoparticle clearance towards the larynx. Yet, while the latter pathway leads to particle excretion via the gastro-intestinal tract, nanoparticle translocation into the blood circulation systemically distributes nanoparticles and allows access to the cardio-vascular, the central-nervous and the immune systems (Kreyling and Geiser 2010).

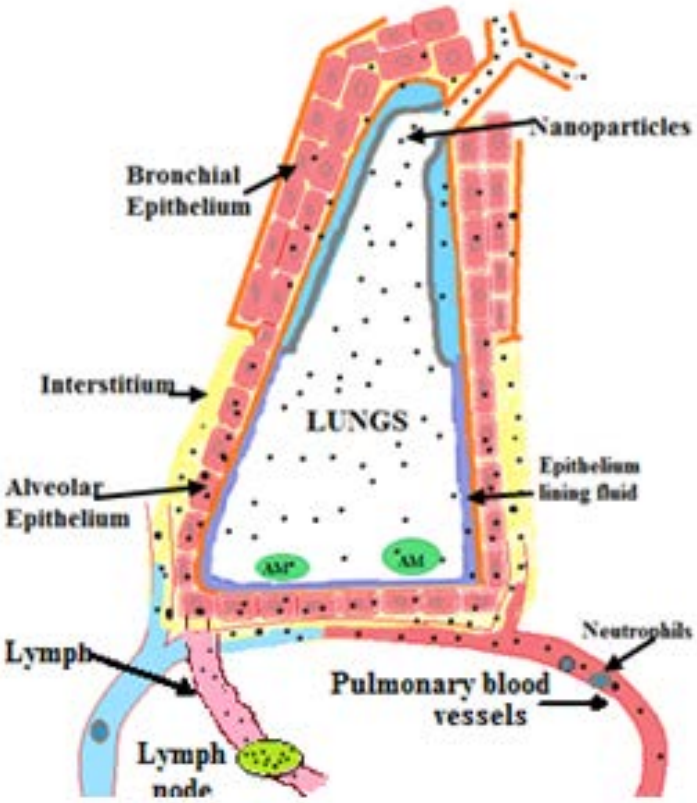

Fig. 1.1. Pictorial representation of clearance of ultrafine particles from lung airways

1.5 Summary

In the tracheobronchial region the clearance process is mainly due to the mucociliary movement. Another significant clearance process is phagocytosis by airway macrophages which are either alveolar macrophages (AM) moving up with the mucociliary escalator or macrophages entering through the airway mucosa. Smaller particles may not be stopped by the mucous in the trachea and bronchi as they travel through the various branches of the airways and eventually reach the alveoli. Aerosols that reach the alveolar region are cleared by transferring to the blood and lymph capillaries or by phagocytosis by AM. The primary role of AM, to protect the lung from inhaled substances, may be reversed in situations when high particulate burdens are deposited and accumulate in the lung. One characteristic finding in such situation is serious retardation of AM-mediated particle clearance with an increase of particles in the interstitial space of the lung. Inhalation of fine particulates present in the atmospheric air especially nanoparticles have reported to produce adverse health problems. Studies have shown that ultrafine particles are not easily phagocytized by AM and the situation can lead to lung overload. Also ultrafine particles enter the interstitium more readily than larger-sized particles of the same chemical composition. Ultrafine particles can easily translocate from deposition sites in the lungs to systemic circulation and accumulate in extra pulmonary organs like liver, heart etc. Studies suggest an inverse particle-size-dependent transport phenomenon into blood circulation. Also it can be hypothesized from the studies that AM-mediated nanoparticle transport to the larynx originates not only from the nanoparticle fraction retained on the epithelium but also from nanoparticles being re-entrained from the interstitium to the luminal side of the airway epithelium.

1.6 Research objectives and Novel Contributions

The objectives of this study are:

- To analyze the airflow and nanoparticle distribution through upper airway and lung airways using Computational Fluid-Particle Dynamics (CFPD).
- To calculate the nanoparticles deposition fractions in key segments of the airways using CFPD.
- To identify important mechanisms of nanoparticle clearance from lungs and upper airways and develop a multi-compartment model representing the bio-kinetics of deposited nanoparticles.
- Estimate the parameters for the multi-compartment model based on retention and clearance data in rat lung.
- Extrapolate the results to human scenario using body weight scaling.
- Apply CFPD deposition results to the newly developed multi-compartment model for human lungs.

1.7 Novel Contributions

The novel contributions from this study are

- The airflow and nanoparticle distribution through upper airway and lung airways were analyzed using Computational Fluid-Particle Dynamics (CFPD). The nanoparticle deposition results were compared with the experimental and analytical

results. The CFPD results were found to agree better with the experimental results than the analytical results.

- The CFPD method for calculating the nanoparticle deposition fractions in key segments of the lung airway is proposed.
- The important mechanisms of nanoparticle clearance from lungs and upper airways were identified and a multi-compartment model was developed representing the bio-kinetics of deposited nanoparticles.
- The multi-compartment model parameters were estimated based on experimental retention and clearance data in rat lung.
- The multi-compartment model for a human was developed using pharmacokinetic cross species extrapolation.
- The model simulation for an exposure to a normal nanoparticle ambient air concentration shows that there can be severe health hazard due to the translocation of nanoparticles to other vital organs from lungs through blood circulation system.
- The multi-compartment model can be used in the field of toxicology to estimate risk to any nanoparticle exposure.
- The multi-compartment model can be used in the field of pharmacology to study the effects of new pulmonary drugs. The retention time in the lung and the amount of nanomaterial translocated to other internal organs are vital data required for any new drug testing.

PART 1

PREDICTION OF LUNG NANOPARTICLE DYNAMICS AND DEPOSITION USING COMPUTATIONAL FLUID-PARTICLE DYNAMICS

CHAPTER 2
INTRODUCTION TO LUNG FLUID DYNAMICS

2.1 Introduction

Computational fluid dynamics (CFD) has been found to be a very useful tool in predicting lung aerosol dynamics especially when the aerosols are toxic. CFD simulations can drastically reduce the time and costs that are associated with the experimental study and can predict realistic features of airway flow and particle deposition patterns including hot spots. The deposition of micro and nanoparticles throughout the nasal, oral and respiratory airways has been considered in many experimental and numerical studies. But the sheer complexity in predicting particle dynamics in a complete tracheobronchial tree has defied detailed study. The objective of this study is to evaluate the transport and deposition of nanoparticles in lung airways. In this study, in order to reduce the geometrical complexity of the lung airway tree, it was geometrically decomposed to 'Triple Bifurcation Unit' (TBU) models. The transport and deposition of 37 nm and 17 nm particles were analyzed and deposition fractions in individual lung sections were calculated.

Most of the lung CFD simulations are based on respiratory airways approximated as a network of repeatedly bifurcating tubes with progressively decreasing dimensions (Weibel lung model, 1963). Balashazy and Hoffmann, (1995) simulated aerosol deposition in an asymmetric airway bifurcation under steady inspiratory and expiratory flow conditions. In another study, Balashazy et al., (1996) analyzed the effects of different geometric models on airflow and particle deposition patterns on a bronchial airway bifurcation. Balashazy et al., (1999) simulated the enhanced deposition of particles in the vicinity of bifurcation. They

proposed a ‘bifurcation enhancement factor’ to indicate the enhanced deposition of particles on the carinal ridges. Comer et al., (2001) simulated the flow and particle deposition in a double bifurcation airway model and calculated the enhanced deposition in the vicinity of the bifurcation. Zhang and Kleinstreuer, (2002) simulated the micron size aerosol inhalation and deposition in a triple bifurcation lung airway unit model. Matida and Finlay (2004) employed a RANS model to examine airflow in an idealized mouth-throat geometry, which they in turn used to study particle deposition pattern. Nowak et al., (2003) modeled the entire tracheobronchial tree using 3.5 generation ‘Triple Bifurcation Units’ (TBU) and calculated the particle deposition patterns in each generations. Zhang & Finlay (2005) proved that trachea with cartilaginous rings would enhance particle deposition in the trachea for all inhalation rates and particle sizes compared with smooth-walled trachea. Asgharian and Price (2006) found that airflow rate entering each major bronchus was similar for uniform and non-uniform lung expansions and concluded that uniform air inlet condition is sufficient for the predictions of regional and total deposition of particles in the lung.

Most of the lung aerosol deposition studies are based on micron sized particles because they tend to deposit in the upper respiratory tract, whereas smaller particles tend to transport to the more distal parts of the lung. So far there are only limited experimental studies of particle deposition in human lungs using nanoparticles because of the high nanomaterial toxicity. Also numerical simulations of nanoparticle deposition in human lungs are relatively less due to the difficulty in modeling nanoparticle dynamics. Transport of nanoparticles in air stream can be modeled as a ‘‘two-phase flow’’ problem. The particle suspension in human airways can be considered to be dilute due to the low particle volume fraction. Both Eulerian and

Lagrangian approaches can be used to model the transport of nanoparticles in airways. As for the Eulerian approach, the particle transport is modeled using a separate convection–diffusion mass transfer equation. Examples include simulations by Yu et al., (1996, 1998), Kimbell et al., (1993), and Kepler et al., (1998). Zhang et al., (2004) used Eulerian approach to model nanoparticle trajectories in the first three generations of the human tracheobronchial tree including the oral airway. Shi et al., (2008) used the one-way coupled Eulerian approach to model the nanoparticle transport and deposition in a subject specific nasal airway model. In the Euler–Lagrange approach, the particle transport is simulated using trajectory equations including random displacement of particles due to Brownian motion. Moskal and Gradon (2002) used the Euler-Lagrange approach to model particle transport through the upper airways of the human bronchial tree. Kleinstreuer and Zhang et al., (2009) compared the particle deposition in lung airways up to generation 15, for both micron and nanoparticles using CFPD simulations with analytical deposition models. The micron particles were modeled using Euler-Lagrange approach and the nanoparticles were modeled using one-way coupled Eulerian approach.

Martonen et al., (1993) showed that the flow disturbances from the laryngeal jet could propagate into trachea and bronchus. Many other numerical simulation studies have pointed out the importance of turbulent dispersion in particle transport and deposition in human lung airways especially in the first six generations (Mazaheri and Ahmadi, 2002 and 2004, Ma and Lutchen (2009). Due to the recent advancement in computational abilities, complex simulations with either Euler-Euler or two-way coupled Lagrangian particle transport models in realistic lung geometries are possible. Ma and Lutchen (2009) performed a CFD study on

an airway model derived from a CT based one-dimensional centerline airway tree using the *k*-ε turbulence model. Jayaraju et al., (2008) compared the RANS *k*-ω, detached eddy simulation, and large-eddy simulation in an idealized mouth-throat model. They found that the flow fields computed by the latter two models agreed well with the measurements of particle image velocimetry, and improved prediction of particle deposition considerably, in particular for particles of size below 5 μm. Longest and Vinchurkar (2007) studied respiratory aerosol deposition in a symmetric Weibel A (1963) model for the third through fifth generations (G3-G5) using laminar, standard Reynolds-Averaged Navier-Stokes (RANS) *k*-ω and low Reynolds number (LRN) *k*-ω models for steady inspiratory flow. They found that an accurate representation of transitional turbulent flows has a significant effect on particle deposition patterns. Zhang and Kleinstreuer (2003) analyzed the flow transition from laminar to turbulence in a straight tube with 75% constriction and an oral airway with partial occlusions using four widely used RANS turbulence models, namely LRN k$-\varepsilon$ model, renormalization group (RNG) k$-\varepsilon$ model, LRN k$-\omega$ model and Menter k$-\omega$ model. They found that LRN k$-\omega$ model with appropriate damping functions and turbulence constants can produce accurate transitional turbulence. Varghese and Frankel (2003) compared the *k*-ε model with the *k*-ω model by simulating the flow through a stenotic vessel. They concluded that the velocity profiles are best predicted by the latter one. It is noticed that the *k*-ε model has shortcomings, which indicates the need for an experimentally validated low Reynolds number (LRN) turbulence model that can represent laminar, transitional and turbulent flows in an upper airway model. Menter (1994) developed a more accurate Reynolds-Averaged Navier-Stokes (RANS) model, called the Shear Stress Transport (SST) model, by combining

the standard k-ω model in the near-wall region and the standard k−ε model in the far field region. Shear Stress Transport (SST) model is more accurate and reliable compared to the standard *k-ω* model. The advantage of an SST *k-ω* model is that it can obtain an accurate laminar solution when the turbulent viscosity approaches zero. This is a necessity when dealing with flows in transitional regions. Modeling technique using Large Eddy Simulation (LES) and Direct Numerical Simulation (DNS) can also be used, for they are supposed to be more accurate, but also more time and cost consuming. LES is a technique where the large energy carrying eddies are simulated, while the smaller eddies are filtered and modeled using a sub-grid scale model. Zhang and Kleinstreuer (2011) confirmed that LES and SST *k-ω* model do not have measurable differences in predicting laminar, transitional and fully turbulent flows.

2.2 Air flow and particle deposition in the alveolar region of the lung

The gas exchange region of the lung also known as the alveolar region is the most vital part of lung. The alveolar region encompasses millions of alveoli specifically designed to allow gas diffusion during the normal breathing process. Flow behavior and particle deposition in the alveolar region are not yet fully understood because of the complex geometrical structure of alveoli. Understanding the flow and particle behavior in the alveolar region carries utmost importance because inhaled aerosols depositing in the alveoli can lead to potential lung diseases. Also understanding gas flow in alveolar region is vital in the treatment of pulmonary diseases including asthma, chronic obstructive diseases, cystic fibrosis, etc. using therapeutic drug targeting.

Alveoli are arranged around the alveolar ducts of each generation in the form of spherical shaped cups with only one opening to the ducts. These cup shaped alveoli are tightly packed in order to optimize the alveolar surface area. Adjacent alveoli are separated by septa which contain multiple interconnected capillary vessels transferring blood. The structure of alveoli together with the septa can be compared with honey comb or soap bubbles pattern. The alveolar region as a whole can be viewed as a bunch of grapes hanging at the end of a branch. Traditionally it has been thought that the low Reynolds number flow in the alveolar region is completely reversible. Heyder et al., (1988) showed that the alveolar flow mixes irreversibly leading deposition of inhaled particles deep inside the lung. Later Tsuda et al., (1995) conducted numerical analysis of alveolar flow and reported chaotic mixing of flow in the alveolar region. Most of the initial numerical analysis was based on simplified 2-D alveolar structures. The model developed by Tsuda et al., (1995) consists of an axisymmetric 2D straight tube with a torus attached on the outer surface representing an alveolus. The model wall was moved using rhythmic expansion and contraction to represent alveolar wall movement. Tsuda et al., (2002) used flow visualization technique to demonstrate alveolar flow recirculation in a rhythmically ventilated rat lung. They verified their previous numerical results demonstrating chaotic irreversible alveolar flow characterized by stagnation saddle points associated with alveolar vortices. Haber and Tsuda (1998) numerically analyzed the particle deposition pattern in a rhythmically expanding alveolus. The alveolus and alveolar duct were modeled as a spherical cap attached at its rim to a circular opening in an expanding plane. The results showed that the particle deposition pattern considerably varies with the alveolar wall motion. Later Haber et al., (2003) analyzed

the effects of gravity and alveolar wall movement on deposition of particles with size ranging from 0.5 μm to 2.5 μm. They found that the submicron particles are significantly influenced by the alveolar flow patterns compared to the micron sized particles. Henry et al., (2002) obtained similar results using numerical analysis alveolar flow pattern and particle deposition in a 9-cell alveolated duct model.

Darquenne and Paiva (1996) used a simplified model of the alveolated duct using sections of an annular ring around a central channel. They showed that the radial alveolar walls are important sites of particle deposition. Harrington et al., (2006) used a similar geometrical representation to generate three-dimensional multi-bifurcation model of acinar tree. Darquenne (2001) and (2002) used symmetric two-dimensional six-generation structure of the human acinus to study the particle deposition characteristics during normal breathing. Snitzman et al., (2007) analyzed alveolar flow pattern using a three-dimensional expanding alveolus attached to a straight tube. The dimensions of the alveolar duct and alveolus were changed according to the lung dimensions reported by Weibel (2005). They noticed recirculation in proximal acinar generations, but no recirculation was noticed in the final generations. In the deeper acinar generations, flows become largely radial due to rhythmic wall motion and increasing alveolar dimensions. Oakes et al., (2010) conducted experimental study on the terminal alveolar sac made of hyper elastic material under normal breathing conditions. The experimental results showed no recirculation zones for both healthy idealized terminal alveolar sac and emphysemic terminal alveolar sac models. Harding and Robinson (2010) used a terminal alveolar sac model with 13 alveoli with expanding alveolar walls. The numerical analysis, using rhythmic inlet breathing profile, showed significant convective

motion due to expanding alveolar wall. But no recirculation was noticed in any of the alveoli. Berg et al., (2010) observed flow in a hollow compliant model of a terminal air sac, with geometry from an actual human lung cast, under conditions of normal breathing using particle image velocimetry (PIV). This study demonstrated that the two generations immediately proximal to the terminal alveolar sacs do not have recirculating eddies which supports the findings of Harding and Robinson (2010) and Oakes et al., (2010). Recently three-dimensional space filling alveolar models have been used to improve the geometric accuracy and produce realistic lung simulations. Sznitman et al., (2007b) used 14-hedron–shaped alveoli, whereas Kumar et al., (2009) used truncated octahedron-shaped alveoli. In both cases, radial flow was reported for normal breathing conditions, assuming a sinusoidal breathing profile. Ma and Darquenne (2011) used multigenerational three-dimensional models of alveolated airways with arbitrary bifurcation angles and spherical alveolar shape to predict the deposition of 1μm and 3μm aerosol particles in models of human alveolar sac and terminal acinar bifurcation under rhythmic wall motion. Flow recirculation was noticed only during transition between inspiration and expiration and accounted for no more than 1% of the whole cycle.

Zhang and Kleinstreuer (2011) simulated the airflow and nanoparticle deposition in a combined nasal-oral-tracheobronchial airway model. They have validated the model by comparing the computational fluid dynamics velocity profiles with experimental results. Shi et al., (2008) calculated the nanoparticle deposition in a subject specific nasal airway geometry using CFPD simulations. Their results suggest that the particle deposition is high for nanoparticles with diameter less than 5 nm. Also they verified that the influence of mucus

layer in the nasal airway passage is negligible and hence a perfectly absorbing nasal airway wall boundary condition is sufficient to model the nanoparticle transport and deposition. Zhang and Kleinstreuer (2008) calculated the deposition fraction in each bifurcation of the human tracheobronchial tree up to 15^{th} generation using an adjustable Triple Bifurcation Unit (TBU). Similar approach was used in this study to calculate the deposition fractions in each compartment of the lung. For this work, the Shear Stress Transport (SST) k-ω model was chosen to predict the laminar-turbulence transition in upper airways as reported in literatures. Some of the geometries and corresponding grids used for this study were taken from Zhang and Kleinstreuer (2011) and Zhang and Kleinstreuer (2008).

2.3 Geometry

The combined nasal-oral upper airway geometry is shown in Fig. 2.1 and a representative triple bifurcation unit is shown in Fig. 2.2. The nasal airway geometry was developed from a magnetic resonance imaging (MRI) scan of a healthy male. The combined upper airway model consists of three parts: the oral airways (including oral cavity, oropharynx, larynx and trachea), nasal airways (nasal cavity and pharynx), as well as an asymmetric triple bifurcation model representing generations G0 (trachea) to G3 (see Li et al., 2007, Zhang and Kleinstreuer, 2011). The TBU dimensions are similar to the Weibel Type A (1963) geometries, assuming a lung volume of 3.5 L.

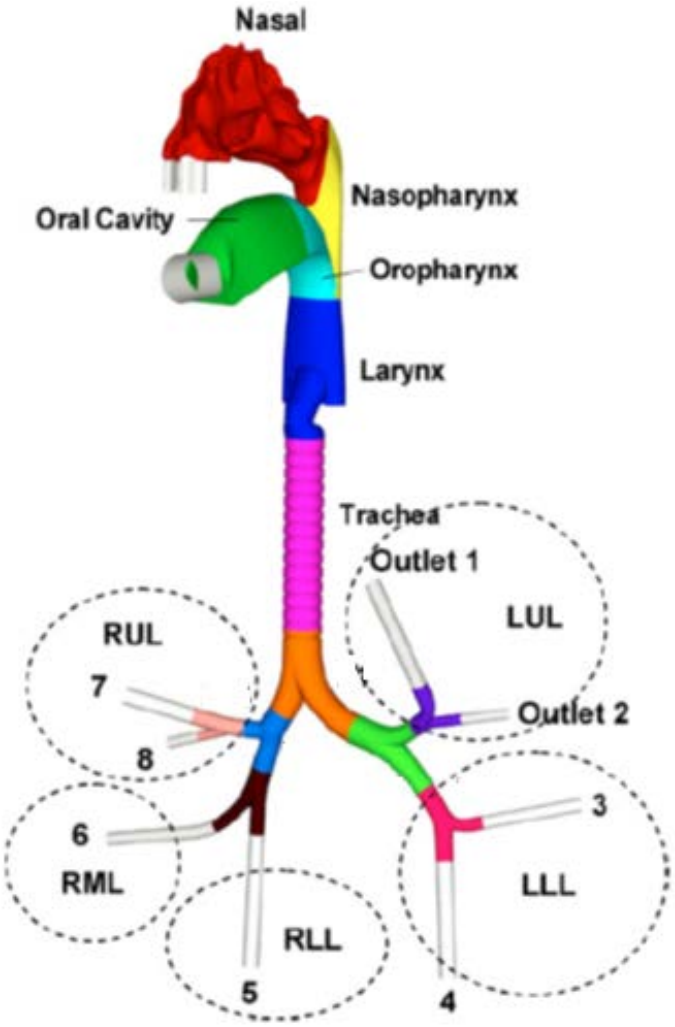

Fig. 2.1. Configuration of representative human nasal-oral upper airway model, with LUL-left upper lobe, LLL-left lower lobe, RUL-right upper lobe, RML-right middle lobe, and RLL-right lower lobe (from Zhang and Kleinstreuer (2011))

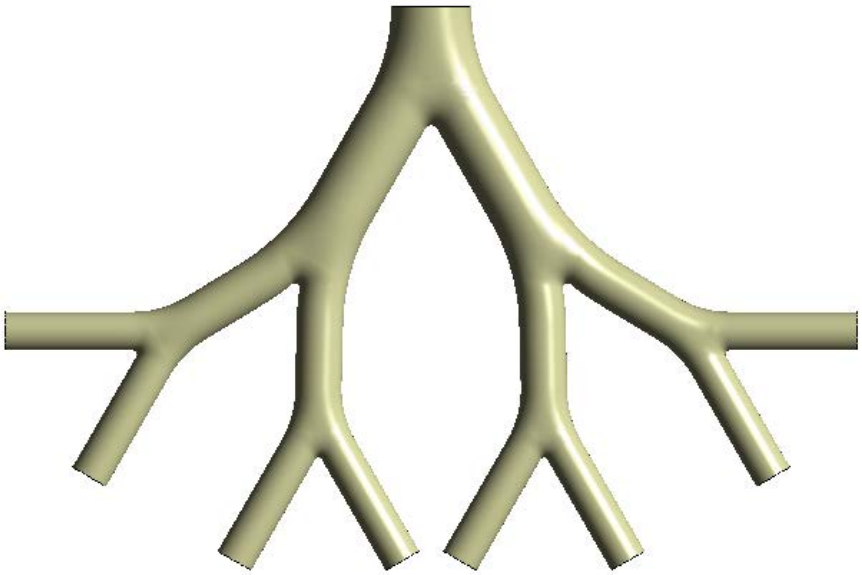

Fig. 2.2. A representative Triple Bifurcation Unit (TBU) model for the upper airways.

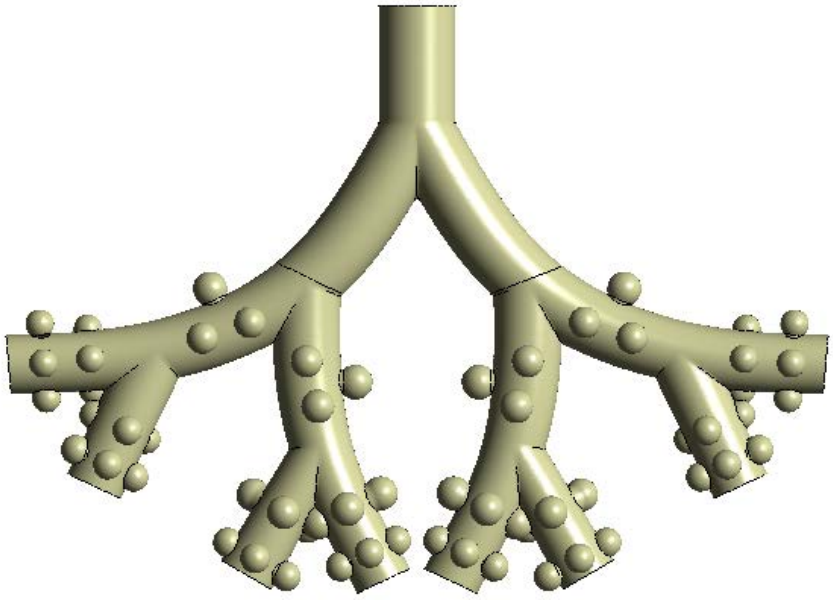

Fig. 2.3. A representative TBU model with alveoli for generation 16-18.

Table 2.1. Comparison of alveolar TBU model dimensions for generation 16-18 with morphometric measurements reported in literature

	Model			**Scaled Weibel (1963)**		
generation	**16**	**17**	**18**	**16**	**17**	**18**
Number of alveoli	0	5	8	0	5	8
Duct diameter (cm)	0.051	0.046	0.043	0.051	0.046	0.043
Segment length (cm)	0.141	0.121	0.108	0.141	0.121	0.1
Alveolus diameter (cm)		0.021-0.022	0.021-0.022		0.0236	0.0236
Alveolus depth(cm)		0.02-0.021	0.02-0.021		0.0235	0.0235
Depth to mouth diameter		1.44	1.44			

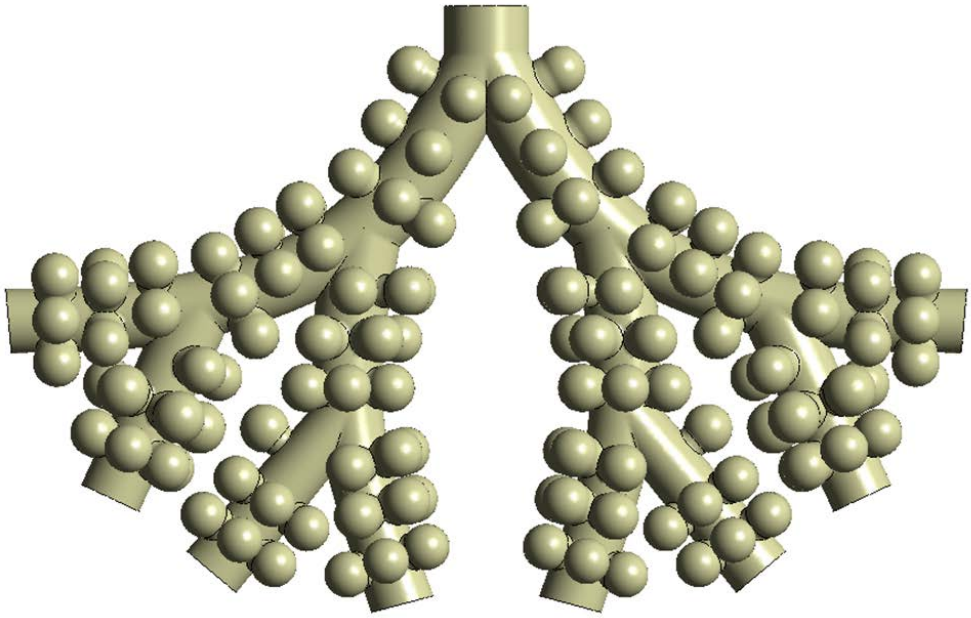

Fig. 2.4. A representative TBU model with alveoli for generation 19-21

Table 2.2. Comparison of alveolar TBU model dimensions for generation 19-21 with morphometric measurements reported in literature

	Model			**Scaled Weibel (1963)**		
generation	**19**	**20**	**21**	**19**	**20**	**21**
Number of alveoli	14	14	14	12	20	20
Duct diameter (cm)	0.04	0.037	0.033	0.04	0.038	0.037
Segment length (cm)	0.098	0.084	0.07	0.085	0.071	0.06
Alveolus diameter (cm)	0.021-0.022	0.021-0.022	0.021-0.022	0.0236	0.0236	0.0236
Alveolus depth(cm)	0.02-0.021	0.02-0.021	0.02-0.021	0.0235	0.0235	0.0235
Depth to mouth diameter	1.44	1.44	1.44			

The alveolar region of the lung was modeled by attaching spherical alveoli to the TBU units. The alveoli attached TBU units were developed using computer aided design software Solid Works. The spherical shape of alveoli was selected based on observations of Hansen et al., (1975). A cylindrical projection from the lumen was used to anchor the spherical alveolus to the duct. The final alveolus has a ¾ spheroid shape. The dimensions of the TBU units and the alveolar cavities were based on the morphometric measurements of Weibel (1963). Table 2.1 shows the dimensions of an average TBU unit of generation 16-18 (Fig. 2.3). Weibel (1963) reported that the alveolar region starts from the 17^{th} generation with 5 alveoli and the 18^{th}

generation has 8 alveoli. The duct diameters were based on Weibel Type A geometries (1963), assuming a lung volume of 3 L. The diameter and depth of the alveoli in the 17^{th} and the 18^{th} generations were 0.021 cm and 0.02 cm respectively. Table 2 shows the dimensions of an average TBU unit of generation 19-21. Weibel (1963) reported that the 19^{th} generation has 12 alveoli, 20^{th} generation has 20 alveoli and 21^{st} generation has 20 alveoli. But due to space constriction, the developed model has 14 alveoli in 19^{th}, 20^{th} and 21^{st} generations (Fig. 2.4). Table 2.2 shows the dimensions of an average TBU unit of generation 19-21. Weibel (1963) reported an average outlet diameter and depth of 0.018 cm and 0.0196 cm for an average total lung volume of 2.63L. It should be noticed that these dimensions were used to get a reference geometry. Each TBU units were again scaled to match the outlet diameters of the previous generations.

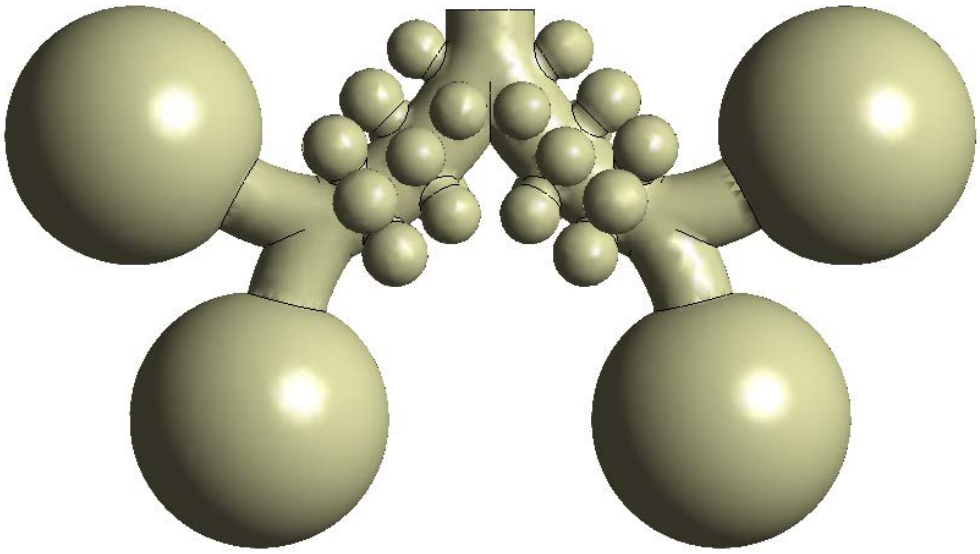

Fig. 2.5. A representative Double Bifurcation Unit (DBU) model with alveoli for generation 22-23

Fig. 2.5 represents the TBU model of generation 22-23. As reported in literature, the final generation was modeled as a closed sac. The generation 22 has 14 alveoli attached to it duct. Instead of using separate alveoli, single spherical alveolus was used in generation 23. The total surface area of 23rd generation was conserved in the model by creating the ¾ spheroid with the same total surface area as generation 23. The total surface area of generation 23 was calculated based on the reported number of alveoli, 17 in generation 23, and the duct diameter

A mesh convergence study was performed for the TBU units in the alveolar region in order to increase the accuracy of the results and optimize the computational cost and time. The particle mass flux on the wall elements was used as the criterion to determine grid independency. It was found that for the TBU model representing generations 16-18, when the number of mesh elements (tetrahedral elements were used) were increased from 756135 to 1455907, the particle mass flux on the wall elements changed by 9% which shows that solution depends highly on the mesh quality. Refining the mesh by increasing the number of elements from 1455000 to 1800000 resulted in only less than 1% change in particle mass flux on wall elements. So the mesh with 1801366 elements was chosen for the simulation. Similarly the mesh for the TBU models representing generations 19-21 and 22-23 were also refined to achieve a mesh independent solution. The final mesh for the TBU 19-21 model has 3680000 elements. Since a Fluid Structure Interaction (FSI) modeling was used for the final 22-23 model, separate fluid and solid domain meshes were created. After the mesh independent study, the final grid has 80000 elements in the solid domain and 700000 elements in the fluid domain.

2.4 Model validation

In order to validate the CFPD modeling technique, the nanoparticle deposition in a nasal geometry using CFPD simulations were compared with in vitro experimental results (see Cheng et al., 1995 and Kelly et al., 2004) in various nasal replicas for inhalation flow rates of $Q_{nose,\ in}$ = 4 L/min, 7.5 L/min and 10 L/min. Figure 2.6 shows the comparison of CFPD nanoparticle deposition results with the experimental results. Reasonable agreement was obtained between the CFPD deposition results and experimental results, even though the in vitro experimental results are highly scattered. In Fig. 2.6, SLA and Viper refer to nasal replicas manufactured with different rapid prototype machines; ANOT refers to adult-nasal-oral-trachea. CFPD deposition results match well the experimental results for particle diameters greater than 10 nm. But as the particle size decreases below 10 nm, the CFPD simulation results appear to under predict the deposition by 5-10%. This variability in results may be due to the effects of minor geometry differences like wall roughness, physico-chemical properties of nanoparticles like electrostatic forces, and differences in experimental preparation methods. The CF-PD results compare also favorably with the numerical data sets of Xi and Longest (2008).

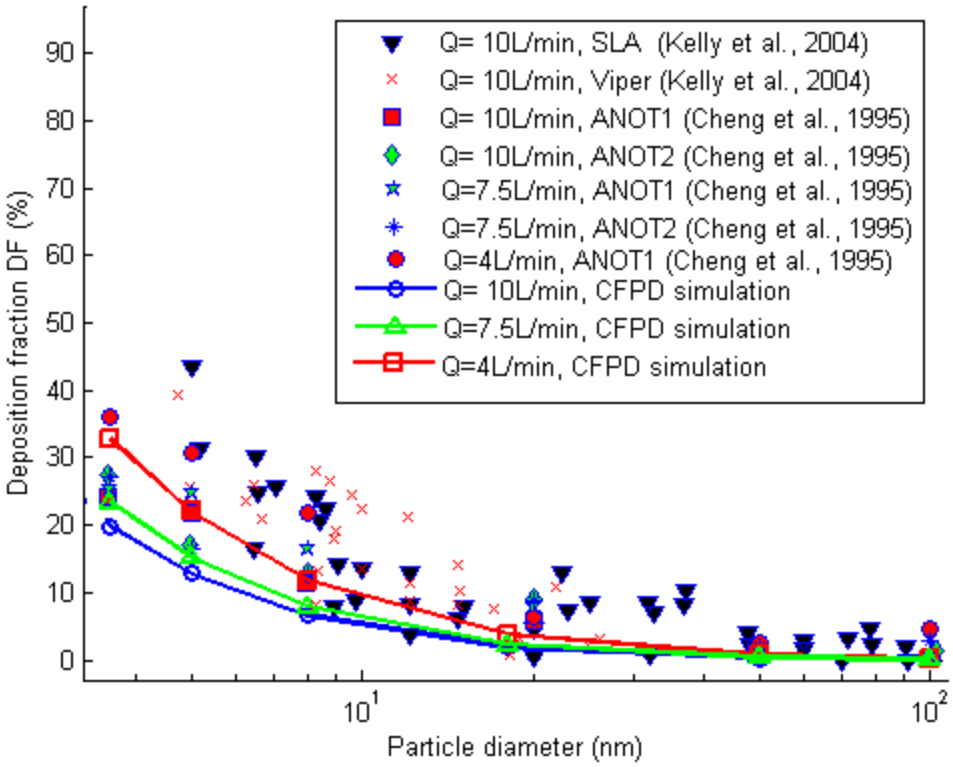

Fig. 2.6 Comparison of CFPD nanoparticle deposition results in human nasal cavities for an inhalation flow rate of with the experimental results.

CHAPTER 3

LUNG NANOPARTICLE DYNAMICS AND CALCULATION OF SEGMENTAL DEPOSITION FRACTION

3.1 Theory

The tracheobronchial tree was constructed using symmetric TBU units connected in series and in parallel as shown in Fig. 3.1. The upper airway geometry starting from the nasal airway to generation 3 were constructed based on average dimensions, so that the asymmetric nature of the tracheobronchial tree was accounted while calculating the particle transfer and deposition. The TBU units fitted to the outlets of the upper airway units were symmetric models based on Weibel Type A (1963) geometries, assuming a lung volume of 3.5 L. The outlet tubes of both upper airway and TBU units were extended to reduce the outlet and downstream effects. In order to capture the influence of the asymmetric property of the tracheobronchial tree, TBU units were fitted to four different outlets of generation 3 of the left lung. Each TBU units were scaled so that the inlet diameter matched the outlet diameter of the previous generation. Since the upstream flow profiles and particle distribution has a significant influence on the particle deposition in subsequent generations, the outlet measurements (velocity profiles and particle distributions) from the combined upper airway geometry were adjusted to become the inlet conditions for the next generation TBUs and the process was continued for all TBUs attached later on. Zhang and Kleinstreuer (2008) found that the geometric effects are negligible for nanoparticle deposition especially for relatively large nanoparticles ($d_p \geq 10$ nm). Hence the non-planar geometric effects are neglected and only coplanar TBU units were used. Also it has been noticed that the gravity has negligible

influence on nanoparticle transport and deposition. So the force due to gravity was neglected in all models.

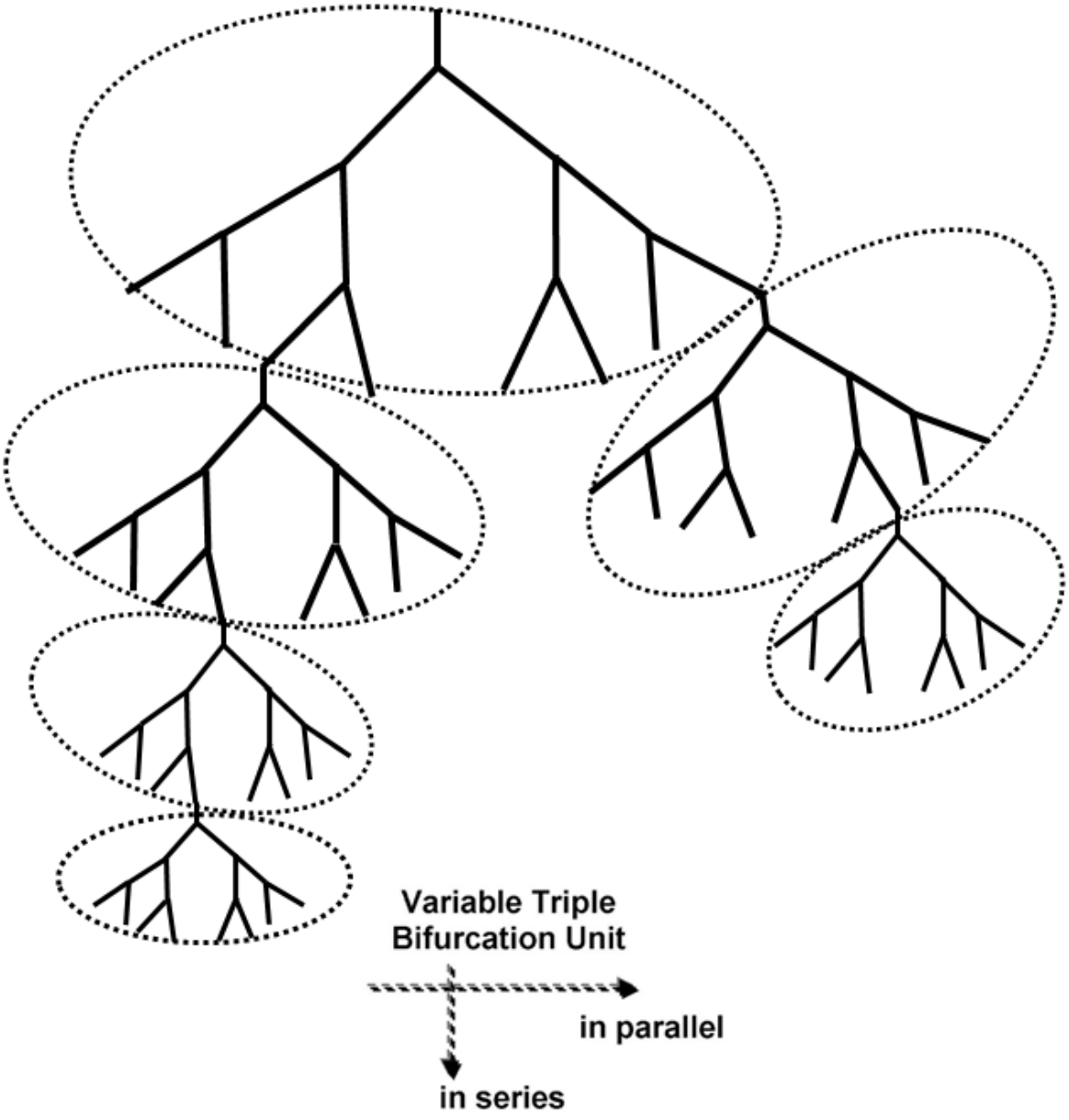

Fig. 3.1. Schematic representation of scaled Triple Bifurcation Unit (TBU) models connected in series and parallel

3.2 Governing equations

3.2.1 Turbulence Model

The Shear Stress Transport (SST) k-ω turbulence model was employed to simulate the laminar, transitional and fully turbulent flow regimes. The SST k-ω turbulence model is a conglomeration of the standard k-ω model in the near-wall region and the standard k−ε model in the far field region. The SST k-ω turbulence model has been found to accurately predict the transitional turbulence flows and particle transport in nasal and oral airway models and tracheobronchial airway bifurcations.

Equations which are commonly used to describe the mass conservation and the momentum for a laminar-turbulent transitional flow, implied by Reynolds averaged Navier-Stokes equations (RANS) and the continuity equation, which govern steady - state two dimensional flow of an incompressible, viscous, Newtonian fluid with no body forces acting are, respectively

$$\frac{\partial \bar{u}_i}{\partial x_i} = 0 \tag{3.1}$$

$$\frac{\partial \bar{u}_i}{\partial t} + \bar{u}_j \frac{\partial \bar{u}_i}{\partial x_j} = -\frac{1}{\rho}\frac{\partial \hat{p}}{\partial x_i} + \frac{\partial}{\partial x_j}[(\nu + \nu_t)(\frac{\partial \bar{u}_i}{\partial x_j} + \frac{\partial \bar{u}_j}{\partial x_i})] \tag{3.2}$$

Where $\bar{u}_i$ is the time-averaged velocity in three coordinate directions, i.e., i=1, 2, and 3, $\hat{p}$ is the modified time-averaged pressure term, ρ is the fluid density, and ν is the kinematic viscosity and ν_t is the turbulent viscosity.

The transport equations governing the turbulent kinetic energy (k) and the specific dissipation rate (ω) are given by

$$\rho\left[\frac{\partial(k)}{\partial t}+\overline{u_j}\frac{\partial(k)}{\partial x_j}\right] = P-\beta^*\rho\omega k+\frac{\partial}{\partial x_j}\left[(\mu+\sigma_k\mu_t)\frac{\partial k}{\partial x_j}\right] \tag{3.3}$$

$$\rho\left[\frac{\partial(\omega)}{\partial t}+\overline{u_j}\frac{\partial(\omega)}{\partial x_j}\right] = \frac{\gamma}{\nu_t}P-\beta\rho\omega^2+\frac{\partial}{\partial x_j}\left[(\mu+\sigma_\omega\mu_t)\frac{\partial\omega}{\partial x_j}\right]+ 2(1-F_1)\frac{\rho\sigma_{\omega 2}}{\omega}\frac{\partial k}{\partial x_j}\frac{\partial\omega}{\partial x_j} \tag{3.4}$$

where

$$P=\tau_{ij}\frac{\partial\bar{u}_i}{\partial x_j} \tag{3.5}$$

$$\tau_{ij}=\mu_t\left(2S_{ij}-\frac{2}{3}\frac{\partial u_k}{\partial x_k}\delta_{ij}\right)-\frac{2}{3}\rho k\delta_{ij} \tag{3.6}$$

$$S_{ij}=\frac{1}{2}\left(\frac{\partial\bar{u}_i}{\partial x_j}+\frac{\partial\bar{u}_j}{\partial x_i}\right) \tag{3.7}$$

and the turbulent eddy viscosity is defined using limiter and blending functions as shown below

$$\mu_t=\frac{\rho a_1 k}{max(a_1\omega, SF_2)} \tag{3.8}$$

Additional functions are given by:

$$F_1=tanh\left(arg_1^4\right) \tag{3.9}$$

$$arg_1 = min\left[max\left(\frac{\sqrt{k}}{\beta^* \omega d}, \frac{500\nu}{d^2\omega}\right), \frac{4\rho\sigma_{\omega 2}k}{CD_{k\omega}d^2}\right] \tag{3.10}$$

$$CD_{k\omega} = max\left(2\rho\sigma_{\omega 2}\frac{1}{\omega}\frac{\partial k}{\partial x_j}\frac{\partial \omega}{\partial x_j}, 10^{-20}\right) \tag{3.11}$$

$$F_2 = tanh\left(arg_2^2\right) \tag{3.12}$$

$$arg_2 = max\left(2\frac{\sqrt{k}}{\beta^* \omega d}, \frac{500\nu}{d^2\omega}\right) \tag{3.13}$$

Where ρ is the density, $\nu_t = \mu_t/\rho$ is the turbulent kinematic viscosity, μ is the molecular dynamic viscosity, *d* is the distance from the field point to the nearest wall, and Ω is the vorticity magnitude.

Note that it is generally recommended to use a production limiter to avoid the excessive build up turbulent kinetic energy in the stagnation regions (see Menter, 1993). In this the term *P* in the *k*-equation is replaced by:

P= min (P, $C_{lim}\ \rho\varepsilon$) where C_{lim} is called clip factor and has a value of 10.

The model constants are:

$$\beta^* = 0.09 \quad , a_1 = 0.31 \, , \kappa = 0.41 \tag{3.14}$$

Inner model coefficients are

$$\sigma_{k1} = 0.85 \ , \ \sigma_{\omega 1} = 0.5 \ , \ \beta_1 = 0.075 \ , \ \gamma_1 = \frac{\beta_1}{\beta^*} - \frac{\sigma_{\omega 1}\kappa^2}{\sqrt{\beta^*}} \tag{3.15}$$

Outer model coefficients are

$$\sigma_{k2} = 1 \ , \ \sigma_{\omega 2} = 0.856 \ , \ \beta_2 = 0.0828 \ , \ \gamma_2 = \frac{\beta_2}{\beta^*} - \frac{\sigma_{\omega 2}\kappa^2}{\sqrt{\beta^*}} \tag{3.16}$$

The model coefficients (denoted with the symbol Φ) are defined by blending the coefficients of the original *k*-ω model, denoted as Φ_1, with those of the transformed k-ε model, denoted as Φ_2:

$$\phi = F_1\phi_1 + (1 - F_1)\phi_2 \text{, where } \quad \phi = \{\sigma k, \sigma_\omega, \beta, \gamma\} \tag{3.17a,b}$$

3.2.2 Nanoparticle transport and deposition equations

The Euler-Euler particle tracking approach is found to be more suitable in tracking quasi-spherical nanoparticles, when d_p < 100 nm, than the Euler-Lagrangian approach. This approach treats the particle as a continuum field, and neglects the particle inertia and the effects of the particle phase on the flow field. In this model the particle concentration is calculated from a convective-diffusive equation using terminal particle velocity. Ignoring coagulation, surface growth, nucleation, and other internal/external forces, the convection-diffusion mass transfer equation of nanoparticles can be written as

$$\frac{\partial Y}{\partial t} + \frac{\partial}{\partial x_j}(u_j Y) = \frac{\partial}{\partial x_j}[D_p \frac{\partial Y}{\partial x_j}] \tag{3.18}$$

where x_j is the coordinate variables (j = 1, 2, 3), u_j is the air velocity, Y is the mass fraction, and D_p is the diffusion coefficient. Assuming the diffusion is isotropic and considering the presence of turbulent dispersion, the effective diffusion coefficient (D_p) is given as:

$$D_p = \widetilde{D} + \frac{\nu_T}{\sigma_Y} \tag{3.19}$$

where ν_T is the eddy viscosity, σ_Y is the turbulent Schmidt number taken to be 0.9, and $\widetilde{D}$ is the thermodynamic aerosol diffusion coefficient. For spherical nanoparticles, $\widetilde{D}$ is

calculated based on kinetic theory as follows (Stokes-Einstein equation, assuming dilute concentration of spherical particles)

$$\widetilde{D} = \frac{k_B T C_{slip}}{3\pi\mu d_p} \tag{3.20}$$

where k_B is the Boltzmann constant (1.38 9 10^{-23} J K-1), T is the temperature, d_p is the particle diameter, μ is the fluid viscosity, and C_{slip} is the Cunningham slip correction factor

$$C_{slip} = 1 + \frac{2\lambda_m}{d_p}\left[1.142 + 0.058\exp\left(-0.999\frac{d_p}{2\lambda_m}\right)\right] \tag{3.21}$$

where λ_m is the mean free path in air

The local wall mass flux of nanoparticles can be determined as

$$\dot{m}_w = \rho A_i j_{wall,i} \tag{3.22}$$

where ρ is the gas mixture density, A_i is the area of local wall cell (i) and $j_{wall,i}$ is the particle flux at the local wall cell given by

$$j_{wall,i} = -D_p \left.\frac{\partial Y}{\partial n}\right|_{wall,i} \tag{3.23}$$

The local Deposition Fraction (DF) and Deposition Efficiency (DE) of nanoparticles, which is defined as the ratio of local wall mass flux to the inlet mass flux, can be expressed as

$$DF_{local} = \frac{(A_i j_{wall,i})}{(Q_{mouthin} Y_{mouthin})} \tag{3.24}$$

$$DE_{local} = \frac{(A_i j_{wall,i})}{(Q_{localin} Y_{localin})} \tag{3.25}$$

and the regional DF and DE can be determined as

$$DF_{region} = \frac{\sum_{i=1}^{n} (A_i j_{wall,i})}{(Q_{mouthin} Y_{mouthin})} \tag{3.26}$$

$$DE_{region} = \frac{\sum_{i=1}^{n} (A_i j_{wall,i})}{(Q_{localin} Y_{localin})} \tag{3.27}$$

where n is the number of wall cells in one specific airway region. The subscript ‘‘mouthin’’ refers to mouth inlet, while ‘‘localin’’ refers to the inlet at the specific airway generation. The local inlet flow rate and particle mass are calculated as the sum of local values of cells at this specific inlet.

The relationship between the DF and DE is given by

$$DF_{TBU\ 1} = DE_{TBU\ 1}\ (1\text{-}DE_{\text{nasal-oral upper airway}}) \tag{3.28}$$

$$DF_{TBU\ i} = DE_{TBU\ i}\ (1\text{-}DE_{\text{upper airway}})\ (1\text{-}\ DE_{TBU\ 1})\ (1\text{-}\ DE_{TBU\ 2})\ldots\ldots..\ (1\text{-}\ DE_{TBU\ i\text{-}1}) \tag{3.29}$$

Assuming that the airway wall is a perfect sink for aerosols upon touch, the boundary condition on the wall for Eulerian transport model is $Y_w = 0$. Even though this boundary condition neglects any particle-wall interaction, the assumption holds true for particles larger than 1nm. In this study nanoparticle of diameter 37 nm and 18 nm were used.

3.2.3 Fluid Structure Interaction Equations

$$\frac{\partial \sigma_{ij}^{s}}{\partial x_j} + \rho_s F_i = \rho_s \frac{\partial^2 d_i^s}{\partial t^2} \tag{3.30}$$

$$\sigma_{ij}^{s} = E_{ijkl}\varepsilon_{kl} \tag{3.31}$$

$$d_i^f = d_i^s \tag{3.32}$$

where σ_{ij}^{s} is the stress tensor, E_{ijkl} is the elasticity tensor, ε_{kl} s the strain matrix, ρ_s is the density of the solid, d_i^f and d_i^s are the fluid and solid nodal displacements. The kinematic condition in Eq. (28) requires equal displacements of the fluid and solid nodes at the fluid-structure interfaces. The value of E was selected such that the total alveolar volume change (here it is assumed that the total alveolar volume change is produced by the expansion of alveoli in 23rd generation since alveolar wall movement was considered in the 23rd generation only) is 25% to 30% (radial dimension change of 7.7% to 9.1%) for a transmural pressure gradient of 200 Pa.

3.3 Numerical method

The governing mass and momentum conservation equations in conjunction with the SST $k-\omega$ turbulence model as well as the Eulerian mass transport equation were solved using a user enhanced commercial finite volume CFD package CFX from ANSYS, Inc. (Canonsburg, PA). The flow regime was assumed steady to capture the particle deposition characteristics independent of periodic conditions. Advection terms in the governing equations were discretized using a second order high resolution scheme. The solutions to the flow field were assumed to be converged when the dimensionless mass and momentum residual ratios were $< 10^{-4}$. Also a converged solution was ensured for the Euler mass transport model by imposing a convergence criterion of 10^{-4} for the residual of nanoparticle mass fraction variable.

3.4 Boundary conditions

In order to observe the particle deposition characteristic during a normal rest/light activity breathing condition, a mass flow rate of 15 L/min was applied at the nasal inlet of the upper airway model. The oral airway opening was considered closed, so that the breathing was assumed to happen through nostrils only. A nanoparticle mass fraction of 1 was assumed at the nasal inlet. Uniform zero pressure gage opening boundary condition was established at all outlets. No slip boundary condition was used on the airway walls. The outlets of all models were extended to reduce outlet and downstream effects, such that the velocity was normal to the outlet planes (negligible radial velocity component). Flow and particle outflow conditions from the 8 outlets of the nasal-oral upper airway model were imported as inlet conditions for

the first level TBU models representing generation 4-6, whose outlet conditions were applied for the next generation TBU models and so on.

3.5 Results

3.5.1 Flow structures and particle distributions in the nasal-oral upper airway model

Flow fields for the combined nasal oral upper airway model for an inhalation flow rate of 15 L/min were simulated assuming steady state flow. Fig. 3.2 shows the flow stream lines as well as the axial velocity contours and secondary velocity vectors at selected cross sections. Flow stream lines (Fig. 3.2a), which provide a quantitative visualization of the flow behavior, were captured by following massless particles released from nasal inlets. Fig. 3.2b shows the velocity contours at various cross sectional slices. Fig 3.3 shows the flow behavior in the nasal cavity. Flow in the nasal cavity is important because of the presence of olfactory sensory receptors. Majority of the flow was found to continue through the lower nasal air passages (middle and inferior meatus), thereby protecting the upper olfactory region. Secondary flow phenomenon such as flow separation and recirculation can be noticed once the flow passes the nasal vestibule due to the apparent 90^0 change in flow direction. The reduction in cross sectional area after the nasal vestibule forces the flow to accelerate and creates secondary velocity components which distribute the air to the middle and inferior meatus. Slice A-A1 in Fig. 3.3b shows the secondary velocity components and flow acceleration. Fig. 3.2c shows the contour of turbulent kinetic energy in the upper airway

model. Turbulence was noticed mainly in the nasal valve region (Fig. 3.3c) and in the high shear area after the glottis due to the laryngeal jet.

In the nasopharynx region, the flow undergoes another 90^0 change in direction, which produced secondary flow structures. Recirculation regions in the nasopharynx can be noticed from the flow stream lines in Fig. 3.2a. Random mixing of flows can be noticed when the nasopharynx meets the oropharynx. Slice A-A1 in Fig. 3.2b shows the secondary flow velocity vectors when nasopharynx meets the oropharynx. Even though the oral inlet was closed, a small percentage of the flow entered the oral airway. Due to the sudden geometric constriction at the glottis, an asymmetric high speed laryngeal jet was developed. The laryngeal jet produced a recirculation zone near the anterior wall of the upper trachea. Also the curved geometry of the epiglottis produced secondary vortical structures which can be easily noticed in slice C-C1 of Fig. 3.2b. Due to the secondary flow structures, the velocity profile in the trachea is skewed towards the anterior part. Once the flow advances in the trachea, the velocity profile is redistributed by the secondary motion, producing a parabolic profile. Flow separation and recirculation was noticed in the bronchial airway bifurcation regions. The flow profile and secondary flow structures in the daughter branches of the bronchial airways were found to vary with the bifurcation angle and daughter tube diameters.

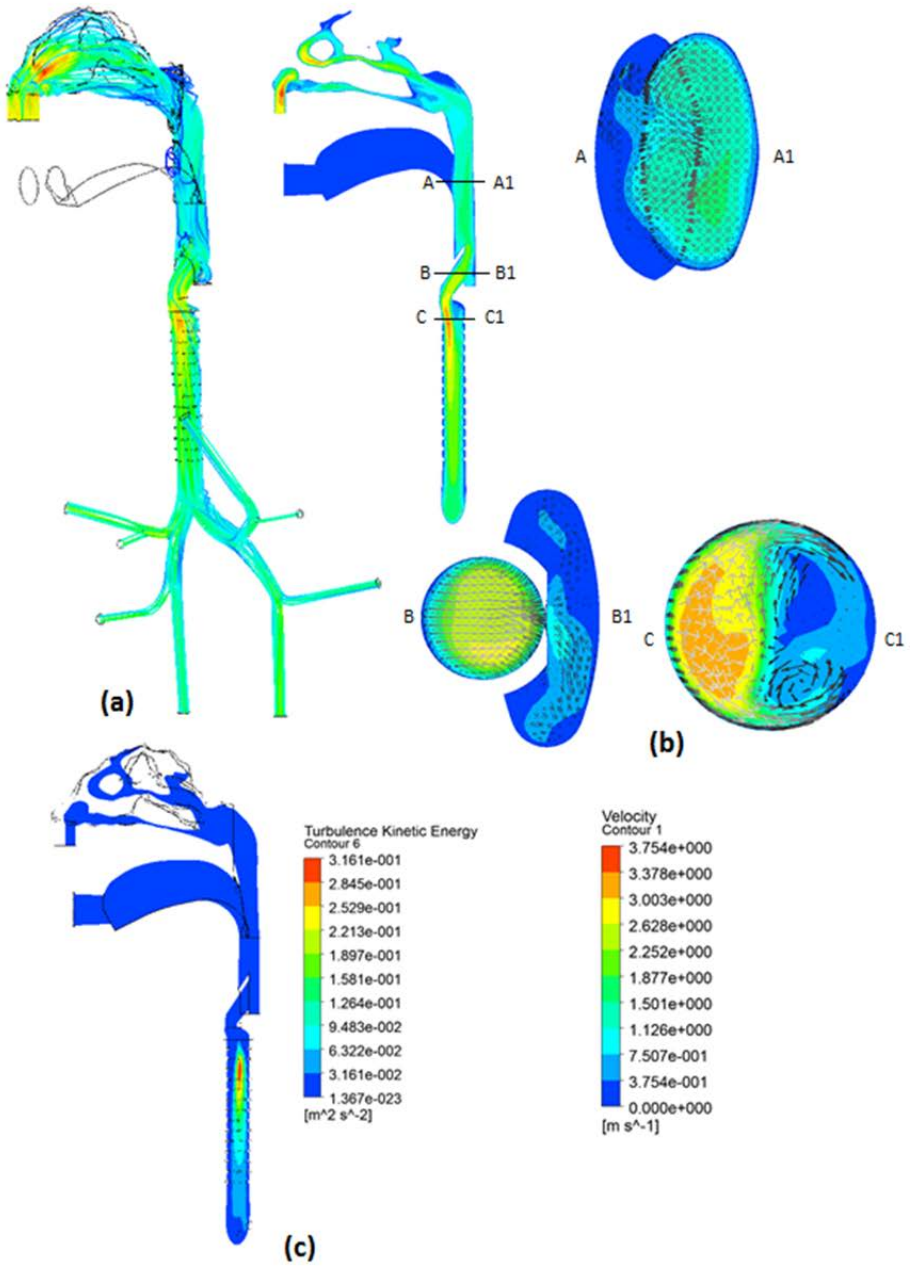

Fig. 3.2 . Flow in the combined nasal-oral upper airway model. (a) Flow stream lines and velocity contours, (b) velocity contours and secondary velocity vectors at selected cross sections and (c) contour of turbulence Kinetic energy at selected cross section

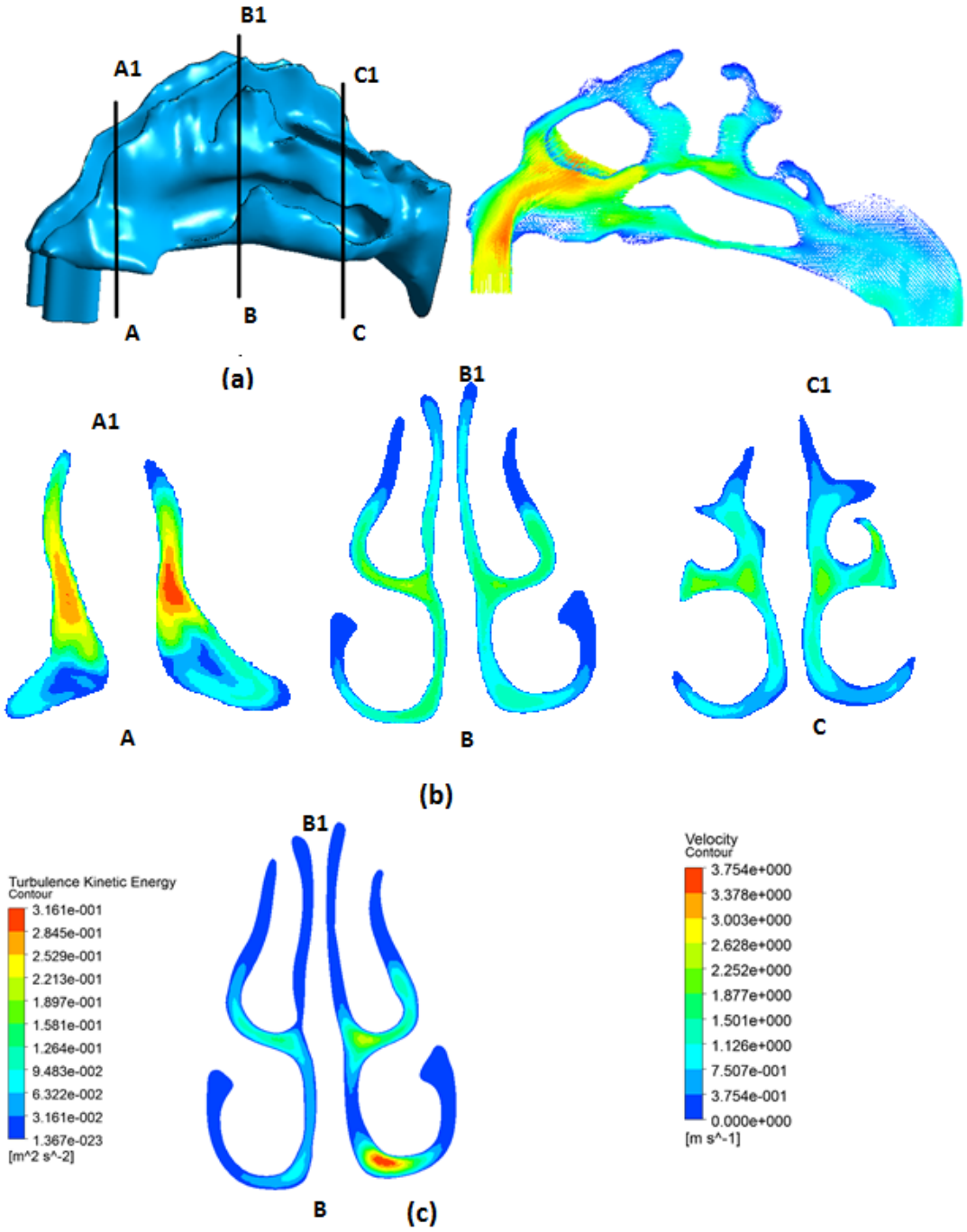

Fig. 3.3. Flow in the nasal airway model. (a) Realistic nasal surface geometry, (b) velocity contours and velocity vectors at selected cross sections and (c) contour of turbulence Kinetic energy at selected cross section

Fig. 3.4a displays the mass fraction contours in a vertical plane and at selected cross sections of the combined nasal-oral airway model. The distribution of nanoparticle is mainly controlled by the convective diffusion, Brownian diffusion and turbulent dispersion. Mass flow rate of the fluid and size of the nanoparticle are the two significant parameters which influence the nanoparticle distribution and deposition. In this study, transport and deposition of 37 nm particles were simulated. It can be noticed that the mass fraction distributions has a high resemblance with the velocity field contours, which indicates that the nanoparticles closely follows the fluid flow. Due to the secondary flow structures, nanoparticles were well distributed. Dense concentration of nanoparticle was observed with areas of high flow velocities because of the higher convection. Similarly low velocity regions like flow separation, recirculation were associated with less particle concentration. Low particle concentrations were noticed near the olfactory region and the tip of middle and inferior meatus. A low concentration of nanoparticles was found to enter the oral airway. After the nasopharynx, a uniform distribution of nanoparticles was noticed, which is due to the secondary flow structures. Fig. 3.4b displays the nanoparticle concentration gradient on the wall, which indicates the mass flux near the wall. The deposition of nanoparticles on the wall can be calculated from the mass flux as described in equation (3.26). Nanoparticle deposition in the nasal passages was found to be less compared to the nasopharynx and oropharynx. In the bronchial airways, the deposition of nanoparticles found to vary with the diameter of the airways. Airways with smaller diameter have higher nanoparticle deposition than larger airways.

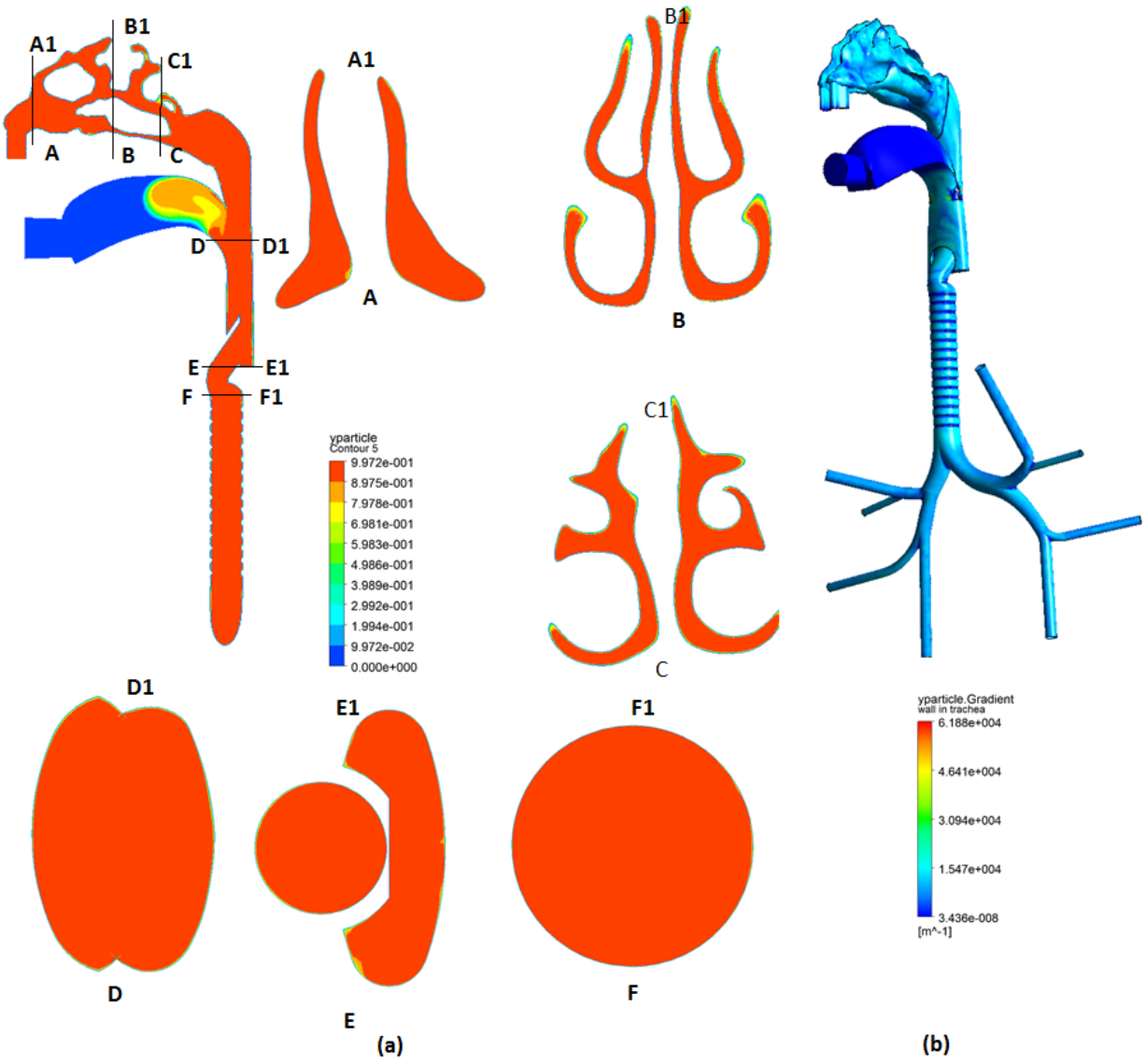

Fig. 3.4. Mass fraction in the combined nasal-oral airway model. (a) Contours in a vertical plane and at selected cross sections and (b) nanoparticle concentration gradient on the wall.

3.5.2 Flow structures and particle distribution in bronchiolar airways

Four outlets of the combined nasal-oral upper airway model (right lung lobes) were selected and the scaled TBU models were connected to these outlets to simulate the nanoparticle distribution in the bronchiolar airways. Fig. 3.5 depicts the flow structures and secondary velocity vectors at selected cross sections in a TBU model representing generation 4-6 started from outlet 4 of the combined nasal-oral upper airway model. The inlet condition for this TBU was obtained from outlet 4 of the combined nasal-oral upper airway model. Since the diameters of the bronchiolar airways of the combined nasal-oral upper airway model were different, the flow rates through each outlet were also different. So the attached TBUs also had different inlet flow rates. This helped in calculating an average deposition data based on different bronchiolar airway diameters.

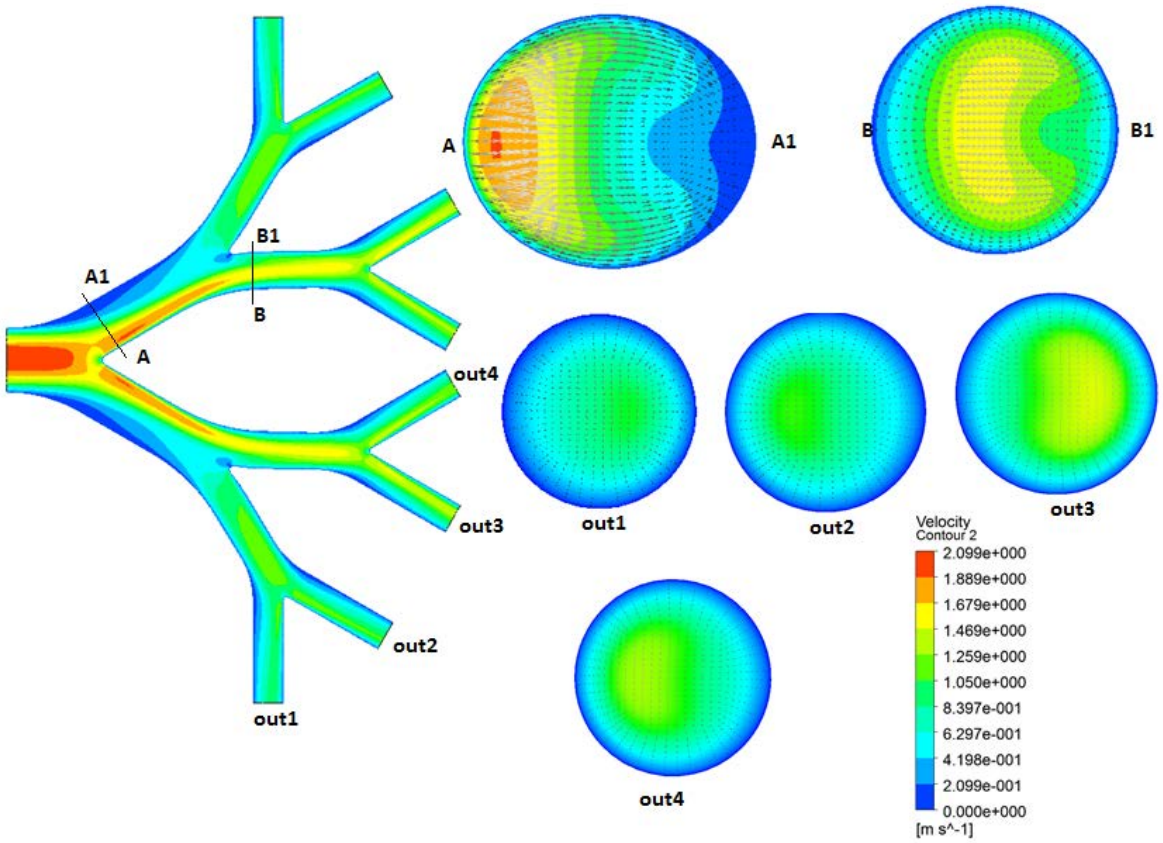

Fig. 3.5. Flow structures and secondary velocity vectors at selected cross sections in a TBU model representing generation 4-6 started from outlet 2 of the combined nasal-oral upper airway model

Secondary flow structures were noticed near the vicinity of bifurcations. Down the bifurcation the velocity profile changed significantly. Change of cross section causing adverse pressure gradient and curved geometry drives the fluid towards the inner wall, producing skewed velocity profile with maximum velocity near the inner wall. It can be noticed that the highest axial velocity is adjacent to the inside wall of the bifurcation (skewed profile). As the flow proceeds from the bifurcation, fluid from the center line where the velocity is high, move towards the inner wall of the bifurcation. This secondary motion can

be attributed to the curvature of the daughter tubes. As the daughter tubes become straight the secondary motion damps out and the velocity profile changes back to parabolic distribution.

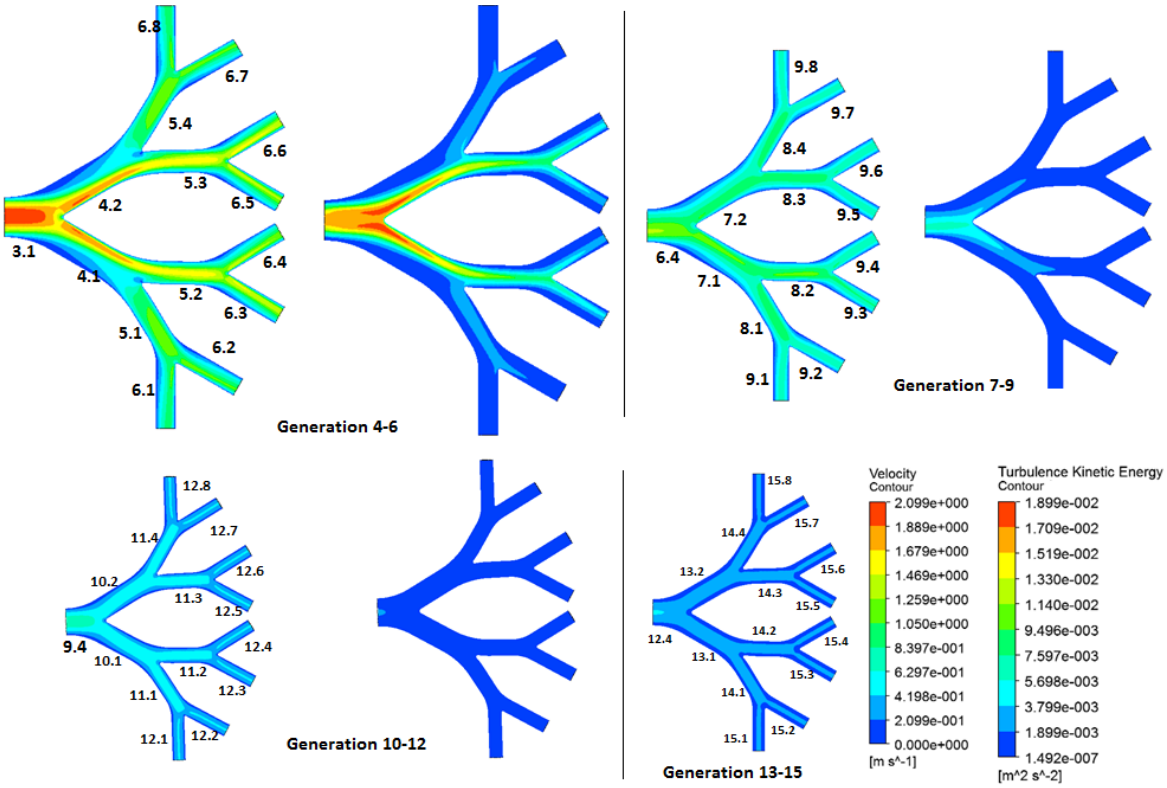

Fig. 3.6. Velocity and Turbulent Kinetic Energy (TKE) contours along a mid-plane plotted for TBUs representing generations 4-6, 7-9, 10-12 and 13-15 respectively. TKE in generation 13-15 has not been plotted since laminar flow model was used. The inlet conditions for generation 3 were taken from outlet 4 of combined nasal-oral airway model.

Fig. 3.6 displays the Velocity and the Turbulent Kinetic Energy (TKE) contours along a mid-plane plotted for TBUs representing generations 4-6, 7-9, 10-12 and 13-15. The inlet conditions for generation 3 were taken from outlet 4 of combined nasal-oral airway model. Skewed velocity profiles can be noticed in most of the upper bronchial airways up to generation 9. It

means that the secondary flow components are significant in the upper lung airways up to generation 9. With the reduced Reynolds number after generation 9, the flow can be assumed fully developed. The Turbulent Kinetic Energy, which shows the amount of turbulence, is significant in the upper lung airways up to generation 9. This implies that laminar flow can be assumed from generation 10 onwards.

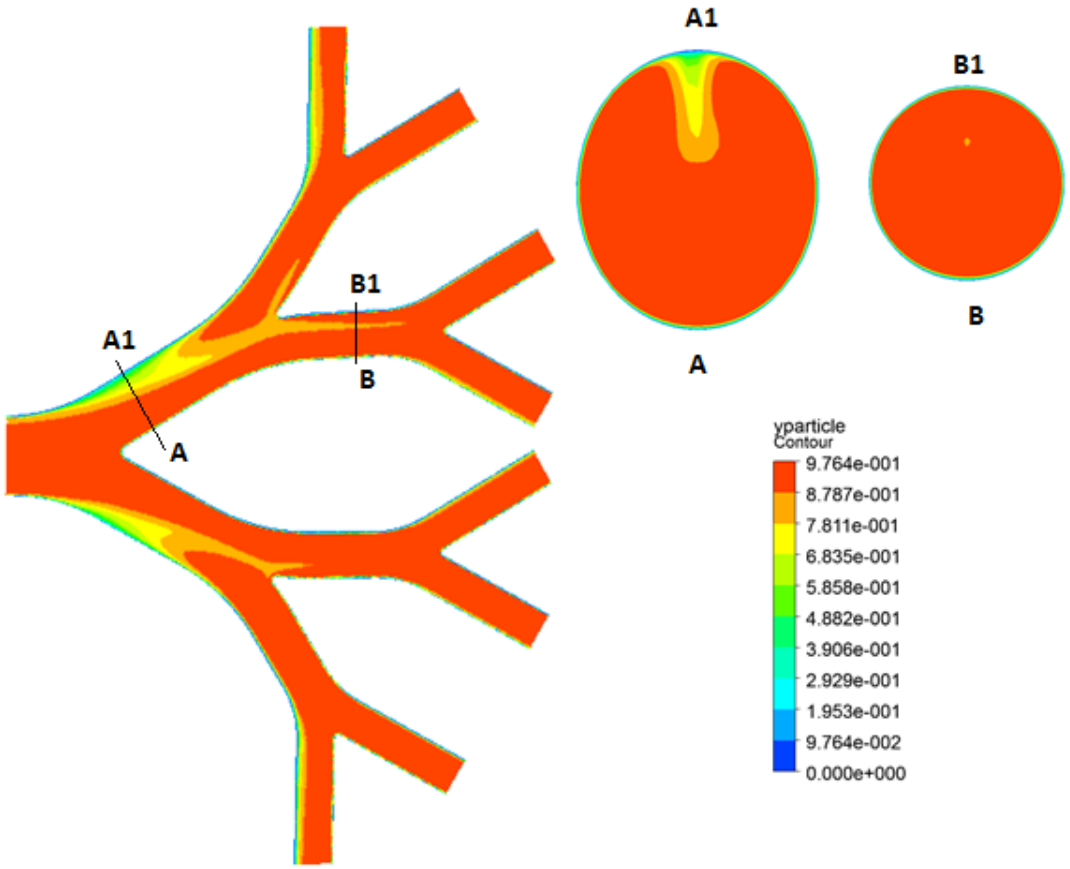

Fig. 3.7 Distribution of nanoparticle in generation 4-6

Fig. 3.7 displays the distribution of nanoparticle in generation 4-6. The mass fraction distributions have a high resemblance with the velocity field contours, which indicates that the nanoparticles closely follow the fluid flow. At the bifurcation, due to the flow separation, a low concentration of nanoparticle was noticed. Dense concentration of nanoparticle was observed with areas of high flow velocities because of the higher convection. Similarly low velocity areas like flow separation, recirculation were associated with less particle concentration. Fig. 3.8 displays the nanoparticle concentration contours along a mid-plane and nanoparticle concentration gradient on wall for TBUs representing generations 4-6, 7-9, 10-12 and 13-15 respectively.

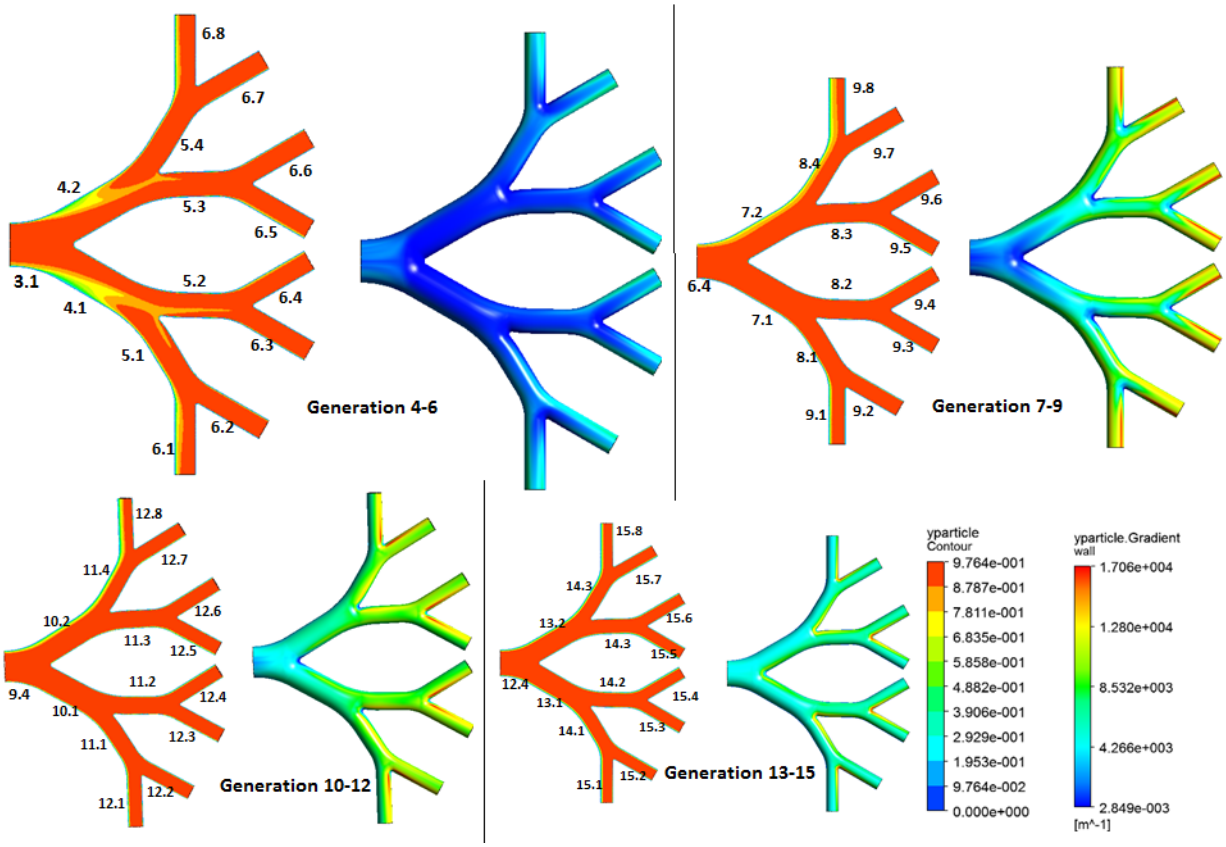

Fig. 3.8. Nanoparticle concentration contours along a mid-plane and nanoparticle concentration gradient on wall for TBUs representing generations 4-6, 7-9, 10-12 and 13-15 respectively. The inlet conditions for generation 3 were taken from outlet 4 of combined nasal-oral airway model.

The inlet conditions for generation 3 were taken from outlet 4 of combined nasal-oral airway model. The nanoparticle concentration gradient on the wall indicates the mass flux near the wall. The deposition of nanoparticles on the wall can be calculated from the mass flux as described in equation (22). It has been noticed that the nanoparticle concentration gradient on wall increases with decreasing geometric dimensions. This is because the convection-diffusion drives the particle to the wall easily in a small geometry than geometry with larger

dimension. So for the given nanoparticle diameter, 37 nm, a higher nanoparticle deposition is expected in the deeper lung than in upper airways.

3.5.3 Flow structures and particle distribution in alveolar region

Fig. 3.9 shows the velocity vectors in the TBU model for generation 16-18. Enlarged view of the flow stream lines in an alveolar mid plane is also displayed. For the simulation, the alveolar wall was assumed to be rigid. Even though rigid wall assumption is not realistic, in the upper alveolar airways, in generations from 17-20, the alveolar wall movement is not significant enough to produce distinct alveolar flow. The prominent flow structure in an alveolus is the recirculation flow. The flow in the airway duct induces a shear flow across the alveolar mouth, thus generating a recirculation region in the alveolar cavity. The presence of alveoli around the duct produces a deflection among a small portion of duct flow in to the alveolar cavity. The size of the alveolar cavity is very less compared to the duct diameter. Hence the amount of duct air entering the alveoli is also less. Since a transient simulation was used in the 22-23 DBU, all the results were averaged over the cycle.

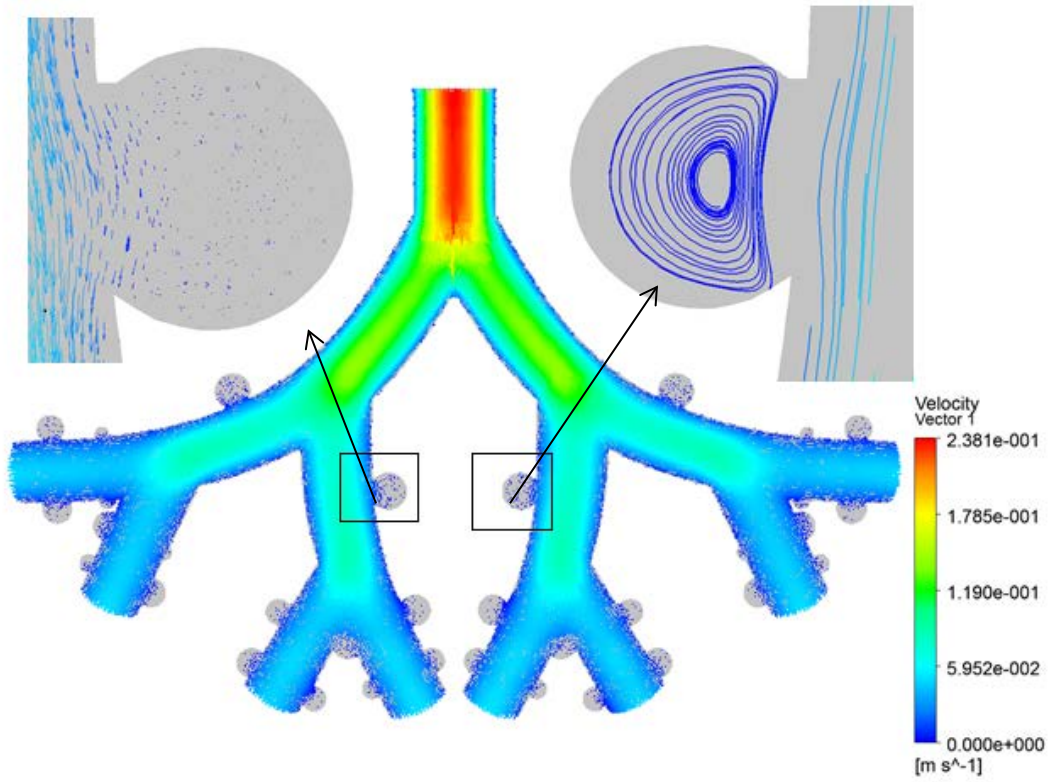

Fig. 3.9 shows the velocity vectors in the TBU model for generation 16-18 with an enlarged view of the flow stream lines in an alveolar mid plane.

Fig. 3.10 shows the velocity vectors and stream lines in the TBU model for generation 19-21. As mentioned earlier, the alveolar wall was assumed to be rigid which may not be realistic. But in the upper alveolar airways, in generations from 17-20, the alveolar wall movement is not significant enough to produce distinct alveolar flow. As mentioned earlier, the prominent flow structure in an alveolus is the recirculation flow.

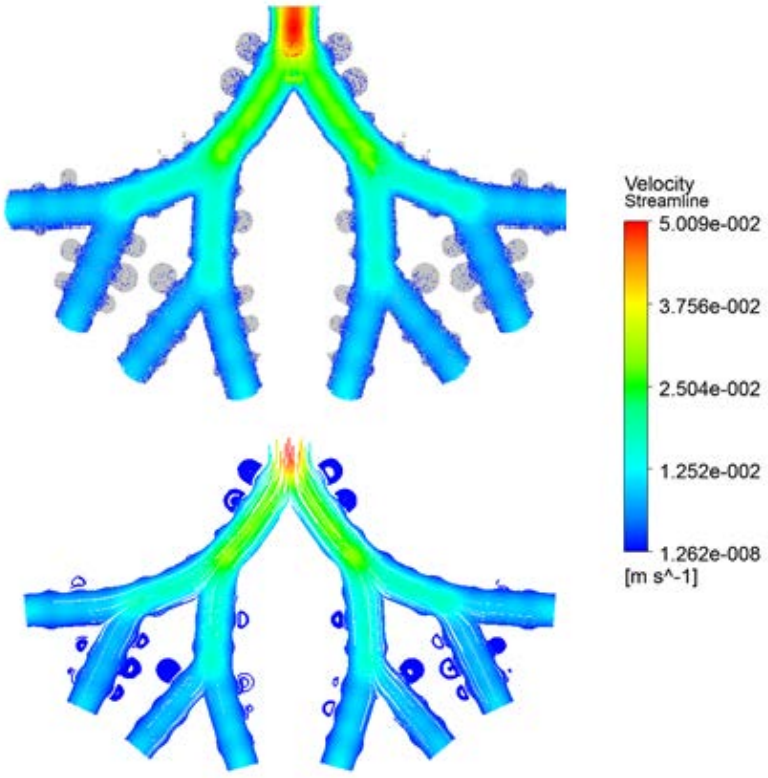

Fig. 3.10 shows the velocity vectors and stream lines in the TBU model for generation 19-21.

Figure 3.11 shows the velocity contour and stream lines in the DBU model for generation 22-23. Since DBU model for generation 22-23 is a sac model, a moving wall boundary condition was used for the 23 generation. Using one way coupled FSI modeling method, a 200 Pa pressure applied on the solid domain alveolar wall was converted to wall motion in the fluid domain. Instead of steady state simulation, a transient simulation with a pressure inlet boundary condition was used to model the flow. The geometrical dimension of the sphere representing the 23rd generation is larger than the duct diameter. Hence the alveolar flow phenomena are fundamentally different from a rigid wall alveolus case. Instead of recirculated flow, radial flow was noticed in the 23rd generation.

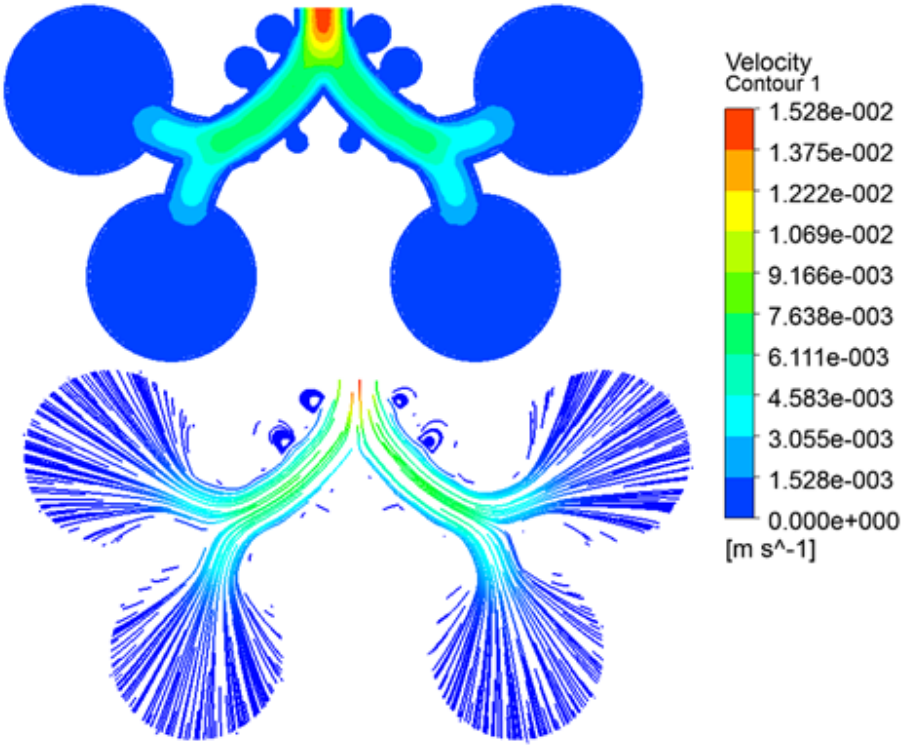

Fig. 3.11 shows the velocity contour and stream lines in the DBU model for generation 22-23.

Figure 3.12 displays the nanoparticle concentration contours and the nanoparticle concentration gradient on wall for the alveolar region. It is evident from the concentration contours that only a small percentage of the total nanoparticle concentration entered the alveolar cavity. The concentration gradient on alveolar wall is also less compared to that on duct. It may be because of the rigid wall assumption which prevents the tidal air mixing with the residual alveolar air. In the 23rd generation, even though wall movement was modeled, due to the reduced mass flow rate only a small fraction of the total flow entered the spherical geometry. The nanoparticle concentration followed the flow field results.

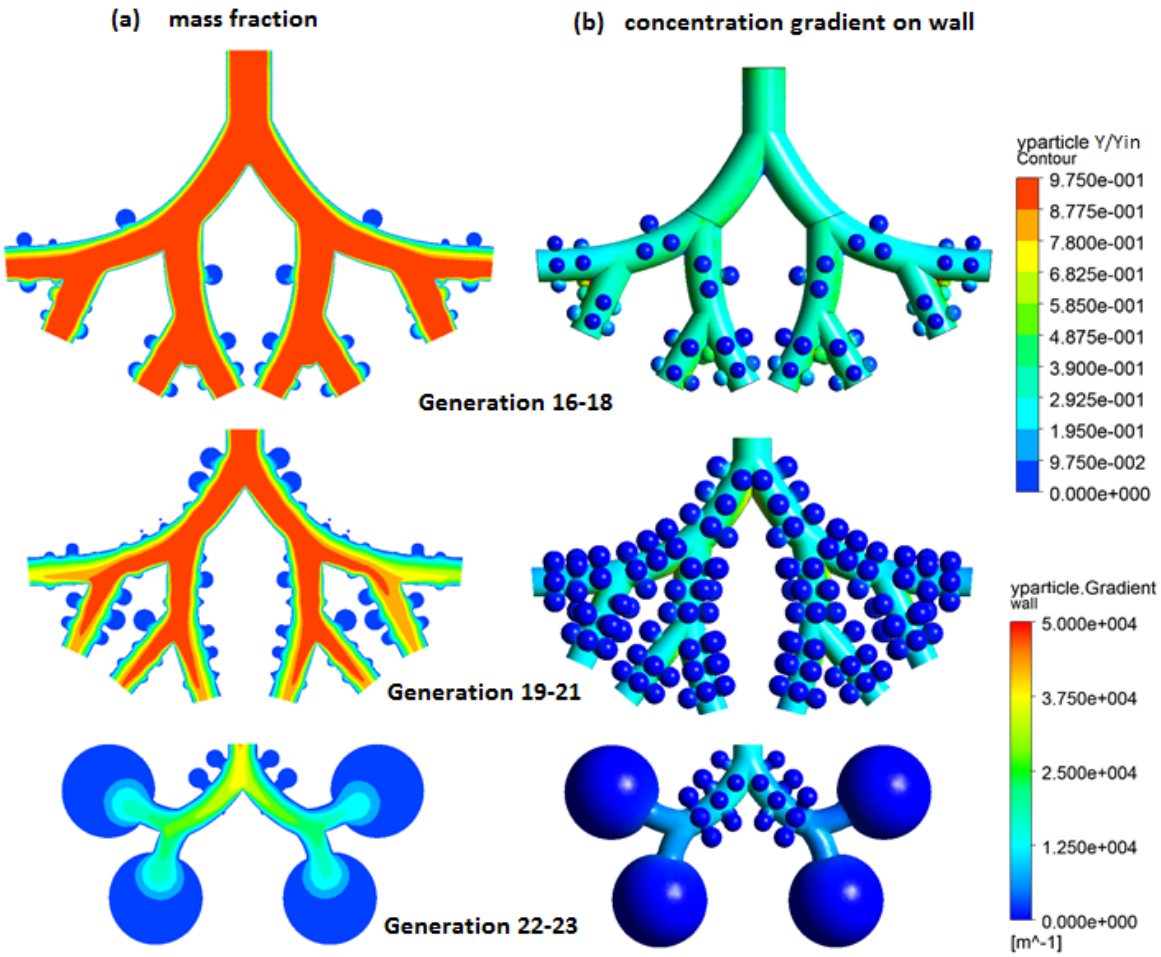

Fig. 3.12 displays (a) the nanoparticle concentration contours and (b) the nanoparticle concentration gradient on wall in the alveolar region of lungs.

3.6 Effect of alveolar wall movement on nanoparticle transport and deposition

The influence of alveolar wall motion on nanoparticle transport and deposition was analyzed using single generation model. Since alveolar wall movement was modeled using Fluid Structure Interaction (FSI), transient study with constant inlet velocity was used. It was found that, the alveolar wall movement in generations 17 to 23 resulted in an increased nanoparticle

deposition by 10-13 %. But considering the increased computing time and cost, the alveolar wall movement in generations 17 to 22nd was neglected and a spherical model with wall movement was used in the 23rd generation. Figure 3.13a shows the nanoparticle transport in generation 23rd with alveolar wall movement and Fig. 3.13b shows the nanoparticle transport without alveolar wall movement.

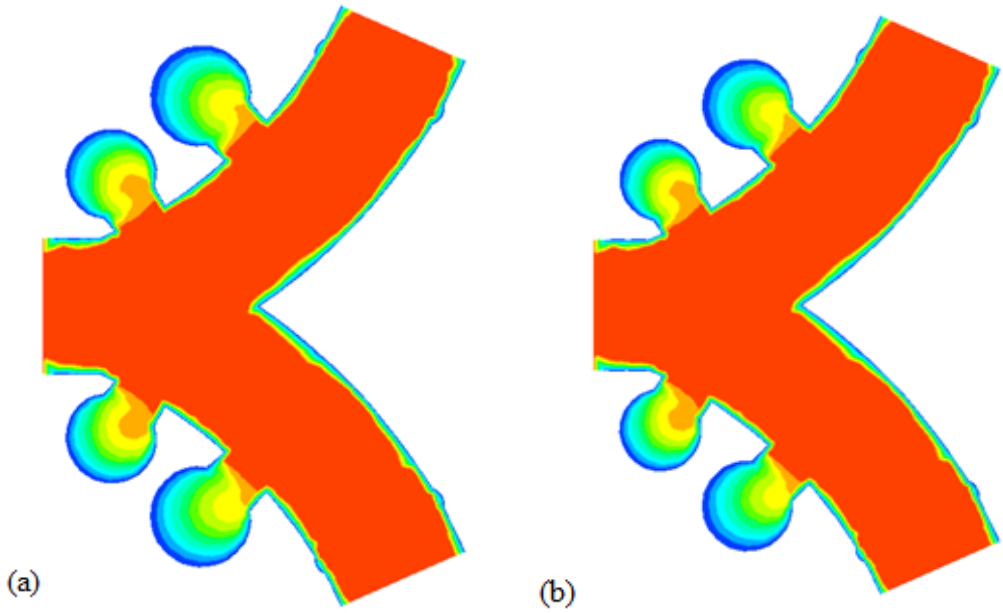

Fig. 3.13. Comparison of nanoparticle transport in generation 23rd (a) with alveolar wall movement, (b) without alveolar wall movement.

3.7 Effect of gravity on nanoparticle transport and deposition

The influence of gravity on nanoparticle transport and deposition were analyzed using the nasal-oral upper airway model. The deposition fractions in the model were compared with and without gravity as a body force in the vertical direction. The net difference between

nanoparticle deposition in the nasal-oral upper airway model under the influence of gravity and without gravity was less than 1%. Hence gravity force was neglected in all lung nanoparticle transport simulations.

3.8 Calculation of Deposition Fraction for 37 nm particles

The CFPD simulated lung deposition data is shown in Table 3.1 and Table 3.2. In Table 3.1, the deposition fraction was calculated using the Weibel (1963) lung morphometric data. The deposition fraction was calculated for airways in the left side of the lung (left upper lobe and left lower lobe). Based on the number of airways in each generation, the total deposition fraction was calculated. In Table 3.2, the deposition fraction was calculated from the deposition efficiency using Eq. 3.27 to 3.29. Table 3.3 and 3.4 shows the section wise DF values using the Weibel (1963) lung morphometric data and deposition efficiency method respectively. Deposition efficiency method takes into account the deposition in all upstream generations while calculating the deposition fractions while the morphometric data method depends only on the number of bifurcations in each generation. A residence time analysis study was conducted to analyze the time taken by nanoparticles to reach the deep lung generations.

Table 3.1 Lung deposition data from CFPD simulations using the Weibel (1963) lung morphometric data

TBU	MASS FLOW INLET	Jwall] =area int (D*(y.d/dn))	No of TBU's	divide by 4	Jwall both lungs	DEPOSITION FRACTION				
asal ,pharynx and laryn	3.06E-04	1.36E-06				4.44E-03				
0-3		7.78E-07				2.54E-03				
FROM OUTLET 1										
4 to 6	4.25E-05	2.66E-08	8	2	5.33E-08	1.74E-04				
7 to 9	5.54E-06	2.07E-08	64	16	3.31E-07	1.08E-03				
10 to 12	6.85E-07	9.79E-09	512	128	1.25E-06	4.09E-03				
13 to 15	8.54E-08	3.68E-09	4096	1024	3.77E-06	1.23E-02				
16	1.06E-08	1.72E-10	32768	8192	1.41E-06	4.60E-03				
17 to 18		5.12E-10	65536	16384	8.40E-06	2.74E-02				
19 to 21	1.30E-09	3.15E-10	262144	65536	2.06274E-05	6.74E-02				
22 - 23	1.72E-10	3.31E-11	2097152	524288	1.73594E-05	5.67E-02	TB sum	6.93E-03		
FROM OUTLET2						(4)	bronchiolar sum	7.07E-02	extra-thoracic	4.44E-03
4 to 6	1.92E-05	2.07E-08	8	2	4.13E-08	1.35E-04	alv sum 17 to 18	9.53E-02	TB	6.93E-03
7 to 9	2.39E-06	1.41E-08	64	16	2.25E-07	7.35E-04	alv sum 19 to 21	0.231643492	Bronchiolar	7.07E-02
10 to 12	2.99E-07	5.84E-09	512	128	7.47E-07	2.44E-03	alv 22-23	1.80E-01	Alveolar	5.07E-01
13 to 15	3.74E-08	1.87E-09	4096	1024	1.92E-06	6.27E-03				
16	4.69E-09	1.11E-10	32768	8192	9.10E-07	2.97E-03	alveolar sum	5.07E-01		
17 to 18		3.05E-10	65536	16384	4.99E-06	1.63E-02				
19 to 21	5.74E-10	1.70E-10	262144	65536	1.11181E-05	3.63E-02				
22 - 23	8.87E-11	1.31E-11	2097152	524288	6.84973E-06	2.24E-02				
FROMOUTLET 3						(5)				
4 to 6	2.65E-05	2.33E-08	8	2	4.66E-08	1.52E-04				
7 to 9	3.92E-06	1.70E-08	64	16	2.72E-07	8.90E-04				
10 to 12	4.92E-07	7.76E-09	512	128	9.93E-07	3.24E-03				
13 to 15	6.16E-08	2.62E-09	4096	1024	2.68E-06	8.75E-03				
16	7.74E-09	1.52E-10	32768	8192	1.25E-06	4.07E-03				
17 to 18		4.13E-10	65536	16384	6.77E-06	2.21E-02				
19 to 21	9.47E-10	2.43E-10	262144	65536	1.59384E-05	5.20E-02				
22 - 23	1.91E-10	2.31E-11	2097152	524288	1.21112E-05	3.95E-02				
FROMOUTLET 4						(2)				
4 to 6	5.42E-05	2.48E-08	8	2	4.97E-08	1.62E-04				
7 to 9	7.23E-06	2.03E-08	64	16	3.24E-07	1.06E-03				
10 to 12	8.76E-07	1.04E-08	512	128	1.33E-06	4.33E-03				
13 to 15	1.09E-07	3.71E-09	4096	1024	3.80E-06	1.24E-02				
16	1.37E-08	1.96E-10	32768	8192	1.61E-06	5.25E-03				
17 to 18		5.52E-10	65536	16384	9.04E-06	2.95E-02				
19 to 21	1.68E-09	3.55E-10	262144	65536	2.32569E-05	7.59E-02				
22 - 23	1.90E-10	3.62E-11	2097152	524288	1.89554E-05	6.19E-02				

Table 3.2. Lung deposition data from CFPD simulations using the deposition efficiency method

TBU	yparticle in	MASS FLOW INLET	Qin*Yparticle in	Jwall]=area int(D*(y.d/dn))	DE					
nasal, pharynx and larynx	1.00000	3.06E-04	3.06E-04	1.36E-06	4.44E-03					
0-3	0.98092	3.06E-04	3.00E-04	7.78E-07	2.59E-03					
FROM OUTLET1										
4 to 6	0.95568	4.25E-05	4.06E-05	2.66E-08	6.56E-04					
7 to 9	0.96771	5.54E-06	5.36E-06	2.07E-08	3.86E-03					
10 to 12	0.95339	6.85E-07	6.54E-07	9.79E-09	1.50E-02		average DE	DF		
13 to 15	0.93931	8.54E-08	8.02E-08	3.68E-09	4.59E-02	nasal	4.44E-03			
16	0.89050	1.06E-08	9.47E-09	1.72E-10	1.81E-02	0-3	2.59E-03	0.00257868		
17 to 18	0.89050	5.32E-09	4.73E-09	5.12E-10	1.08E-01	4 to 6	7.91E-04	0.000785687	extra-thoracic	0.004437
19 to 21	0.80855	1.30E-09	1.05E-09	3.15E-10	3.00E-01	7 to 9	4.34E-03	4.30E-03	TB	7.67E-03
22 - 23					4.27E-01	10 to 12	1.61E-02	1.59E-02	Bronchiolar	7.91E-02
FROM OUTLET2					(4)	13 to 15	4.52E-02	4.39E-02	Alveolar	6.03E-01
4 to 6	0.96640	1.92E-05	1.85E-05	2.07E-08	1.12E-03	16	2.08E-02	1.93E-02		
7 to 9	0.96574	2.39E-06	2.31E-06	1.41E-08	6.09E-03	17 to 18	1.16E-01	1.06E-01		
10 to 12	0.95465	2.99E-07	2.85E-07	5.84E-09	2.05E-02	19 to 21	3.21E-01	2.57E-01		
13 to 15	0.93049	3.74E-08	3.48E-08	1.87E-09	5.39E-02	22-23	4.39E-01	2.40E-01		
16	0.86999	4.69E-09	4.08E-09	1.11E-10	2.72E-02					
17 to 18	0.86999	2.35E-09	2.04E-09	3.05E-10	1.49E-01					
19 to 21	0.75462	5.74E-10	4.33E-10	1.70E-10	3.92E-01					
22 - 23		1.33E-10			5.36E-01					
FROM OUTLET3					(5)					
4 to 6	0.96008	2.65E-05	2.54E-05	2.33E-08	9.16E-04					
7 to 9	0.96011	3.92E-06	3.77E-06	1.70E-08	4.52E-03					
10 to 12	0.95074	4.92E-07	4.68E-07	7.76E-09	1.66E-02					
13 to 15	0.93512	6.16E-08	5.76E-08	2.62E-09	4.54E-02					
16	0.88999	7.74E-09	6.89E-09	1.52E-10	2.21E-02					
17 to 18	0.88999	3.87E-09	3.44E-09	4.13E-10	1.20E-01					
19 to 21	0.77516	9.47E-10	7.34E-10	2.43E-10	3.31E-01					
22 - 23					3.95E-01					
FROM OUTLET4					(2)					
4 to 6	0.96142	5.42E-05	5.21E-05	2.48E-08	4.77E-04					
7 to 9	0.97216	7.23E-06	7.03E-06	2.03E-08	2.88E-03					
10 to 12	0.96451	8.76E-07	8.45E-07	1.04E-08	1.23E-02					
13 to 15	0.95390	1.09E-07	1.04E-07	3.71E-09	3.56E-02					
16	0.91499	1.37E-08	1.26E-08	1.96E-10	1.56E-02					
17 to 18	0.91499	6.87E-09	6.29E-09	5.52E-10	8.78E-02					
19 to 21	0.81387	1.68E-09	1.37E-09	3.55E-10	2.60E-01					
22 - 23					3.98E-01					

Table 3.3. Lung deposition fraction calculated based on region of deposition using the Weibel (1963) lung morphometric data

	CFPD simulation
Extra-thoracic	0.00444
TB	0.00693
Bronchiolar	0.0707
Alveolar	0.507
Total	0.589

Table 3.4. Lung deposition fraction calculated based on region of deposition using the deposition efficiency method

	CFPD simulation
Extra-thoracic	0.004437
TB	0.00767
Bronchiolar	0.0791
Alveolar	0.603
Total	0.6942

3.9 Residence Time Analysis

During slow inhalation conditions, due to reduced mass flow rate, the nanoparticles may not reach the 22nd and 23rd generations. A resident time analysis may be helpful in understanding the reachability of nanoparticles. For this study an initial mass flow rate of 15 L/min was assumed as the initial mean nasal inspiratory flow rate which corresponds to a breathing condition at rest (Kim and Jaques, 2005). Usually in this condition the breathing cycle lasts for 4 to 8 sec from which an inspiratory phase of 2 to 4 sec can be assumed. If the total residence time of nanoparticles during inspiration exceeds the inspiratory phase, it can be assumed that these particles will be exhaled without depositing. Hence the nanoparticles with total residence time more than inspiratory phase were excluded from the calculation of inspiratory deposition. The residence time was calculated based on domain average velocity. But higher air velocity at the center and diffusion of nanoparticles could affect the deposition of nanoparticles in deeper lung airways. Table 3.5 shows the residence time in each bifurcation units. It can be noticed that the residence time exceeds 2 sec before reaching the final DBU model for generation 22-23 in all lung lobes. Hence only the nanoparticles which were deposited in the final DBU 22-23 with in the inspiratory phase need to be considered, instead of total deposition. A ratio of distance travelled in the 22-23 DBU during the inspiratory phase to the total length of 22-23 DBU was used to calculate the final deposition fraction in the 22-23 DBU model.

Table 3.5. Residence time analysis for the upper and lung airways

TBU	Avg. length (m)	Avg. velo (m/s)	Residence time (s)	Total Residence Time
nasal	0.1225603	0.47694	0.256972156	From nose to generation 3
nasopharynx	0.06975	0.638045	0.109318308	
oropharynx	0.05729	0.214512	0.267071306	
trachea	0.2364278	0.531918	0.444481668	1.077843438
FROM OUTLET1				From generation 4 to generation 23 of left upper lobe followed from outlet 1
4 to 6	0.0507165	0.601838	0.084269355	
7 to 9	0.02346	0.354589	0.066161105	
10 to 12	0.0112802	0.187888	0.06003683	
13 to 15	0.0053644	0.10286	0.052152635	
16 to 18	0.0025733	0.0319978	0.080421779	
19 to 21	0.0019050	0.00347195	0.548685897	
22 - 23	0.0014954	0.00040325	3.708567886	4.600295487
FROM OUTLET4				From generation 4 to generation 23 of left lower lobe followed from outlet 4
4 to 6	0.051899	0.724045	0.071679246	
7 to 9	0.0241895	0.437433	0.055298754	
10 to 12	0.0112476	0.240931	0.046683905	
13 to 15	0.0053600	0.132572	0.040431162	
16 to 18	0.0026996	0.0377417	0.071529369	
19 to 21	0.0019923	0.00407014	0.489491762	
22 - 23	0.0015803	0.00046495	3.398989139	4.174103338
FROM OUTLET2				From generation 4 to generation 23 of left upper lobe followed from outlet 2
4 to 6	0.0031738	0.681813	0.004655001	
7 to 9	0.0151299	0.366348	0.041299256	
10 to 12	0.0072101	0.197699	0.036470341	
13 to 15	0.0034751	0.107511	0.032323204	
16 to 18	0.0017551	0.0305715	0.05741066	
19 to 21	0.0013084	0.00329616	0.396971021	
22 - 23	0.0011993	0.00032821	3.654154352	4.223283836
FROM OUTLET3				From generation 4 to generation 23 of left lower lobe followed from outlet 3
4 to 6	0.0388681	0.608197	0.063907089	
7 to 9	0.0187118	0.38661	0.048399679	
10 to 12	0.0090321	0.208573	0.043304263	
13 to 15	0.0043332	0.113157	0.038293698	
16 to 18	0.0021519	0.03217	0.066894311	
19 to 21	0.0016207	0.00346803	0.467340248	
22 - 23	0.0015357	0.0003694	4.157363292	4.885502581

The final alveolar deposition fraction was calculated after subtracting the excess deposition based on the residence time analysis. The CFPD results were compared with experimental results of Kim and Jaques (2005) for 40 nm particles and MPPD (details about the MPPD software is given in appendix A1) results for 37 nm particles. Kim and Jaques (2005) measured the deposition fractions of 40 to 100 nm particles in lungs of healthy elderly human. Based on the inhalation conditions three cases where considered: 15 L/min mass flow rate with an inspiratory phase of 2, 3 and 4 sec (breathing cycle of 15 breaths/min, 10 breaths/min and 7.5 breaths/min respectively). Table 3.6 and 3.7 shows the final segmental airway deposition fraction for an inspiratory phase of 2 sec using the Weibel (1963) lung morphometric data and deposition efficiency method respectively. Table 3.8 and 3.9 shows the final segmental airway deposition fraction for an inspiratory phase of 3 sec using the Weibel (1963) lung morphometric data and deposition efficiency method respectively. Table 3.10 and 3.11 shows the final segmental airway deposition fraction for an inspiratory phase of 4 sec using the Weibel (1963) lung morphometric data and deposition efficiency method respectively. The CFPD airway deposition values agree well with the experimental results. It was noticed from the results that as the residence time increases, the deposition also increases. It is because of the higher deposition in the deeper lung regions. When the breathing period is long, particles will get longer time to reach the deeper lung regions.

Deposition efficiency method takes into account the deposition in all upstream generations while calculating the deposition fractions while the morphometric data method depends only on the number of bifurcations in each generation. Comparing the CFPD results to the

experimental and analytical deposition data, it can be concluded that the deposition efficiency method gives better results than the morphometric data method.

Multiple-Path Particle Dosimetry (MPPD) program was used to determine the analytical deposition data in the olfactory, upper airways and alveolar regions. This program can calculate deposition and clearance of aerosols in rats and humans given information about the particle characteristics, exposure conditions, and breathing patterns. The program can be downloaded from http://www.ara.com/products/mppd.htm. MPPD model use statistical equations to calculate the deposition of particles inside lung airways. The nanoparticle Model of the MPPD program uses convection-diffusion mass transfer equation to model the transport of nanoparticles. The MPPD model does not consider the effect of turbulence on nanoparticle transport and deposition. Also the model is based on a simplified geometry which assumes the lung airways as cylindrical tubes.

Table 3.6. Comparison of regional lung deposition fraction calculated based on Weibel (1963) lung morphometric data with MPPD and experimental results for an inspiratory phase of 2 sec

	CFPD simulation	MPPD	Kim and Jaques (2005) for 40 nm particles
Extra-thoracic	0.00444	0.099	
TB	0.00693	0.0357	
Bronchiolar	0.0707	0.115	
Alveolar	0.334	0.231	
Total	0.416	0.481	0.43±0.03

Table 3.7. Comparison of regional lung deposition fraction calculated based on deposition efficiency method with MPPD and experimental results for an inspiratory phase of 2 sec

	CFPD simulation	MPPD	Kim and Jaques (2005) for 40 nm particles
Extra-thoracic	0.004437	0.099	
TB	0.00767	0.0357	
Bronchiolar	0.0791	0.115	
Alveolar	0.3748	0.231	
Total	0.466	0.481	0.43±0.03

Table 3.8. Comparison of regional lung deposition fraction calculated based on Weibel (1963) lung morphometric data with MPPD and experimental results for an inspiratory phase of 3 sec

	CFPD simulation	MPPD	Kim and Jaques (2005) for 40 nm particles
Extra-thoracic	0.00444	0.091	
TB	0.00693	0.0366	
Bronchiolar	0.0707	0.127	
Alveolar	0.383	0.345	
Total	0.465	0.6	0.53 ± 0.04

Table 3.9. Comparison of regional lung deposition fraction calculated based on deposition efficiency method with MPPD and experimental results for an inspiratory phase of 3 sec

	CFPD simulation	MPPD	Kim and Jaques (2005) for 40 nm particles
Extra-thoracic	0.004437	0.091	
TB	0.00767	0.0366	
Bronchiolar	0.0791	0.127	
Alveolar	0.4395	0.345	
Total	0.531	0.6	0.53 ± 0.04

Table 3.10. Comparison of regional lung deposition fraction calculated based on Weibel (1963) lung morphometric data with MPPD and experimental results for an inspiratory phase of 4 sec

	CFPD simulation	MPPD	Kim and Jaques (2005) for 40 nm particles
Extra-thoracic	0.00444	0.087	
TB	0.00693	0.037	
Bronchiolar	0.0707	0.133	
Alveolar	0.432	0.409	
Total	0.514	0.665	0.62 ± 0.06

Table 3.11. Comparison of regional lung deposition fraction calculated based on deposition efficiency method with MPPD and experimental results for an inspiratory phase of 4 sec

	CFPD simulation	MPPD	Kim and Jaques (2005) for 40 nm particles
Extra-thoracic	0.004437	0.087	
TB	0.00767	0.037	
Bronchiolar	0.0791	0.133	
Alveolar	0.5156	0.409	
Total	0.595	0.665	0.62 ± 0.06

3.10 Calculation of Deposition Fraction for 17 nm particles

In order to estimate the parameters (transfer rates) for the multi-compartment human lung model, simulations were conducted to calculate the lung nanoparticle deposition based on the experimental conditions in Semmler et al. (2004). The utility of the experimental results from Semmler et al. for the multi-compartment human lung model is described in chapter 6 and chapter 7. Semmler et al used an endotracheal inhalation procedure to transport the nanoparticles in to the rat lung. Also the ventilation process was controlled using a computer and the breathing frequency was almost half the normal frequency. Hence for the CFPD simulation, in order to replicate the endotracheal inhalation process, the inlet was specified at the start of tracheal tube, instead of the nasal inlet. Also the breathing frequency was fixed to half (7.5 breaths per minute) of the normal frequency but with the same flow rate 15 L/min. The residence time analysis method was used to calculate the residence time and deposition fraction based on an inspiratory phase of 4s. Because the flow was started form trachea, it was found that most of the nanoparticles reached the 23^{rd} generation with in the inspiratory phase of 4s. The results from these CFPD simulations were used in chapter 7 to estimate the parameters (transfer rates) for the multi-compartment human lung model. Since it was concluded that the deposition efficiency method is better than the lung morphometric method, only the later method was used to calculate the nanoparticle deposition. The nanoparticle deposition in the deeper lung regions was found to be very high because of the endotracheal inhalation. Table 3.12 displays the lung deposition fraction for a 17 nm particles calculated based on region of deposition using the deposition efficiency method

Table 3.12. Lung deposition fraction calculated based on region of deposition using the deposition efficiency method

	CFPD simulation DF	DF after residence time analysis
Extra-thoracic	0	0
TB	0.0159	0.0159
Bronchiolar	0.144	0.144
Alveolar	0.745	0.691891677
Total	0.905	0.852196132

3.11 Discussion

In this study, the nanoparticle transport and deposition in a human lung was simulated numerically. Realistic nasal-oral upper airway geometry was used to simulate the nanoparticle transport in the extra thoracic region. The lung airway generations 4-16 were approximated as a geometrically scaled Triple Bifurcation Unit (TBU) models based on Weibel (1963) lung morphometric data. The alveolar airways from generations 17 to 23 were also approximated as a geometrically scaled Triple Bifurcation Unit (TBU) models with alveoli attached to the lumen surface. The alveolar dimensions were based on Weibel (1963) lung morphometric data.

The CFPD simulated deposition data agrees well with the experimental results. But comparing the regional deposition CFPD results with the analytical results of MPPD, differences were noticed in the nasal-oral and alveolar regions. In the nasal-oral region as per

the MPPD model calculation, a high deposition fraction of 0.091 was predicted. But the CFPD simulated deposition results suggests a deposition fraction of 0.0044. In the alveolar region the CFPD simulated deposition results suggests a high deposition fraction than MPPD. The CFPD results are comparable with the numerical results of Xi and Longest (2008) in which they calculated the nanoparticle deposition in an oral airway numerically. For a 50 nm, they predicted a deposited efficiency of 0.004 in the oral airway which is close to the extra thoracic airway deposition fraction predicted by the CFPD simulation. In the alveolar region further investigation must be done to confirm the results. Comparing the CFPD results to the experimental and analytical deposition data, it can be concluded that the deposition efficiency method gives better results than the morphometric data method.

The alveolar wall movement might be a significant factor in nanoparticle deposition, which will be added to the existing models in future. Simulations using individual lung generation models have shown that the alveolar nanoparticle deposition can increase by 10-13% because of the alveolar wall movement. But the computational time and cost required for such models are very high.

The distribution of nanoparticle is mainly controlled by the convective diffusion, Brownian diffusion and turbulent dispersion. Mass flow rate of the fluid and size of the nanoparticle are the two significant parameters which influence the nanoparticle distribution and deposition. It can be noticed that the mass fraction distributions has a high resemblance with the velocity field contours, which indicates that the nanoparticles closely follows the fluid flow. It was noticed that the flow and particle transport/deposition history (i.e., upstream, asymmetric

velocity profiles and particle distributions) has a more significant effect on particle deposition. In the upper airways, large asymmetry was noticed for flow rates and velocity profiles even in parallel TBUs. But in smaller airways the air flow became more symmetric, laminar with reduced secondary flow structures. Hence the nanoparticle deposition is more uniform in small airways than in upper large airways. In the upper alveolar airway generations the effect of alveoli on particle deposition tends to be negligible, but in the deeper alveolar airways, they have significant influence on particle deposition.

A significant shortcoming of the current numerical study is approximation of the tracheobronchial and alveolar airway geometry. Realistic lung airways are asymmetric and non-planar which can influence the fluid flow and particle distribution. However as reported by Zhang et al. (2008), the geometrical differences have negligible effect on nanoparticle transport and deposition. Another limitation of the current study is that it neglects particle inertia effects. Even though the particle inertia effects are negligible for nanoparticle especially when the diameter d_p<40nm, it can significantly influence the local nanoparticle deposition characteristics. Another short coming of the current study is the assumption of steady flow. Previous studies have pointed out the influence of transient breathing on sub-micron particle deposition. Sosnowski et al. (2006) have highlighted the effects of transient breathing on particle deposition. Also Zhang et al. (2008) suggested that the cyclic breathing patterns have only negligible influence on nanoparticle distribution and deposition. They also reported that particle deposition under transient inspiratory flow conditions can be approximated as the deposition under equivalent steady conditions with matching Reynolds

numbers, which essentially fall into the middle of mean and maximum Reynolds numbers of an inhalation cycle. Jiang et al. (2010) compared the deposition efficiency of nanoparticles in a rat nasal model during steady and cyclic breathing conditions. They reported that the total nanoparticle deposition during a cyclic breathing condition is lower than that of a steady state condition. Since the alveolar wall movement was neglected, the calculated lung nanoparticle deposition is less than original. Hence the error produced due to the steady state assumption may be compensated with the error produced due to rigid alveolar wall assumption. Also SST k-ω turbulence model cannot capture all turbulent features of the flow, which may affect the particle distribution simulation. Higher order turbulence models like LES and DNS can be used in future simulations to improve the accuracy of the results. These limitations should be addressed in future studies in order to better predict nanoparticle transport and deposition.

PART 2

MULTI-COMPARTMENTAL MODEL

CHAPTER 4

MULTI-COMPARTMENTAL MODEL REPRESENTING THE BIOKINETICS OF INHALED ULTRAFINE PARTICLES

4.1 Introduction

Particle retention and clearance is a major concern in lung related disease treatment. Inhalation carries gases, liquid droplets and soluble and insoluble particulate materials in to the lung airways. Among these particulate materials some can be useful, for example when aerosol droplets containing inflammation-reducing steroids are inhaled to treat asthma. Unfortunately, they can also be harmful, such as when asbestos fibers (or other toxic materials) are inhaled by workers. From the epidemiological and pathological studies of occupational and environmental exposures to airborne particles and fibers, it can be concluded that many of the lung related diseases are an outcome of these inhaled aerosols. Ultrafine particles, which constitute a major portion of the urban particulate air pollution, are found to have increased toxicity than larger particles made of the same material. But the dosimetry of ultrafine particles in the human lung is poorly characterized. Deposition and disposition of inhaled ultrafine particles are different from that of larger particles. Studies related to particle deposition and removal from the lungs are of great importance since accumulation and retention of these particles can result in serious lung diseases like chronic bronchitis, lung fibrosis, silicosis, asbestosis, lung cancer etc. Mathematical models and associated computer simulations, which can predict possible particulate lung burden for specific parameters of exposure conditions, can offer valuable assistance in developing new preventive strategies. Also ultrafine particles have a large surface area per mass which makes

it suitable for many bio-applications such as carrier for pulmonary drug delivery, catalyst for specific reactions and so on. Optimization of pulmonary nano-drug delivery requires appropriately accurate deposition, retention and clearance models and knowledge about the mass of drugs to be deposited. So a good lung dosimetry model is required for efficient pulmonary drug delivery. In this study a multi-compartmental model representing the bio-kinetics of nanoparticles in the pulmonary region of the lung was created. The model was quantified by a set of differential equations describing the transfer of particles between compartments.

Particulate deposition and retention in the lungs are a potential cause of serious lung problems. Insoluble particles have a long retention time in the lung than soluble particles. These particles affect the normal lung processes and they change the lung material structure leading to lung fibrosis, chronic bronchitis, pneumoconiosis, silicosis, asbestosis, and lung cancer. Usually, these particle deposits are formed during chronic exposures to certain respirable particles. Chronic inhalation of urban particulate air pollution may lead to particulate lung deposits and potential health risks. Particulate air pollution has also been associated cardiovascular diseases and neurodegenerative effects. Aerosol particles can be categorized based on their mean diameter namely ultrafine or nano, fine and coarse. Ultrafine particles (those of < 100 nm in mean diameter) contribute very little to the overall mass, but are very high in number in the urban air. Epidemiological studies have shown that ultrafine particles can easily reach the deeper lung regions and cause pulmonary inflammation. Pulmonary toxicity caused by ultrafine particles is an ongoing research field. In fact there are evidences which suggest that ultrafine particles are more toxic that any larger particles.

Hence widely used nanoparticles, which are part of ultrafine particles, may cause negative health effects when inhaled. Clearly, the rapid development of nanoparticle applications needs to be complemented by assessing possible negative health implications (Holgate, 2010). Specifically a lung dosimetry model for ultrafine particles deposition, retention and translocation could help in making advances in the field of risk assessment and developing preventive strategies.

Learning from environmental toxicology studies, nano-sized solid materials easily enter the lungs and may reach the alveoli. Subsequently they will be cleared from the lungs to the extra-pulmonary sites by different clearance mechanisms. It has been proved by experiments on lab animals that inhaled nanoparticles quickly translocate from the lungs to be deposited in extra-pulmonary organs. Thus translocation to extra-pulmonary sites after deposition in the respiratory tract represents an important mechanism for these particles to cause direct effects in secondary target organs. Considering drug-aerosols this makes ultrafine particles a suitable medium for pulmonary drug delivery. The route of drug administration is as important as the drug itself for therapeutic success. Nanodrug delivery through the lungs is focused on crossing cell-blood barrier and on finding alternative routes for the delivery of drugs vulnerable to the gastro-intestinal environment. Pulmonary delivery of drugs at the nano-level is a non-invasive promising means to provide not only local lung effects but also high systemic bioavailability. The high surface-to-volume ratio of nanoparticles makes them more reactive, even though they are inert as larger particles. Therefore, any possible effects of the nanoparticles may be amplified once entering the body via inhalation. Optimization of pulmonary nanodrug delivery requires appropriately accurate deposition, retention and

clearance models and knowledge about the mass of drugs to be deposited. Again a good lung dosimetry model is required for efficient pulmonary drug delivery as well.

Studies have shown that the ultrafine particles deposited in the alveolar region of the lungs are not easily phagocytized. However experiments conducted on rodents demonstrate that ultrafine particles can easily break the epithelial cell barrier and reach the blood/lymph circulation system. Inhaled nanoparticles may end up in systemic circulation and the lymphatic system once they reach the pulmonary interstitial sites following transcytosis across alveolar epithelial cells (Oberdörster et al., 2005). The nanoparticles sequestered by the macrophages may also be transported to regional lymph nodes and may subsequently migrate to systemic circulation. Particle-loaded macrophages were seen in pulmonary lymphatic vessels and in hilar lymph nodes of animals following instillation of particulates into the airways. Recently, it was reported that inhaled nano-materials may also influence organs other than the lungs. Inhaled ultrafine technetium (99 mTc) labeled carbon particles diffused into the systemic circulation of hamsters within 5 min. For example, Nemmar et al., (2001) concluded that phagocytosis by macrophages and endocytosis by epithelial and endothelial cells may be responsible for particle-translocation to the blood, along with other mechanisms. Nemmar et al., (2002) conducted studies on human lungs and reported a rapid 3–5% uptake of radio-labelled carbonaceous ultrafine particles into the bloodstream within minutes after exposure and subsequent uptake in the liver. There are recent reports that inhaled nanoparticles have been found in the brain, probably traveling from the nasal nerves (Donaldson et al., 2004). This suggests that nanoparticles may travel to sites quite far away from the site of deposition in the lungs. Oberdörster et al., (2002) reported rapid translocation

of carbon nanoparticles with a diameter of 26 nm to the liver, occurred within 24 h following inhalation in to a rat lung. Kato et al., (2003) reported that inhaled polystyrene particles were transported into the pulmonary capillary space, presumably by transcytosis. In another study by Kreyling et al., (2002) on rats, only less than 1% iridium nanoparticles (15–20 nm in diameter) were found in secondary organs, but the nanoparticles were distributed widely throughout the body to such organs as liver, spleen, kidneys, brain and heart. Semmler et al., (2004 and 2007) found evidence for transfer of nanoparticles from the alveolar epithelial surface to interstitial space. They also reported quantitative data of extra pulmonary particle uptake. They measured the ultrafine particle mass fraction translocated in secondary organs such as the liver, spleen, brain and kidney. Extra pulmonary translocation has also been described for poorly soluble ultra-fine gold and Ir particles. Geiser et al., (2005) found that both ultra-fine and fine particles cross cellular membranes by non-endocytic mechanisms. In a study conducted on rats exposed to ultra-fine gold particles (5-8 nm), Takenaka et al., (2006) reported a low but significant fraction of gold translocated to blood. Oberdörster et al., (2004) conducted studies on ultra-fine particle migration to central nervous system by exposing rats to ultra-fine carbon particles containing ^{13}C in a whole-body chamber for 6 h. The distribution of ^{13}C was followed for 7 days post exposure. There was a significant increase in ^{13}C in the olfactory bulb on Day 1 with persistent and continued increase through day 7. Elder et al., (2006) has reported the transfer of inhaled Mn oxide ultrafine particles to the central nervous system through the olfactory neuronal pathway. Wang et al., (2007) reported the translocation of both fine and ultra-fine TiO2 particles to the olfactory bulb in mice. Nevertheless, other research groups did not find any detectable particulates in the body

other than the lungs (Brown et al., (2002) and Mills et al., (2006)). Figure 4.1 displays the nanoparticle translocation from lung epithelium to regional lymph nodes, blood circulation and secondary organs.

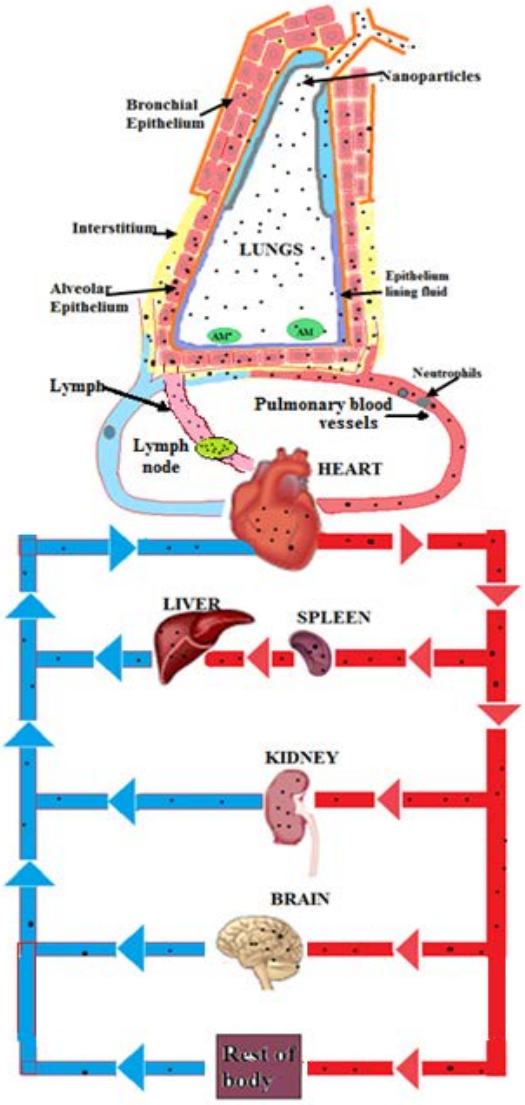

Fig. 4.1. Nanoparticle translocation from lung epithelium to regional lymph nodes, blood circulation and secondary organs.

Mathematical models have been used to describe the retention and clearance phenomena of deposited particles form the pulmonary region of the lungs. Initially the clearance process was modeled using simple mathematical equations depicting first order reaction kinetics (Albert et al., 1955). Later compartmental models were used to model the bio kinetics of particle clearance. Strom et al., (1987) developed a compartmental model with nonlinear transfer rates for macrophage mediated clearance processes. Smith et al., (1985) used Michaelis-Menten kinetics to model the transfer kinetics. Vincent et al., (1987) came up a sequestration model to account for the slow clearance process. Later physiology-oriented compartmental model composed of several sub-compartments in the pulmonary region of the lung, including an interstitial compartment were developed (Morrow et al., 1988, Stober et al., 1989). Stober et al., (1989, 1990a, 1990b) postulated that particle burdens in alveolar macrophages would progressively reduce alveolar clearance by decreasing the macrophage mobility down to total mobility loss once the particle burden exceeds a critical volume (overload phenomenon). Katsnelson et al., 1992 published a multi-compartmental retention model of bio persistent particles in the pulmonary region of the lung. They included neutrophils which also engage in phagocytosis and contribute to alveolar clearance by transfer with their particle load onto the mucociliary escalator.

International Committee on Radiological Protection (ICRP-1994) developed a particle clearance model (Human Respiratory Tract Model, HRTM) based on a great variety of human data for accidental occupational or other aerosol exposures that resulted in lung burdens of small masses of bio-persistent radioactive particles. The model design also covers aerosols with slow dissolution rates. Tran et al., (1999) developed a multi-compartmental

model focusing on the alveolar region of the lung. They modeled sequestration of particles using separate compartments. Also they considered the decay of macrophages of both alveolar surface and interstitium and the overload phenomenon. Kuempel et al., (2001a) modeled the lung clearance of coal miners using three compartments. They used alveolar, interstitial and hilar lymph node compartments. MacCalman et al., (2009) developed a multi-compartmental model focusing on disposition of inhaled nanoparticles from lungs to other secondary organs. Sturm (2007) created a multi–compartmental model for the tracheobronchial region of the lung. Quantifying the transfer rates for these parameters requires experimental data. But human data are limited, but quantitative data are available from rodent studies. Much of the information on the dosimetry of nanoparticles comes from experiments conducted on lab animals. Optimal use of these data requires extrapolation to the human scenario (Kuempel 2000, Kuempel et al., 2002, and Brown et al., 2005).

Prediction of the impact of nanoparticles on humans is not easy. Since experimental data using nanoparticles on humans are limited, one has to rely on other rational methodologies. During the past years a number of lung models have been developed for examining particle deposition, retention and transfer. These models are developed based on the bio-kinetics of particles in the lung. In this study a multi-compartmental model representing the bio-kinetics of nanoparticle translocation and retention in the pulmonary region of the lung was created. The model was quantified by a set of differential equations describing the transfer of particles between the compartments.

4.2 Multi-compartment model

Compartmental models are reduced mathematical forms of physiological processes interacting with each other. Compartmental models are represented by well mixed boxes in series and parallel. The relationships between compartments are specified using transfer functions. The general concept of compartmental modeling is to mathematically describe relevant physiological, physicochemical, and biochemical processes from organ to organ or body segment that determine the pharmacokinetic behavior of a compound. The development of a compartmental model follows physiology oriented compartmental kinetics (POCK). It includes specifying the compartments, building the mathematical equations describing the material transfer and estimating the model parameters. Compartments are decided based on the distribution pathways of the substances and the availability of experimental data. Equations are built according to the mass transfer routes and the transportation kinetics. Parameter values are deduced from experimental data sets.

4.3 Mathematical description of a compartment

In general, mass balance equations can be applied for compartments in series. Equation 4.1 shows the mass balance for a compartment with x_i amount of material (as shown in Fig.4.2). Mass transfer rate between compartments is denoted by k, where kij denotes the rate of material being transferred from compartment i to compartment j and D denotes the rate of material injected in to the compartment from exterior. Figure 4.2a shows the general a single

compartment and Fig. 4.2b shows two compartments in series. Equation 4.2 and 4.3 represents the mathematical description of two compartments in series.

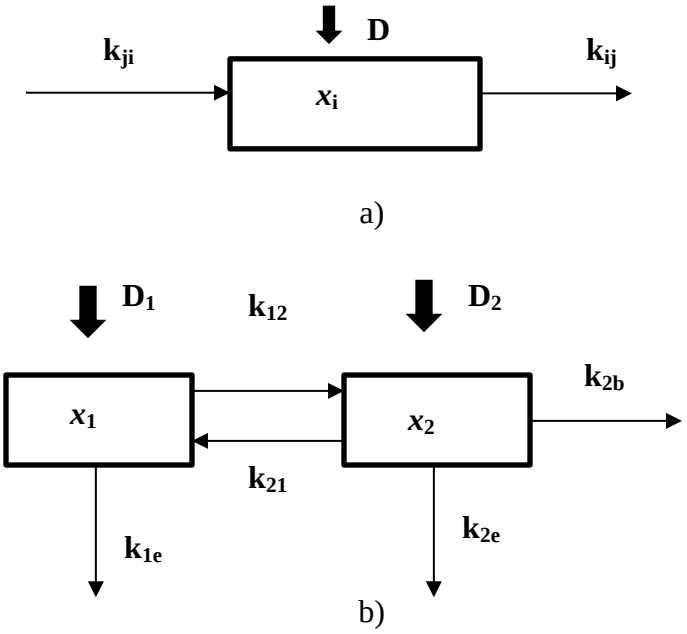

Fig. 4.2. Representation of a) single compartment b) two compartments in series

$$\frac{dx_i}{dt} = \sum k_{ji} \cdot x_j - k_{ij} \cdot x_i + Di \tag{4.1}$$

$$\frac{dx_1}{dt} = \mathbf{k_{21}} x_2 - (\mathbf{k_{12}} + \mathbf{k_{1e}}) x_1 + \mathbf{D_1} \tag{4.2}$$

$$\frac{dx_2}{dt} = \mathbf{k_{12}} x_1 - (\mathbf{k_{21}} + \mathbf{k_{2e}} + \mathbf{k_{2b}}) x_2 + \mathbf{D}_2 \tag{4.3}$$

4.4 Model Structure and Process description

The deposition, retention and translocation of inhaled nanoparticle are modeled using the multi-compartmental model. The schematic representation of the model with transfer coefficients are shown in Fig. 4.3. Each compartment represents probable locations of identifying inhaled ultrafine particles during the clearance process. The compartments are connected based on the transfer routes for particles. The model basically divides the transfer routes to the olfactory region, bronchial region, bronchiolar region, and alveolar region. Epithelium/interstitium was considered as separate compartments in each regions, except in the olfactory, since ultrafine particles can easily cross epithelial cells and reach the interstitium. During the inhalation process particles are mainly deposited in the olfactory, mucus membrane in bronchi and bronchioles and surfactant layer in alveolar region. For the sake of simplification particles are assumed to finally accumulate in the gastrointestinal tract, lymph, interstitial granuloma and secondary organs.

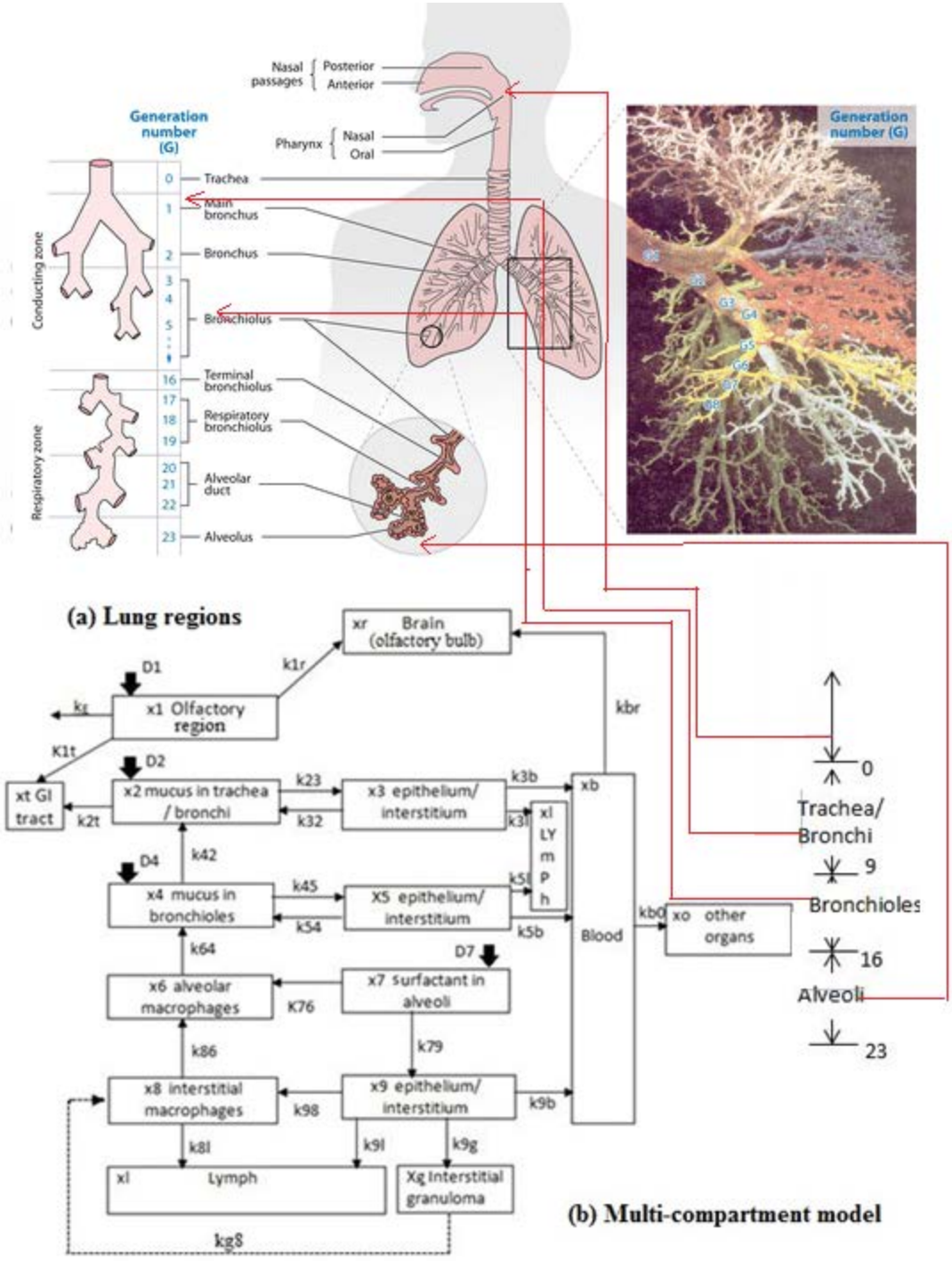

Fig. 4.3. (a) Pictorial representation of the regional differentiation of a lung. (b) Multi-compartment model structure describing the bio kinetics of inhaled nanoparticle

The retention and clearance of particles from the lung depends on the site at which the particles are deposited and the physicochemical characteristics of the particles. The clearance processes from the lung are region specific. Clearance is rapid for particles that deposit in the upper airways compared to that for the particles that deposit in the gas exchange (alveolar) region of the lung. Particles that deposit on the surface of the tracheobronchial region are trapped in the mucus layer that covers the surface of the trachea and bronchi. Ciliated cells waft the mucus (mucociliary escalator) with trapped particles up to the pharynx. The mucociliary escalator does not extend beyond the respiratory bronchioles and is depleted in the terminal bronchioles. Particles that are deposited in the terminal bronchioles and the alveolar region will be phagocytized by macrophages and transport them to the upper bronchioles for clearance through mucociliary escalator. Ultrafine particles can easily cross epithelial cell barrier and reach interstitial space. The free particles from the interstitium can easily reach the lymphatic system or systemic system or else they will be phagocytized by interstitial macrophages and transport them back to the airways or to the lymphatic system. Phagocytosis was not considered as an independent process in the tracheobronchial region because the clearance process is irrespective of the state of particles. Previous studies indicated that ultrafine particles deposited in the olfactory region have been transported from the nasal olfactory mucosa to the olfactory bulb by axonal transport via the olfactory nerve.

Nanoparticles relocate from the lung surface to the pulmonary tissue. Nanoparticles have long term retention kinetics inside the lung compartments. The retained nanoparticles reappeared on the epithelial surface with macrophages. From the broncho alveolar lavage study conducted by them, it is clear that nanoparticles translocate from the bronchial surface

to the epithelium/ interstitium and they are translocated back to the bronchial surface through macrophages. In this model separate epithelial/interstitial compartments with pathways in both direction was created at the tracheobronchial region. Ultrafine particle clearance rate is very slow in human and canine lungs and in many studies (Geiser and Kreyling, 2010) ultrafine particles were found retained in the lung even after years. This phenomenon was modeled using a sequestration compartment, interstitial granuloma. Alveolar macrophages are not a major contributor for ultrafine particle clearance and the phagocytic process by alveolar macrophages is rather sporadic and nonspecific. But still they are involved in the response reaction processes and phagocytic process. So compartments for alveolar and interstitial macrophage were considered in the model.

4.5 Compartments and mathematical description

Table 4.1 shows the compartments and mass of ultrafine particles in each compartment. Each compartment is assumed to be well mixed, no concentration gradient with in compartment, with the nanoparticles. The equations showing the interaction between compartments are explained in detail later.

Table 4.1. Compartments and mass of ultrafine particles in each compartment

Compartment	**Mass of particles inside the compartment**
Olfactory	X_1
Mucus layer in Trachea/Bronchi	X_2
Epithelium/interstitium in trachea/bronchi	X_3
Mucus layer in bronchioles	X_4
Epithelium/interstitium in bronchioles	X_5
Alveolar macrophages	X_6
Surfactant layer in alveoli	X_7
Interstitial macrophages	X_8
Epithelium/interstitium in alveolar region	X_9
GI tract	X_t
Lymph	X_l
Blood	X_b
Interstitial granuloma	X_g
other organs	X_o
Brain	X_b

Olfactory region- As discussed, normal clearance mechanisms for inhaled particles deposited in the nasal compartment of the respiratory tract are toward the gastrointestinal

tract by swallowing and to the environment through expectoration, sneezing and nose blowing. Ultrafine particles from the olfactory region will easily translocate to the central nervous system through the olfactory nerve. Considering all transfer paths as shown in Fig. 4.3, the mass balance equation for this compartment can be written as in Eq. (2), where x_1 denotes the mass of particle remaining in the compartment, k_e shows the particle transfer rate for transfer of particles from olfactory region to the environment, k_{1r} shows the particle transfer rate for transfer of particles to brain, k_{1t} shows the particle transfer rate for transfer of particles to GI tract.

$$\frac{dx_1}{dt} = -\left[k_e \cdot x_1 + k_{1t} \cdot x_1 + k_{1r} \cdot x_1\right] + D1 \tag{4.4}$$

Mucus layer in Trachea/Bronchi - The rate of change of mass within a single compartment at the time *t* is determined by the initially included mass as well as the masses transferred into and out of the compartment. The mass of particle remaining in the compartment is denoted by x_2. From the mucus layer ultrafine particles are transferred to the gastrointestinal tract (GI) and to the corresponding epithelium/interstitium. Also by mucociliary escalation, particles are transferred to this compartment from the bronchioles. As mentioned earlier some of the retained particles will reenter to the mucus compartment from epithelium/interstitium, with or without macrophages. Considering all transfer paths as shown in Fig. 4.3, the mass balance equation for this compartment can be written as in Eq.

(3), where k_{42} is the particle transfer rate for transfer of particles from lower bronchioles(x_4) by mucociliary escalator, k_{32} is the particle transfer rate of resurfacing particles from epithelium/interstitium(x_3); k_{2t} is the particle transfer rate for transfer of particles from mucus in trachea/bronchi to GI tract(x_t); k_{23} is the particle transfer rate for transfer of particles from mucus in trachea/bronchi to epithelium/interstitium and D2 denotes the amount of particles initially deposited by inhalation.

$$\frac{dx_2}{dt} = k_{42}\cdot x_4 + k_{32}\cdot x_3 - k_{2t}\cdot x_2 - k_{23}\cdot x_2 + D2 \tag{4.5}$$

Epithelium/interstitium in trachea/bronchi – Ultrafine particles can easily cross the epithelial barrier to reach interstitium and migrate to lymphatic and systemic system. Also it has been found that the ultrafine particles resurfaced to the epithelial surface. Considering all transfer paths as shown in Fig. 4.3, the mass balance equation for this compartment can be written as in Eq. (4), where x_3 denotes the mass of particle remaining in the compartment, k_{3b} denotes particle transfer rate for transfer of particles to blood and k_{3l} denotes particle transfer rate for transfer of particles to lymphatics.

$$\frac{dx_3}{dt} = k_{23}\cdot x_2 - k_{32}\cdot x_3 - k_{3b}\cdot x_3 - k_{3l}\cdot x_3 \tag{4.6}$$

Mucus layer in bronchioles - From the mucus layer ultrafine particles are transferred to the upper bronchi by mucociliary escalation and to the corresponding epithelium/interstitium. As mentioned earlier some of the retained particles will reenter to the mucus compartment from epithelium/interstitium, with or without macrophages. Also alveolar macrophages will carry some of the particles from the alveolar region to the mucus layer in the upper bronchioles. Considering all transfer paths as shown in Fig.3, the mass balance equation for this compartment can be written as in Eq. (5), where x_4 denotes the mass of particle remaining in the compartment, k_{42} is the particle transfer rate for transfer of particles to upper bronchioles by mucociliary escalator, k_{54} is the particle transfer rate of resurfacing particles from epithelium/interstitium; k_{64} is the particle transfer rate for transfer of particles from alveolar region; k_{45} is the particle transfer rate for transfer of particles from mucus to epithelium/interstitium and D4 denotes the amount of particles initially deposited by inhalation.

$$\frac{dx_4}{dt} = k_{64} \cdot x_6 + k_{54} \cdot x_5 - k_{42} \cdot x_4 - k_{45} \cdot x_4 + D4 \qquad (4.7)$$

Epithelium/interstitium in bronchioles - Considering all transfer paths as shown in Fig.3, the mass balance equation for this compartment can be written as in Eq. (6), where x_5 denotes the mass of particle remaining in the compartment, k_{5b} denotes particle transfer rate

for transfer of particles to blood and k_{5l} denotes particle transfer rate for transfer of particles to lymphatics.

$$\frac{dx_5}{dt} = k_{45} \cdot x_4 - k_{54} \cdot x_5 - k_{5b} \cdot x_5 - k_{5l} \cdot x_5 \tag{4.8}$$

Alveolar macrophages – Some of the ultrafine particles deposited in the alveolar surface are phagocytized by alveolar macrophages, though the process is rather sporadic and nonspecific. Considering all transfer paths as shown in Fig. 4.3, the mass balance equation for this compartment can be written as in Eq. (7), where x_6 denotes the mass of particle remaining in the compartment, k_{64} is the particle transfer rate for transfer of particles to upper bronchioles, k_{76} denotes the rate of phagocytosis from alveolar surface, k_{86} denotes the translocation rate of phagocytized particles from interstitium to the alveolar surface.

$$\frac{dx_6}{dt} = k_{86} \cdot x_8 + k_{76} \cdot x_7 - k_{64} \cdot x_6 \tag{4.9}$$

Surfactant layer in alveoli – The particles are deposited in the surfactant layer of alveoli. From this layer particles either translocate to interstitium or get phagocytized by interstitial macrophages. Considering all transfer paths as shown in Fig. 4.3, the mass balance equation for this compartment can be written as in Eq. (8), where x_7 denotes the mass of particle

remaining in the compartment, k_{76} denotes the rate of phagocytosis from alveolar surface, and k_{79} denotes the translocation rate of particles from the alveolar surface to interstitium.

$$\frac{dx_7}{dt} = -\left[k_{79}\cdot x_7 + k_{76}\cdot x_7\right] + D7 \tag{4.10}$$

Interstitial macrophages - Some of the ultrafine particles from the interstitium are phagocytized by interstitial macrophages and they migrate to the alveolar surface or lymphatics. Considering all transfer paths as shown in Fig. 4.3, the mass balance equation for this compartment can be written as in Eq. (9), where x_8 denotes the mass of particle remaining in the compartment, k_{8l} is the particle transfer rate for transfer of particles to lymphatic system, k_{98} denotes the rate of phagocytosis from interstitial surface, k_{86} denotes the translocation rate of phagocytized particles from interstitium to the alveolar surface, k_{g8} denotes the particle transfer rate of phagocytized particles from interstitial granuloma.

$$\frac{dx_8}{dt} = k_{98}\cdot x_9 - k_{86}\cdot x_8 - k_{8l}\cdot x_8 + k_{g8}\cdot x_g \tag{4.11}$$

Epithelium/interstitium in alveolar region - Some of the ultrafine particles from the interstitium is phagocytized by interstitial macrophages, while some will be sequestered in interstitial granuloma and remaining will translocate to the lymphatic and systemic system.

Considering all transfer paths as shown in Fig. 4.3, the mass balance equation for this compartment can be written as in Eq. (10), where x_9 denotes the mass of particle remaining in the compartment, k_{9l} and k_{9b} denote the particle transfer rates for transfer of particles to lymphatic system and systemic system, k_{98} denotes the rate of phagocytosis from interstitial surface, k_{9g} denotes the translocation rate to the interstitial granuloma.

$$\frac{dx_9}{dt} = k_{79}\cdot x_7 - k_{98}\cdot x_9 - k_{9l}\cdot x_9 - k_{9g}\cdot x_9 - k_{9b}\cdot x_9 \tag{4.12}$$

Considering all transfer paths as shown in Fig. 4.3, the mass balance equation for remaining compartments GI tract, Lymph, Blood, Interstitial granuloma, other organs and Brain are given in Eq. (11), Eq. (12), Eq. (13), Eq. (14), Eq. (15), Eq. (16) respectively where k_{bo} denotes the particle transfer rate for transfer of particle from blood to other organs and k_{br} denotes the particle transfer rate for transfer of particle from blood to brain.

$$\frac{dx_t}{dt} = k_{1t}\cdot x_1 + k_{2t}\cdot x_2 \tag{4.13}$$

$$\frac{dx_l}{dt} = k_{3l}\cdot x_3 + k_{5l}\cdot x_5 + k_{8l}\cdot x_8 + k_{9l}\cdot x_9 \tag{4.14}$$

$$\frac{dx_b}{dt} = k_{3b}\cdot x_3 + k_{5b}\cdot x_5 + k_{9b}\cdot x_9 - k_{bo}\cdot x_b - k_{br}\cdot x_b \tag{4.15}$$

$$\frac{dx_g}{dt} = k_{9g} \cdot x_9 - k_{g8} \cdot x_g \quad (4.16)$$

$$\frac{dx_o}{dt} = k_{bo} \cdot x_b \quad (4.17)$$

$$\frac{dx_r}{dt} = k_{br} \cdot x_b + k_{1r} \cdot x_1 \quad (4.18)$$

Instead of using sequestration compartments to represent the slow clearance from the tracheobronchial tree as in ICRP (1994), an improved way of modeling, considering the physiological mechanisms (the translocation of ultrafine particles to epithelium/interstitium and their resurfacing), was used.

4.6 Assumptions made for multi-compartmental modeling

- Nanoparticles are insoluble
- Physico chemical properties of nanoparticles will not affect the biokinetics.
- No agglomeration of nanoparticles.
- No overload effects in lung due to nanoparticles as compared to micro particles.
- The compartments of the multi-compartmental model are well mixed.

4.7 Conclusion

A multi-compartmental model has been developed to predict the bio-kinetics of inhaled ultrafine particles. In this model the particles were assumed to accumulate in well-mixed

compartments, even though the physiological processes may be different. The model parameters and transfer rates can be estimated from existing particle retention and translocation data sets. The deposition of particles depends on their size. This model can also be used to define pathological situations like COPD, by switching off some of the compartments.

CHAPTER 5
PARAMETER ESTIMATION AND VALIDATION OF RAT LUNG MODEL

5.1 Introduction

Model parameterization refers to establishing plausible parameter values necessary for solving the model equations. Most of the initial transfer rate coefficients were obtained from the open literature and the rest was assumed to produce physiologically reasonable responses. The transfer rate coefficients of the multi-compartmental model were optimized in light of experimental results. Optimization was done with a minimization algorithm using MATLAB. Specifically model was calibrated using experimental results from Semmler et al., (2004) and Oberdörster et al., (2004). Optimal parameter estimation for the transfer coefficients were found by minimizing the mean squared error between the experimental results and simulated results. The limits for the parameters were chosen in such a way that the half-life periods for the particle transfer between compartments were always in the biological range. After estimating the parameters, the model was verified by comparing the simulated results with experimental results for a rat lung from Takenaka et al., (2001).

5.2 Experimental data

Semmler et al., (2004) conducted experimental study of lung retention and clearance kinetics of nanoparticle on rats using ^{192}Ir particles. They also measured the amount of nanomaterial transferred to other organs from lungs through blood circulatory system. The amount of nanomaterial in each organ was calculated by measuring the radioactivity of ^{192}Ir particles.

The count median diameter of ^{192}Ir particles was 15 to 20 nm. During the experiment, rats were forced to inhale ultra-fine particles with a concentration of 0.2 mg/m^3 through an endotracheal cannula for 1 to 1.5 hrs. The ventilation process was controlled using a computer to obtain a breathing frequency of 45 per minute. The amount of nanomaterial retained in the lungs was followed for nearly 180 days. The results showed that the main clearance pathway was up the airway tree with a time course similar to that for micron particles. It was also suggested from these studies that nanoparticles that were translocated into the interstitium reappear on the lung surface within macrophages. Fig. 5.1 shows the variation of retention fraction with time in the whole lung, while Fig. 5.2 shows the cumulative excretion data averaged over all rats.

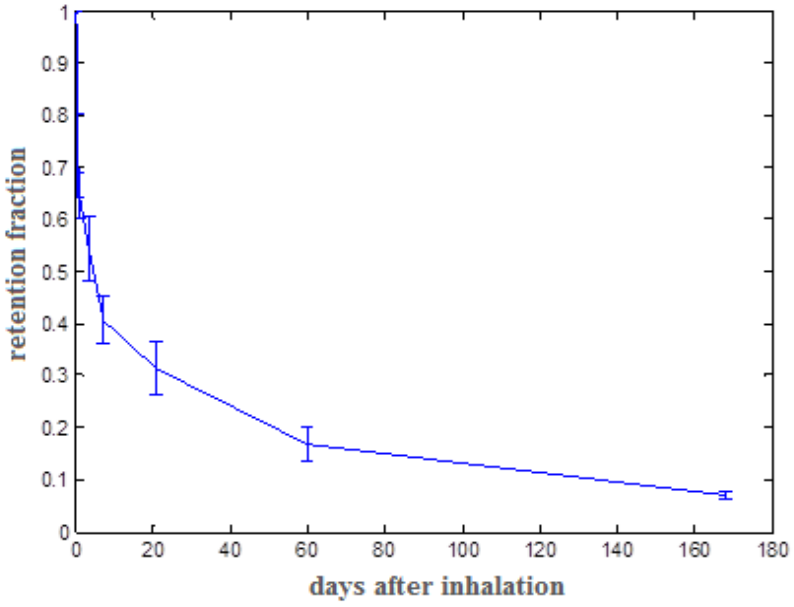

Fig. 5.1. Retention fraction of nanoparticles in lungs (adapted from Semmler et al., 2004)

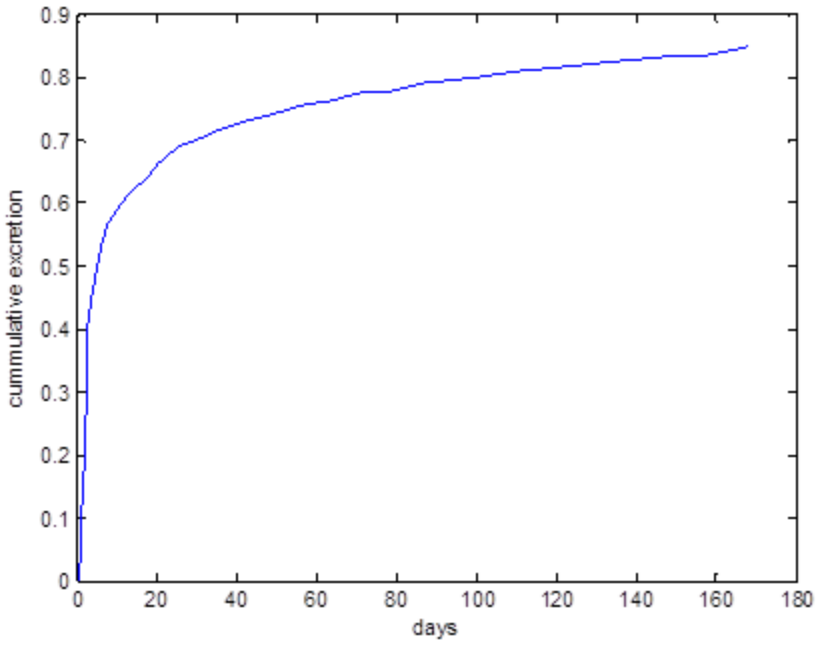

Fig. 5.2. Cumulative excretion fraction of nanoparticles from lungs (adapted from Semmler et al., 2004)

The parameter estimation for the amount of nanomaterial mass transfer from the olfactory region in nose to the brain (olfactory bulb) was done by calibrating the model with the experimental results from Oberdörster et al., (2004). They conducted studies on ultra-fine particle migration to the central nervous system by exposing rats to ultra-fine carbon particles containing ^{13}C in a whole-body chamber for 6 h. The distribution of ^{13}C was followed for 7 days post exposure. There was significant increase in ^{13}C in the olfactory bulb on Day 1 with persistent and continued increase through day 7. Rest of the inhaled particles deposited in the nasal compartment of the respiratory tract was cleared to the gastrointestinal tract by

swallowing and to the environment through expectoration, sneezing and nose blowing. Cumulative particle deposition in the olfactory bulb is shown in Fig. 5.3.

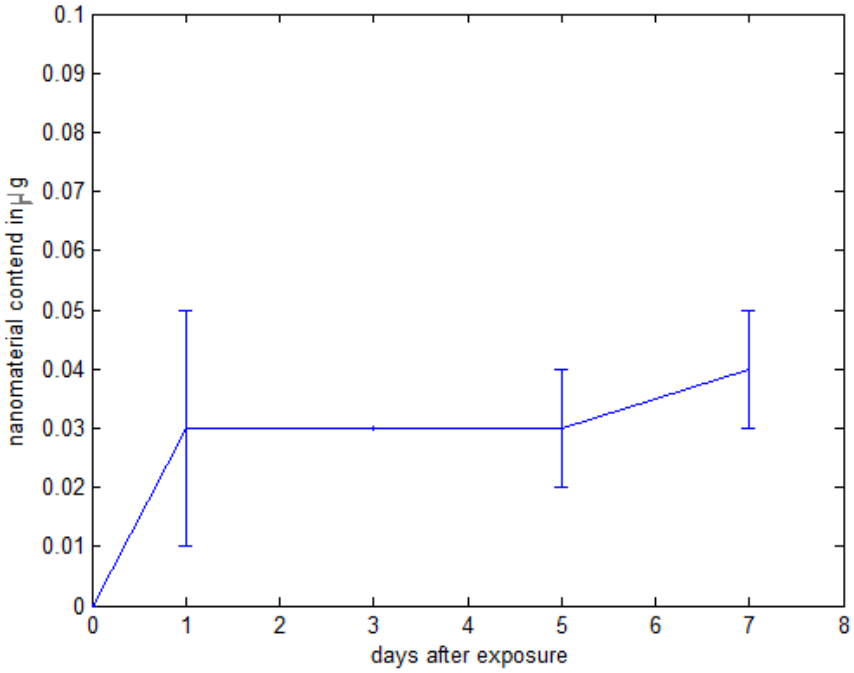

Fig.5. 3. Amount of nanomaterial migrated to the olfactory bulb from olfactory mucosa after an initial deposition from an exposure for 6 hours (adapted from Oberdörster et al., 2004).

5.3 Implementation using MATLAB

The built-in MATLAB variable step ODE-solvers (ode45) were used to simulate the differential equations described in the previous chapter. The parameters were estimated using an optimization algorithm, 'FMINCON', in MATLAB. Most of the initial values for the parameters were obtained from the literature and the rest was assumed to produce physiologically similar responses (see Fig. 5.4).

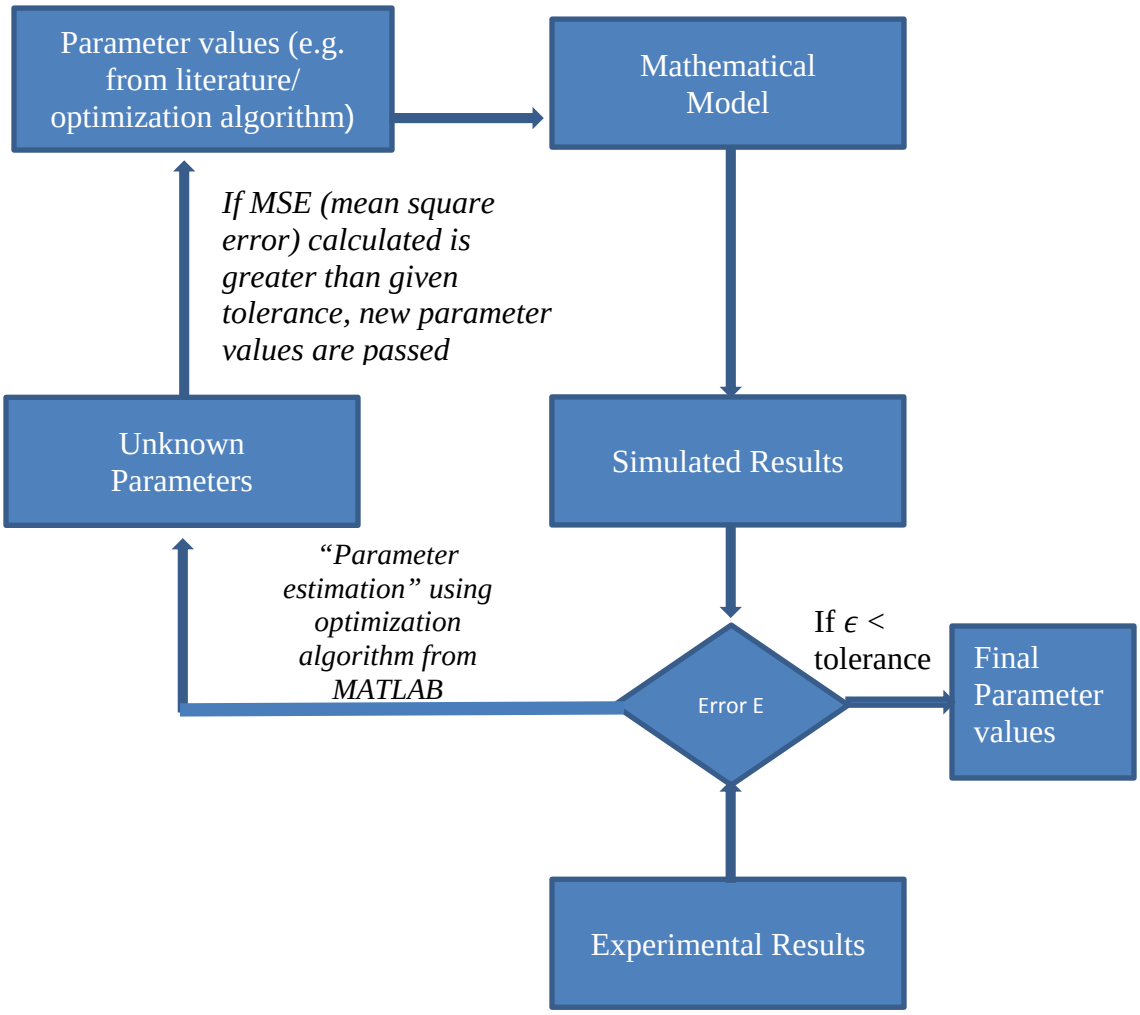

Fig. 5.4. Flow chart representing the algorithm for parameter estimation

The model structure consists of a set of linear differential equations to describe the dynamics of a general input-output system parameterized by a vector K, which represents the unknown constants in the system. The state equation is:

$\dot{\mathbf{x}}(t) = \bar{K} * \bar{x}(t)$ and $\bar{\mathbf{x}}(t_0) = \mathbf{x}_0$

where dot denotes time derivative and '**-** ' denotes vector field and the resulting output equation is:

$\mathbf{x}(t) = g(\mathbf{x}(t, k))$

The model contains unknown parameters K which need to be estimated based on the experimental time-series data. The estimation technique used here is the 'Least Squares method'. The difference between the experimental measurements and the simulated time-discrete model output is the model error E (also referred to as the residuals). Mean square error (MSE) is calculated by finding the sum of squares of error E (method of least square). FMINCON was used to carry out a search over many possible estimates of parameters supplied within limits and choose the parameter vector K which minimizes the MSE.

FMINCON is a function included in MATLAB's Optimization Toolbox which seeks the minimizer of a scalar function of multiple variables, within a region specified by linear constraints and bounds. 'Active set' algorithm was chosen by specifying a parameter in options structure. The function can be called by the flowing syntax.

x_opt = fmincon (fun, *x0*, *A*, *b*, A_{eq}, b_{eq}, *lb*, *ub*)

Where

- *fun* is the "function handle"; that is, the name of an M-file that defines the function
- *x0* is an initial value for the optimizer;
- *A, b* define a linear inequality constraint A * x <= b on the solution.
- A_{eq}, b_{eq} define a linear equality constraint A_{eq} * x = b_{eq} on the solution.
- *lb*, *ub* define bounds on the solution, lb <= x <= ub.

Initial parameter values and each parameter's lower and/or upper bounds were supplied with the calling function as shown above. The termination tolerance for the objective function and the termination tolerance for the parameter estimates were defined in the 'options' using 'OPTIMSET'.

5.4 Parameter estimation for the extra-thoracic model

The extra-thoracic region, including the nasal and oral passages, pharynx, and larynx, is the entrance to the human respiratory tract and the first line of defense against inhaled air pollutants. As explained in the previous chapter, an extra-thoracic model was used to calculate the amount of nanomaterial migrated to the olfactory bulb from nasal mucosa. Fig. 5.5 shows the extra-thoracic model. Nanomaterial transfer from the blood to the brain (parameter k_{br}) was not considered at this point. The amount of nanomaterial in the blood should be calculated from the lung model, which is described later, and once the lung model is calibrated, the transfer route using k_{br} will be added to the nasal model. Experimental results of nanomaterial translocation after an initial deposition from an exposure for 6 hours, given in Fig. 3, was used for calculating the MSE. The amount of nanomaterial deposited in the extra-thoracic region during the 6 hours of exposure was calculated based on the deposition fraction. A program, Multiple-Path Particle Dosimetry (MPPD), was used to determine the deposition fractions in the olfactory, upper airways and alveolar regions. This program can calculate deposition and clearance of aerosols in rats and humans given information about the particle characteristics, exposure conditions, and breathing patterns.

The program is free and can be downloaded from http://www.ara.com/products/mppd.htm.

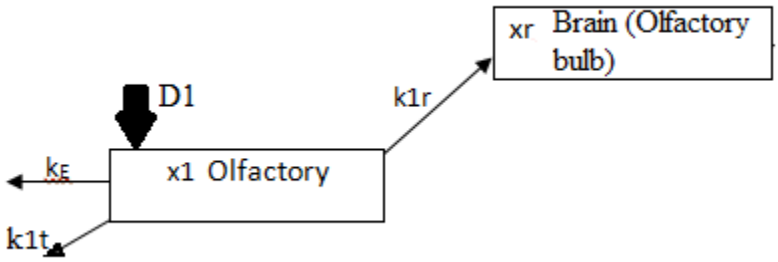

Fig. 5.5. Extra-thoracic model representing translocation of the ultra-fine particle deposited on the olfactory region to brain (olfactory bulb).

The experimental exposure conditions are given in table 5.1. Rat breathing parameters are given in table 5.2. Most of the breathing parameters are generalized values for rat obtained from literature. These conditions were used as input in MPPD to calculate the deposition fraction in the nasal region. A deposition fraction of 0.1 was obtained from MPPD for the nasopharyngeal region. This value was used in the Eq. (5.2), to calculate the amount of particles deposited. Also since the aerosol exposure was only for 1.6 hrs. , the amount of particles deposited was considered as an initial condition and the term D1 from Eqn. (5.1) was neglected.

Table 5.1. Experimental exposure conditions (Oberdörster et al., (2004))

Particle type	^{13}C
Particle diameter	37 nm (CMD) with GSD=1.66
Aerosol concentration	160 μg / m^3 (average of 170 and 150)
Duration of exposure	6 hours
Breathing scenario	Inhalation
Length of follow up	7 days

$$\frac{dx_1}{dt} = -\left[k_e \cdot x_1 + k_{1t} \cdot x_1 + k_{1r} \cdot x_1\right] + D1 \quad (5.1)$$

D1=concentration*ventilation rate*daily exposure in hr.*deposition fraction (5.2)

Ventilation rate=Tidal volume*breathing frequency per min.*60 (in m^3/hr.) (5.3)

Table 5.2. Normal breathing parameters of a rat

Normal breathing frequency	102 / min
Tidal volume	$2.1 * 10^{-6}$ m^3

Table 5.3. Assumed initial parameters for the extra thoracic model

Transfer rates	Initial value (day^{-1})	Half-life (days)	reference
k1r	6.2*10^-3	112	Oberdörster et al., (2005)
ke	0.346	2	
k1t	3.3	0.2	

Initial parameter values were assumed based on the results from Oberdörster et al., (2004). Table 5.3 shows the assumed initial parameters. All the calculations with MPPD results are shown in appendix. Initial parameter values with respective lower and upper bound values for each parameter were supplied with FMINCON's calling function. Another function was used to calculate the MSE between the simulated results produced from the differential equation (Eqn. 5.1), representing the model, and the experimental results (shown in Fig. 5.3). FMINCON was used to reduce the MSE calculated by optimizing the parameter values. Table 5.4 shows the optimized parameter values and Fig. 5.6 shows the amount of nanoparticle translocated to the olfactory bulb, calculated using the model with optimized parameter values. The simulated results show a good fit with the experimental results.

Table 5.4. Optimized parameter values for the extra thoracic model

Transfer rates	Optimized parameter value (day^{-1})
k1r	0.0441
ke	0.2575
k1t	1.3115

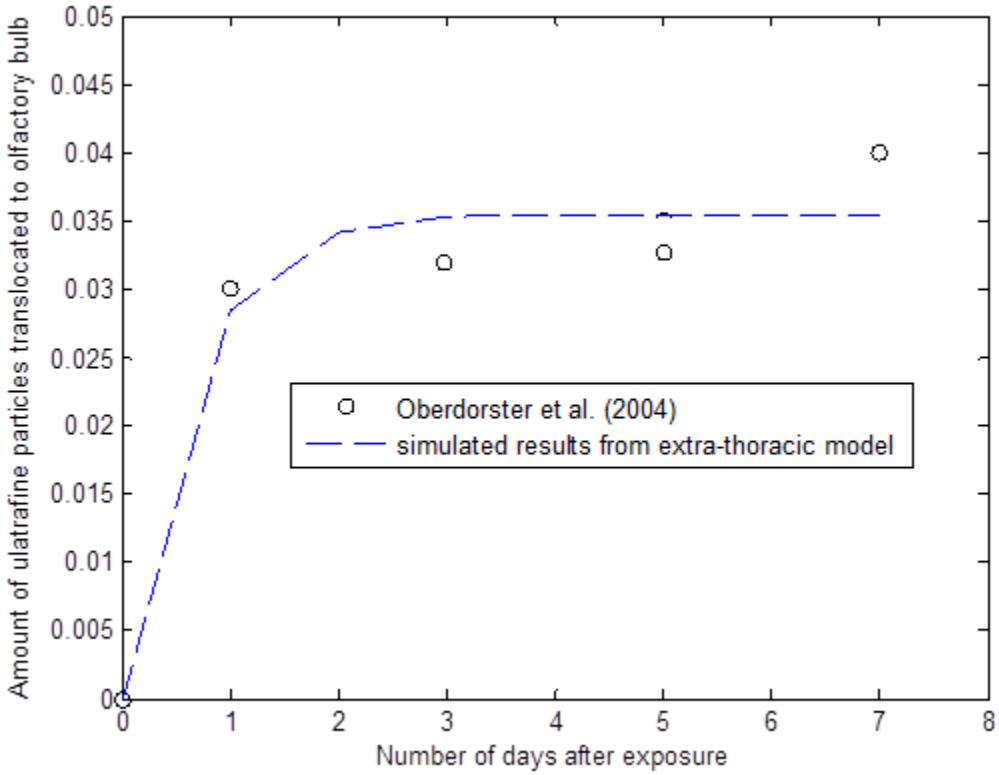

Fig. 5.6 Comparison of amount of nanoparticle translocated to the olfactory bulb, calculated using the model with optimized parameter values, with experimental results.

5.5 Parameter estimation for the rat lung model

As described in the previous chapter, the lung model (without considering the extra thoracic region) was developed with 13 compartments representing each region of lung and connected bio-systems. Initial model parameter values were assigned to each transfer rate coeffiecients based on data available in the literature. The model parameters were optimized by comparing the results of the model with experimental results from Semmler et al., (2004). The amount of nanomaterial deposited in the lung during the exposure was calculated based on the deposition fraction. Multiple-Path Particle Dosimetry (MPPD) was used to determine the deposition fractions, based on the exposure conditions. The experimental exposure conditions are listed in Table 5.5. These conditions were used as input in MPPD to calculate the deposition fraction in the tracheobronchial, bronchiolar and alveolar region. The results from MPPD and the optimization algorithms are given in appendix.

Table 5.5. Experimental exposure conditions (Semmler et al., (2004))

Particle type	Iridium (^{192}Ir)
Particle diameter	15 - 20 nm (CMD)
Aerosol concentration	0.2 mg / m^3 (average of 170 and 150)
Duration of exposure	1.25 hours
Breathing scenario	Endotracheal
Length of follow up	6 months
Breathing frequency	45 / min

5.5.1 Single compartment model

In order to verify the efficacy of a mathematical model in predicting the lung retention, a single compartment model was constructed first. Also it's the simplest model for describing particle retention in the lungs. A basic model of lung with one compartment is shown in Fig. 5.7. Three clearance processes form the lung were considered. They include nanomaterial translocation to GI tract ('kt'), lymphatic system ('kl') and blood circulation system ('kb'). The model can be represented using the differential equation defined in Eqn. (5.4). Also since the aerosol exposure was only for 1.25 hrs. , the amount of particles deposited was considered as an initial condition and the term D in Eqn. (5.4) was neglected. The updated equation is defined in Eqn. (5.5). Table 6 shows the initial parameter values and the lower and upper bounds. The amount of nanomaterial deposited in each part of lung was added together to get the total lung deposition, D. The results from MPPD and the optimization algorithms are given in appendix.

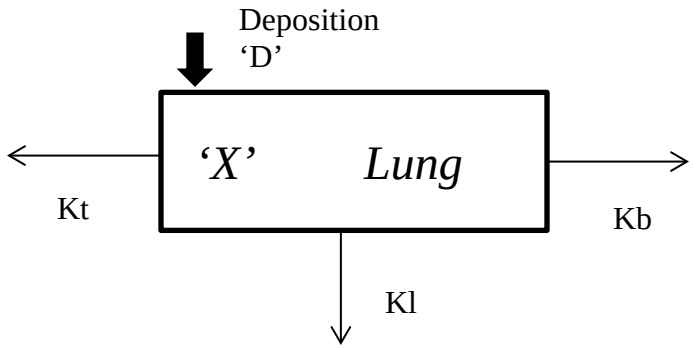

Fig. 5.7. Basic model of lung with one compartment

$$\frac{dx}{dt} = -[k_t + k_l + k_b] \cdot x + D \qquad (5.4)$$

$$\frac{dx}{dt} = -[k_t + k_l + k_b] \cdot x$$

and $x(0) = D$ (5.5)

Table 5.6. Initial parameter values for single compartment model and their lower and upper bounds

Transfer rates	**Initial value (day^{-1})**	**Reference**	**Lower and upper bounds**
kt	2.772	Hoffmann and Asgharian (2003)	0.0693 – 3.465
kl	0.0042	Shinohara et al., (2010)	0.001386 – 0.0231
kb	0.003465		0.001386 – 0.0231

Table 5.7. Optimized parameter values for the single compartment model

Transfer rates	**Optimized value (day^{-1})**
kt	0.115
kl	0.001386
kb	0.001386

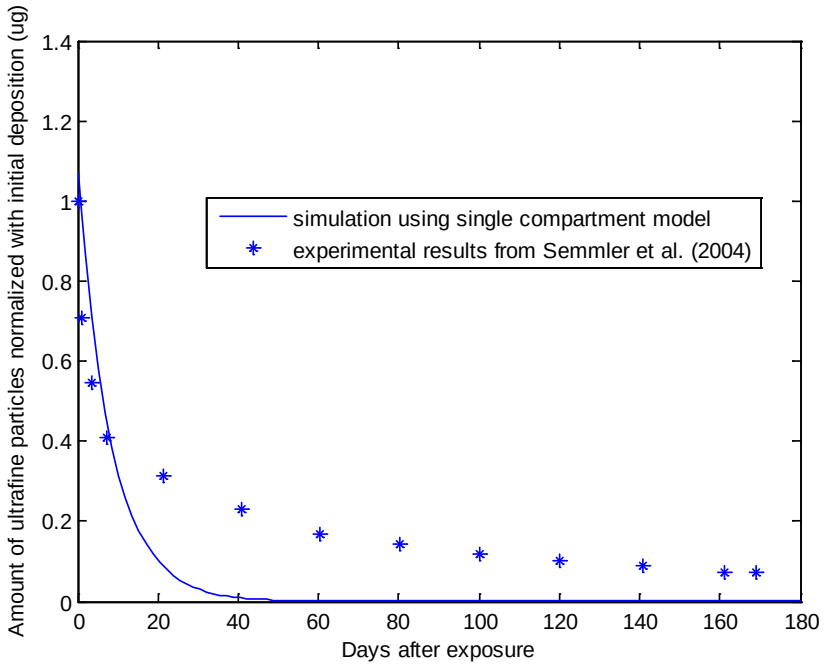

Fig. 5.8. Comparison of results (normalized amount of ultra-fine particle retained) from single compartment model with experimental results

The result from the single compartmental model is plotted in Fig. 5.8. Table 5.7 lists the optimized parameter values for the single compartment model. It appears that a single compartment cannot accurately predict the retention in the lungs. The Mean Square Error (MSE) after optimization was found to be 0.2454, which indicates the mismatch between simulated and experimental results. Even after varying the lower and upper bounds of the parameter values, the model results could not fit well with the experimental results. Clearly a single compartment model is inadequate in predicting nanomaterial retention in lungs.

5.5.2 Two-compartment model

In order to predict the slow clearance of some particles from the lungs, a sequestration compartment (interstitial granuloma) was added to the single compartment model. A sequestration compartment can model the binding of particles to the epithelial cells. These bonded particles will take a long time to clear from the lungs. So, a low transfer rate was used for the clearance of particle from the sequestration compartment. A basic model of the lung with two-compartments is shown in Fig. 5.9. The transfer rates ‘kg’ and ‘kgr’ represent the migration of particles coming in and going out of the interstitial granuloma respectively. The two-compartment model can be represented using the differential equations defined in Eqn. (5.6) and (5.7).

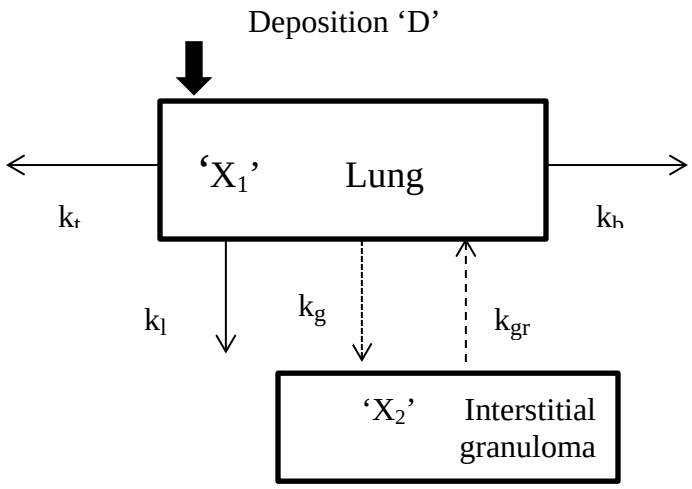

Fig. 5.9. Basic model of lung with two-compartments

$$\frac{dx_1}{dt} = -[k_t + k_b + k_l + k_g]\cdot x1 + k_{gr}\, x_2 \tag{5.6}$$

and x1(0) = D

$$\frac{dx_2}{dt} = k_g \cdot x_1 - k_{gr} \cdot x_2 \tag{5.7}$$

and x2(0) = 0

The parameters were optimized using FMINCON algorithm as explained earlier. The upper and lower bounds for the parameters were chosen based on the physiological clearance time reported in literature. Shinohara et al., (2010) reported a half-life period of 165 days for the particle clearance to the lymphatic system. So a range 20 to 200 days, as half-life period, was used for optimizing the transfer rates from lung to lymphatic system (‘kl’) and blood circulation system (‘kb’). Similarly a range 1 to 10 days, as half-life period, was used for optimizing the transfer rate from lung to gastro intestinal tract. Also a range 30 to 500 days, as half-life period, was used for optimizing the transfer rates between lung and interstitial granuloma. Table 8 lists the initial parameter values for two-compartment model and their lower and upper bounds.

Table 5.8. Initial parameter values for two-compartment model and their lower and upper bounds

Transfer rates	Initial value (day^{-1})	Lower and upper bounds
kt	2.772	0.0693 – 3.465
kl	0.0042	0.001386 – 0.003465
kb	0.003465	0.001386 –0.003465
kg	0.00693	0.001386 – 0.0231
kgr	0.00693	0.001386 – 0.0231

Table 5.9. Optimized parameter values for the two-compartment model

Transfer rates	Optimized value (day^{-1})
kt	0.13213
kl	0.0035
kb	0.00448
kg	0.0231
kgr	0.002774

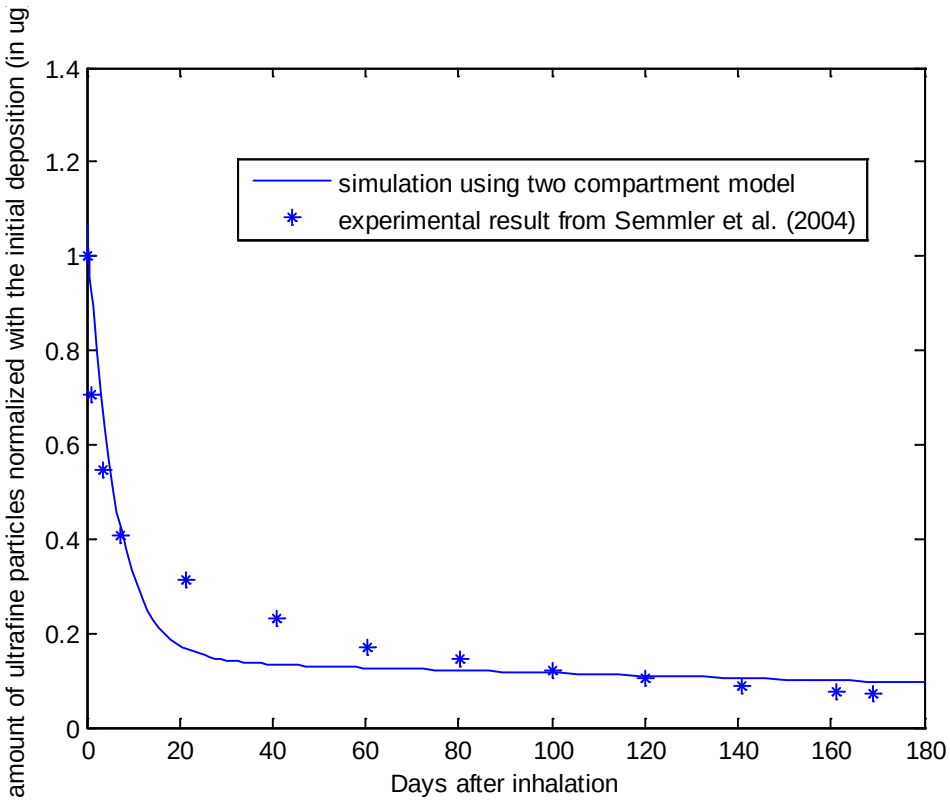

Fig. 5.10. Comparison of two-compartment model results, using optimized parameter values, with experimental results (normalized amount of ultra-fine particle retained in the lung).

The results from the two-compartmental model are shown in Fig. 5.10. Table 5.9 lists the optimized parameter values for the two-compartment model. The Mean Square Error (MSE) after optimization was found to be 0.0715, which shows a good fit between simulated and experimental results. However, as the model depends on the measured airway deposition fraction, the results may not be always accurate. In this case the experiment was based on endotracheal intubation and most of the particle deposited in the pulmonary region of the lung. But if the experiment was based on inhalation the deposition pattern and values would

have been different and the model may not be able to predict the results. Based on this insight, a multi-compartment model with sufficient resolution of particle deposition is proposed. The optimized parameter values from the two-compartment model were used in the multi-compartment model.

5.5.3 Multi-compartment model

The multi-compartment model described in the chapter 4 was used to predict the biokinetics of ultra-fine particle transfer from a rat lung. As mentioned, the model parameters were estimated based on the experimental results from Semmler et al., (2004). Some of the parameters, whose values were either known from the literature or previously estimated using the 'Two-compartment model', were used as initial values. Figure 5.11 depicts the multi-compartment model of a rat lung. Table 5.10 lists the initial parameter values for the multi-compartment model and their lower and upper bounds.

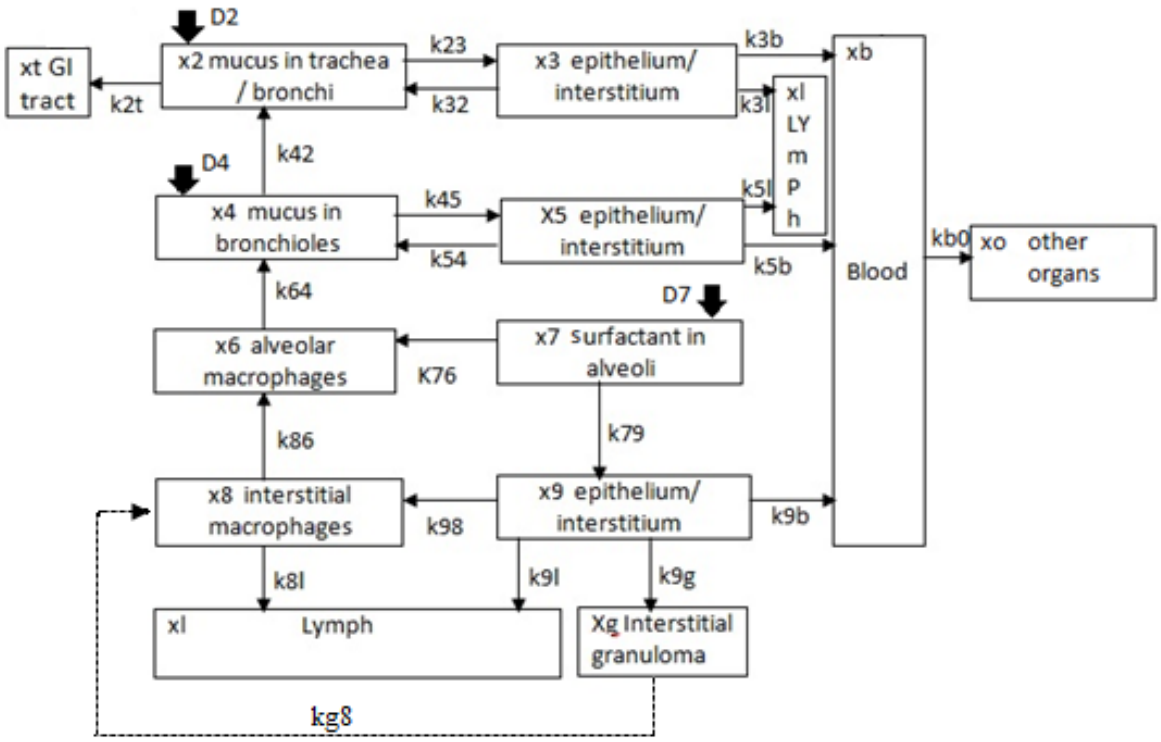

Fig.5.11. Multi-compartment rat lung model

The parameters were optimized using FMINCON algorithm as explained earlier. The upper and lower bounds for the parameters were chosen based on the physiological clearance time reported in literature. The half-life periods for the particle transfer between compartments were always in the biological range. As reported by Semmler et al., (2007), it was expected that most of the nanoparticles translocate from the alveolar surfactant compartment to the epithelium/ interstitium compartment. Also they reported that the amount of nanoparticle phagocytized by alveolar macrophages is very low. So the transfer rate k79 was kept at 0.3465/day and phagocytosis rate k76 was optimized using low transfer coefficient range.

Table 5.10. Initial parameter values for multi-compartment model and with lower and upper bounds.

Transfer rates	Initial Value (day^{-1})	Half-life (day)	Upper and lower bounds	Reference
k2t	2.772	0.25	0.462-4.158	Hoffmann et al., (2003)
k23	0.1386	5	0.03465-0.3465	Semmler et al., (2007)
k32	0.0693	10	0.03465-0.693	
k42	0.231	3	0.1386-1.386	Hoffmann et al., (2003)
k45	0.1386	5	0.03465-0.3465	Semmler et al., (2007)
k54	0.0693	10	0.03465-0.693	
k64	0.231	3	0.0231-1.386	
k76	0.000866	800	0.000815-0.00173	Geiser et al., (2007)
k86	0.1386	5	0.0693- 1.386	
k79	0.3465	2		Semmler et al., (2007)
k98	0.3465	2	0.01386-0.3465	Shinohara et al., (2010)
k3l	0.0035	198	0.000693-0.0034	Two-compartment model
k5l	0.0035	198	0.000693-0.0034	Two-compartment model
k8l	0.0035	198	0.000693-0.0034	Two-compartment model
k9l	0.0035	198	0.000693-0.0034	Two-compartment model
k9g	0.0231	30	0.00231-0.0231	Two-compartment model
kg8	0.002774	250	0.00099-0.002772	Two-compartment model
k3b	0.004482	154	0.000693-0.00448	Two-compartment model
k5b	0.004482	154	0.000693-0.00448	Two-compartment model
k9b	0.004482	154	0.000693-0.00448	Two-compartment model
kbo	30.4*10^-3	22.8		Zhu et al., (2009)

The parameters were optimized using FMINCON algorithm as explained earlier. The MSE was calculated from the error between the simulated results including both retained and excreted nanoparticle fraction and the experimental results shown in Fig. 5.1 and Fig. 5.2. Since the simulated results produced only the excretion through gastro intestinal tract, the excretion through urine was not considered here. A factor 0.5 was multiplied with the MSE from the excretion results. This will ensure that the final optimization results are not affected by the error due to the assumption. The results from the single compartmental model are shown in Fig. 5.12 and Fig. 5.13. Table 5.11 lists the optimized parameter values for the multi-compartment model. The MSE after optimization was found to be 0.01, which shows a good fit between simulated and the experimental results.

Table 5.11. Optimized parameter values for the multi-compartment model.

Transfer rates	**Optimized parameter values (day^{-1})**
k2t	0.71
k23	0.2456
k32	0.693
k42	3.465
k45	0.3465
k54	0.693
k64	1.2141
k76	0.0017
k86	3.465
k98	0.0159
kg8	0.0028
k3b	0.000693
k5b	0.0045
k9b	0.0029
k9g	0.0073
k3l	0.000693
k5l	0.0034
k8l	0.0034
k9l	0.0023

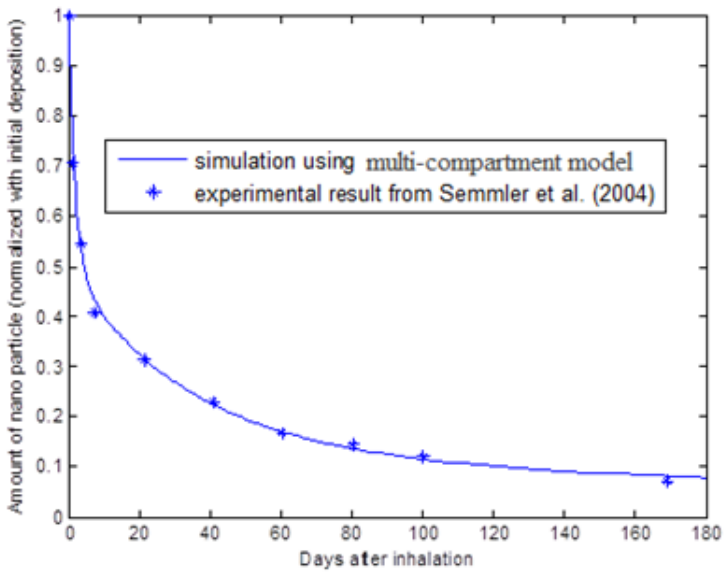

Fig. 5.12. Comparison of multi-compartment model results, using optimized parameters, with experimental results (normalized amount of ultra-fine particle retained in the lung).

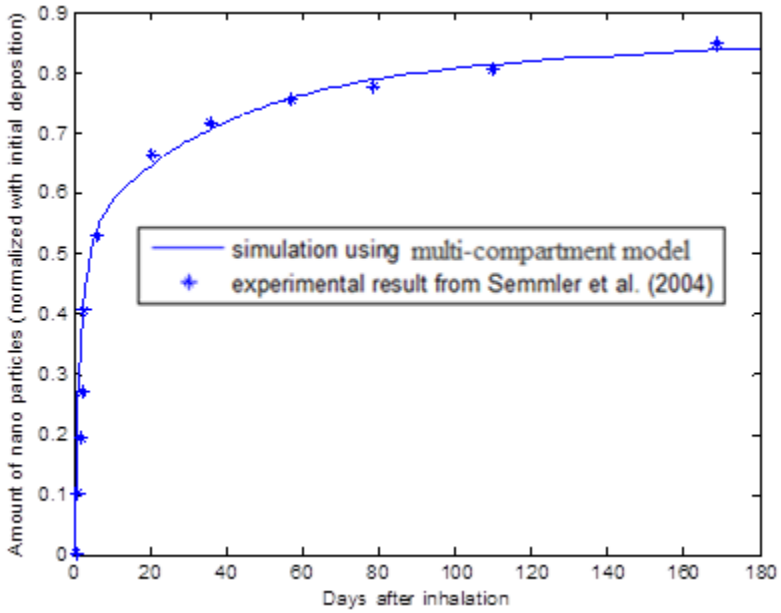

Fig. 5.13. Comparison of multi-compartment model results, using optimized parameters, with experimental results (normalized amount of ultra-fine particle excreted from the lung).

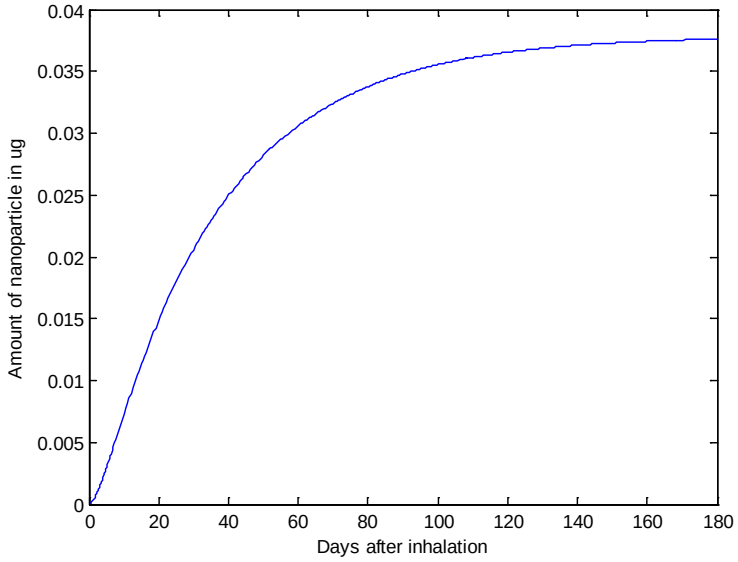

Fig. 5.14. Amount of ultra-fine particles translocated from lung to the lymphatic system (using experimental conditions from Semmler et al., 2004)

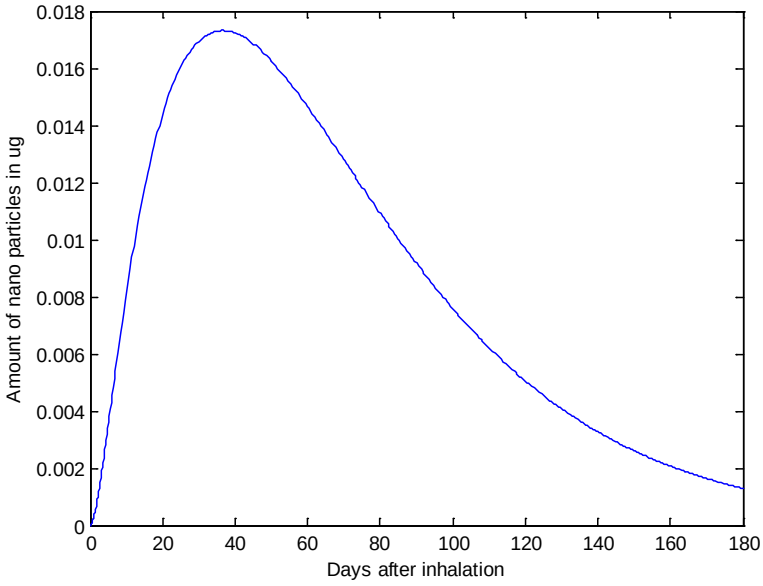

Fig. 5.15. Amount of ultra-fine particles translocated from lung to the blood circulation system (using experimental conditions from Semmler et al., 2004)

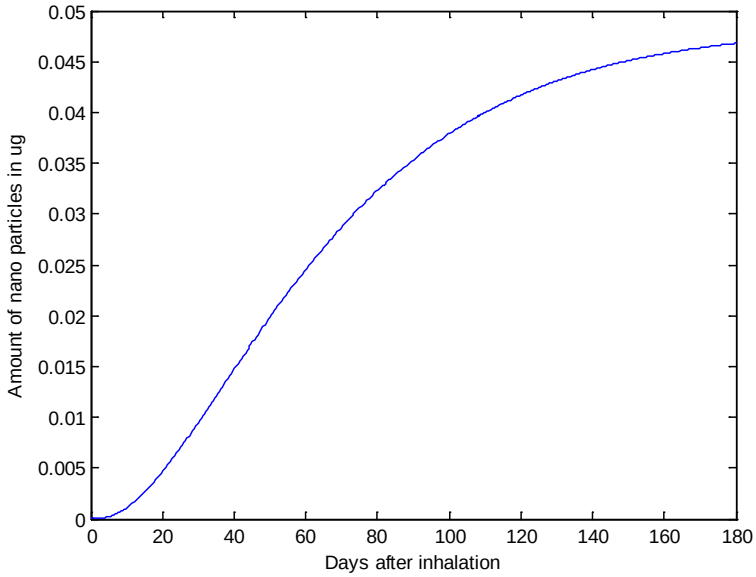

Fig. 5.16. Amount of ultra-fine particles translocated to other organs through blood circulation system (using experimental conditions from Semmler et al., 2004)

The amount of ultra-fine particles translocated from lung to the lymphatic system and blood circulation system are plotted in Fig. 5.14 and Fig. 5.15. Based on the exposure conditions, initial deposition of ultra-fine particles in the rat lung, calculated using MPPD, was 1.06 μg. Semmler et al., (2007) reported an initial deposition of 2 μg during the experiment. Since normalized values were used for parameter estimation, the results are not affected by this mismatch. Also Semmler at al. (2007) reported that only less than 1% of ultra-fine particles translocated to the blood circulation system. But based on the model results, nearly 1.7% of initial deposition of ultra-fine particles rapidly translocated to the blood circulation system within 20 days after inhalation (Fig. 5.14), which is in accordance with the previous studies. Fig. 5.15 shows the amount of ultra-fine particles that can be accumulated in other organs,

considering organs other than lungs where the particles can be deposited through blood circulation, like liver, kidney, spleen, brain, heart, as a closed compartment without clearance. It was found from the model results that, nearly 4.6% of initial deposition accumulated in other organs. Also nearly 3.7% of initial deposition of ultra-fine particles, accumulated in the lymphatic system (Fig. 5.13).

5.6 Nanoparticle distribution from blood circulation system to other organs

A whole body physiology based compartment model was developed to analyze the distribution of nanoparticles from blood circulation system to other organs or tissues like Kidneys, Gut, Spleen, Pancreas, Lung, Heart, Fat, Muscle, skeletal, Bone, Skin. Figure 5.19 shows a multi-compartment model depicting the transport of nanoparticle through blood circulation system to the organs and tissues. The amount of nanoparticle in the blood circulation system can be calculated from the multi-compartment model. Based on the assumption that, any soluble or insoluble substance in the blood will be distributed to organs and tissues according to the blood flow rate ratio to each individual organ or tissue, the amount of nanoparticle transporting to these organs and tissues can be calculated. Table 5.12 lists the blood flow rate to individual organs as a fraction of cardiac output calculated for a rat. It is assumed that the nanoparticles translocated to the pulmonary blood system enter the heart before being pumped into the aorta. The clearance of nanoparticles from organs and tissues are not calculated in this study. Clearance of nanoparticles has been found to depend on the material property of the particle. Further investigation should be done in order to calculate the transfer rates of nanoparticles from tissues and organs to the venous blood

circulation system. Also it should be noted that the macrophages in liver can phagocytize particles from blood circulation system. Connecting the multi-compartment lung model to the multi-compartment organ model, we can predict the total amount of nanoparticles translocated to each organ and tissue over time. Figure 5.20 to Fig. 5.26 shows the distribution of nanoparticles from blood circulation system to Heart, Fat, skeletal Muscle, Bone, Skin, Kidneys and Lung respectively.

Table 5.12. Blood flow rate to individual organs as a fraction of cardiac output calculated for a rat (mean data compiled from the literature)

Tissue	**Blood flow rate (fraction of cardiac output)**
Fat	0.07
Muscle skeletal	0.278
Bone	0.122
Skin	0.058
Kidneys	0.141
Gut	0.131
Spleen	0.02
Pancreas	0.01
Liver	Arterial-0.065; Total-0.226

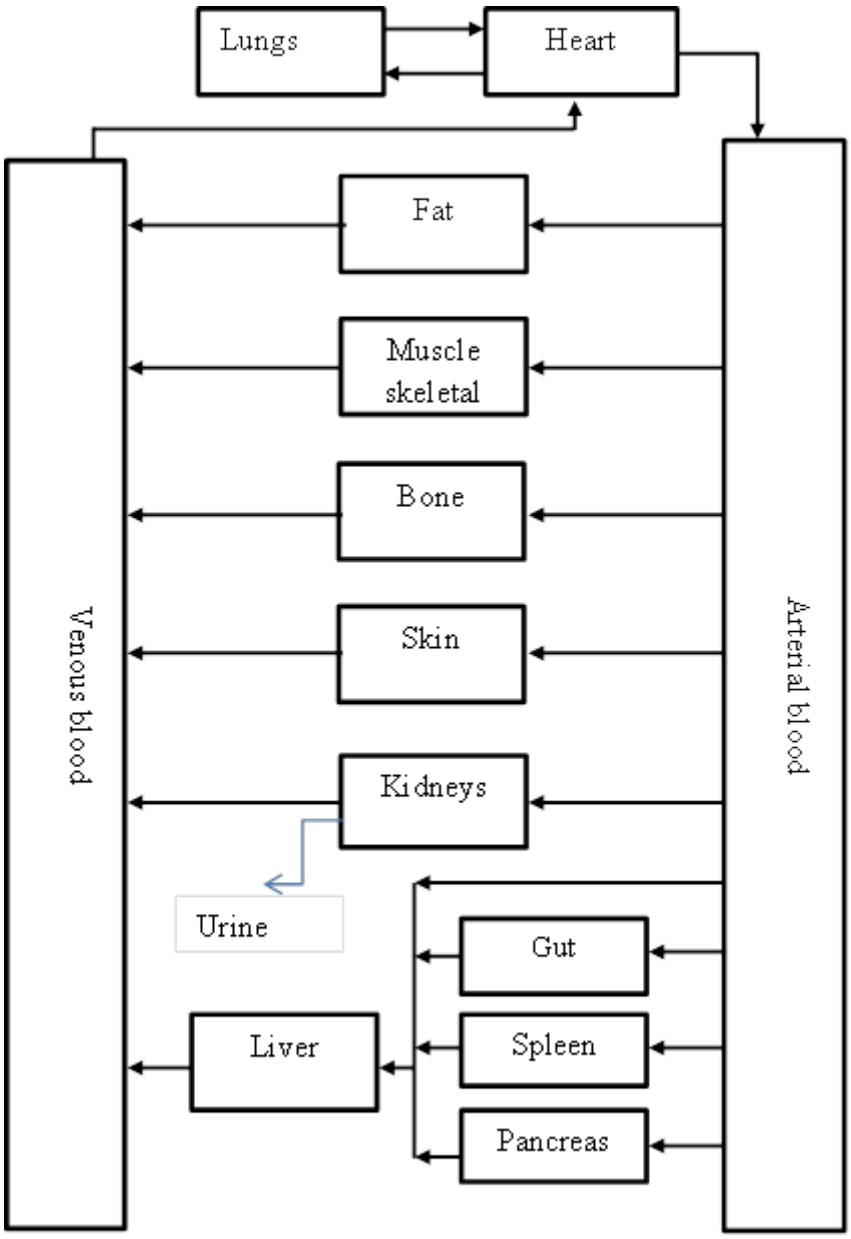

Fig. 5.17. Multi-compartment model depicting the transport of nanoparticle through blood circulation system to the organs and tissues.

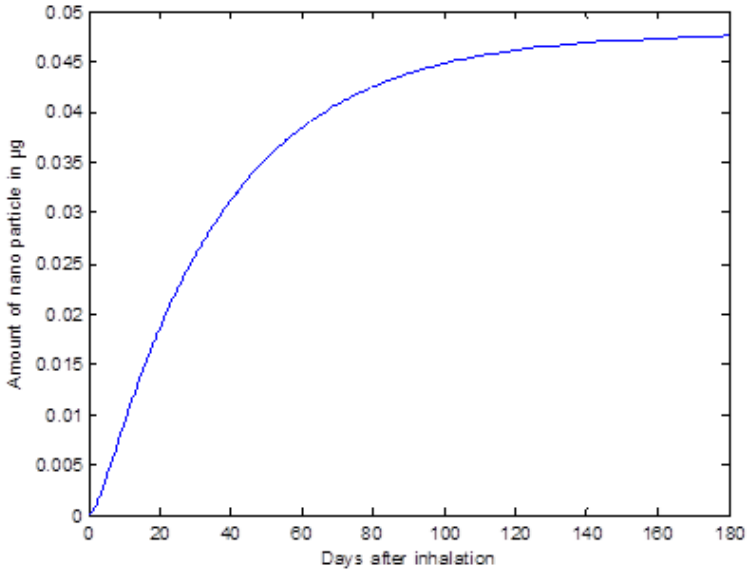

Fig. 5.18. Amount of ultra-fine particles translocated to heart through blood circulation system (using experimental conditions from Semmler et al., 2004)

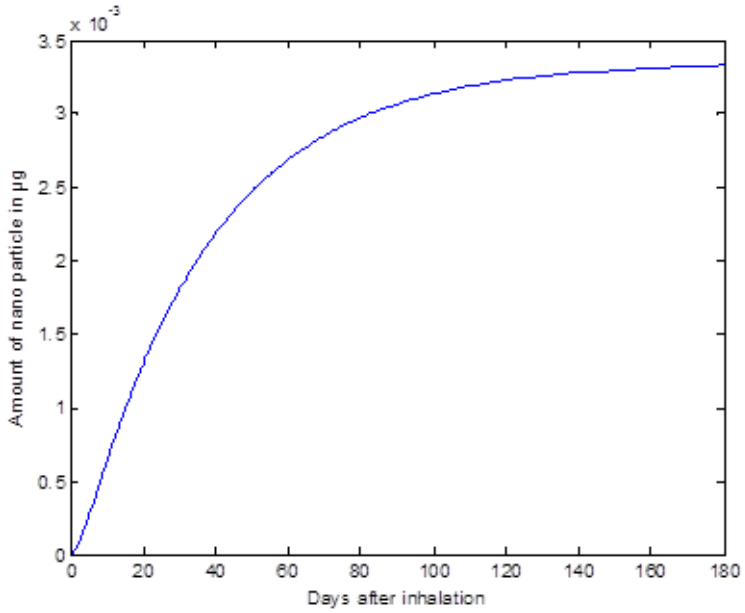

Fig. 5.19. Amount of ultra-fine particles translocated to fat tissue through blood circulation system (using experimental conditions from Semmler et al., 2004)

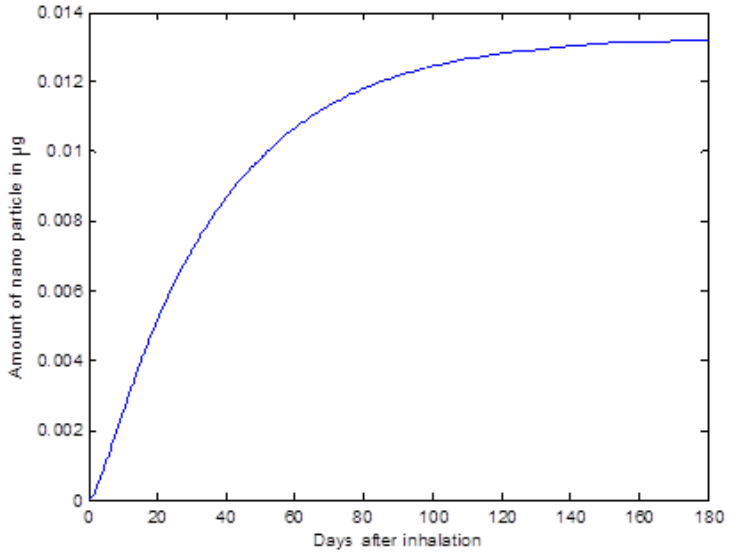

Fig. 5.20. Amount of ultra-fine particles translocated to skeletal muscle tissue through blood circulation system (using experimental conditions from Semmler et al., 2004)

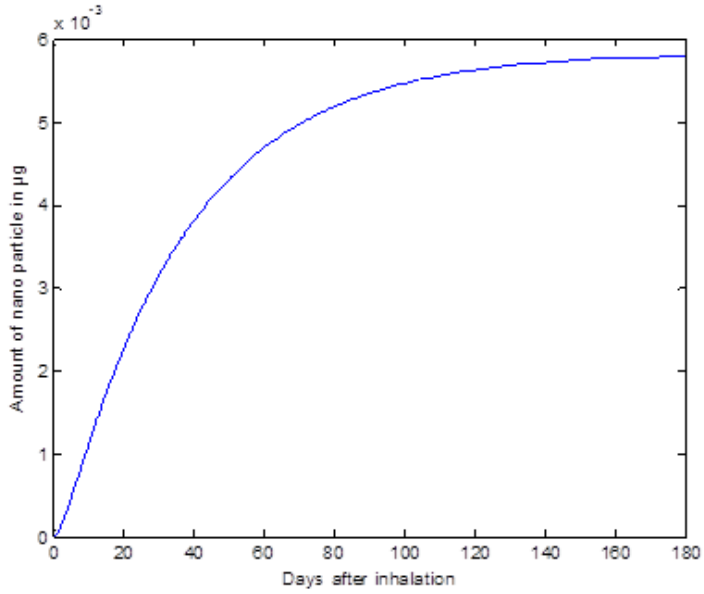

Fig. 5.21. Amount of ultra-fine particles translocated to bone tissue through blood circulation system (using experimental conditions from Semmler et al., 2004)

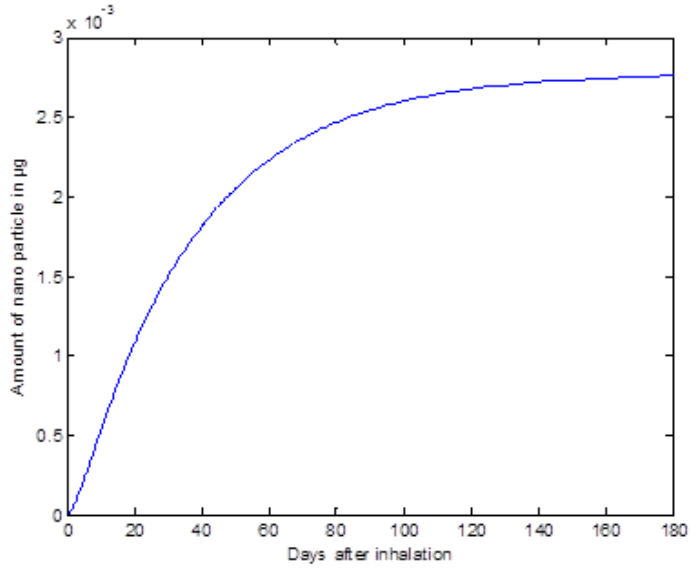

Fig. 5.22. Amount of ultra-fine particles translocated to skin tissue through blood circulation system (using experimental conditions from Semmler et al., 2004)

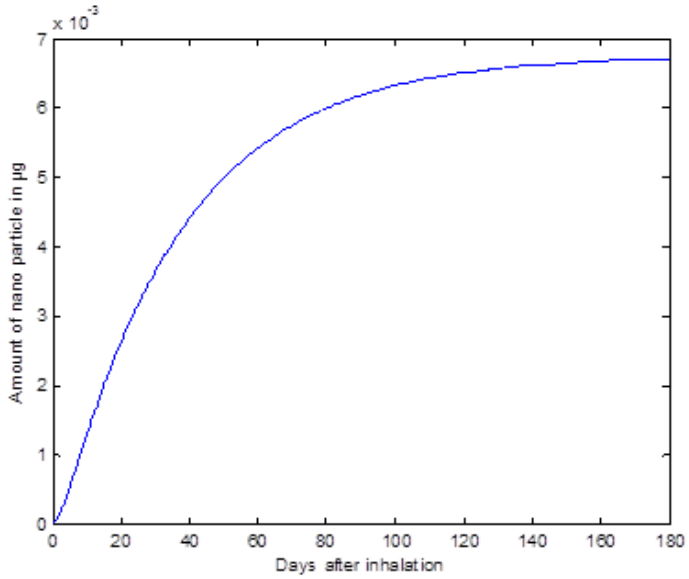

Fig. 5.23. Amount of ultra-fine particles translocated to kidneys through blood circulation system (using experimental conditions from Semmler et al., 2004)

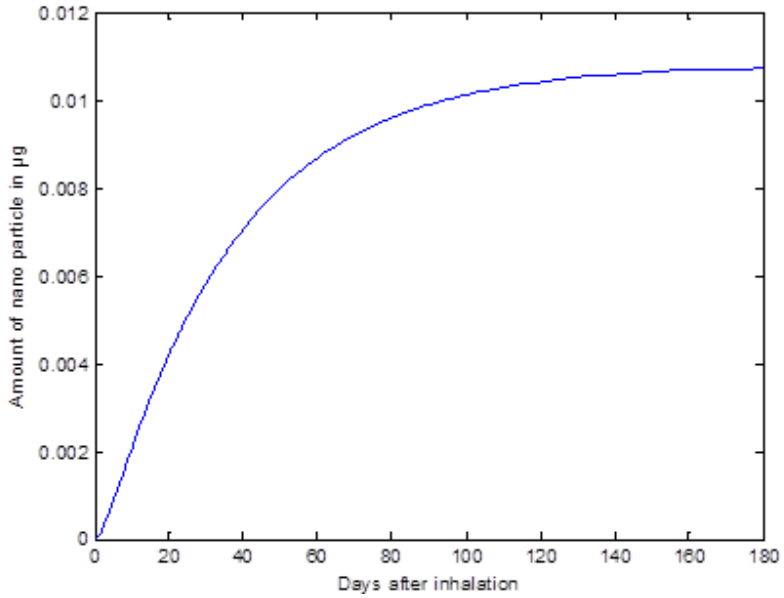

Fig. 5.24. Amount of ultra-fine particles translocated to liver through blood circulation system (using experimental conditions from Semmler et al., 2004)

5.7 Estimation of k_{br} by combining extra-thoracic model and lung model

In order to estimate the parameter kbr (particle transfer from blood to brain), both extra-thoracic and lung model were combined and the model results were calibrated using the experimental results from Oberdörster et al., (2004). The amount of ultra-fine particles translocated to blood circulation system was calculated using the lung model based on the exposure condition in Oberdörster et al., (2004). Since the blood compartment is connected to the brain (olfactory bulb) updated differential equations were added to the existing model equations and the parameter kbr was calibrated using FMINCON function as explained earlier. Since the result used for calibration was only for 7 days, it was assumed that after 7 days the amount of nanoparticles in the olfactory compartment remained almost the same.

Clearance of nanoparticles from olfactory bulb to venous blood was not considered here. Table 5.13 lists the optimized parameter values for the extra thoracic model. Figure 5.27 shows the comparison of amount of nanoparticle translocated to the olfactory bulb, calculated using the model with optimized parameter values with experimental results.

Table 5.13. Optimized parameter values for the extra thoracic model

Transfer rates	**Optimized parameter value (day^{-1})**
kbr	0.0015

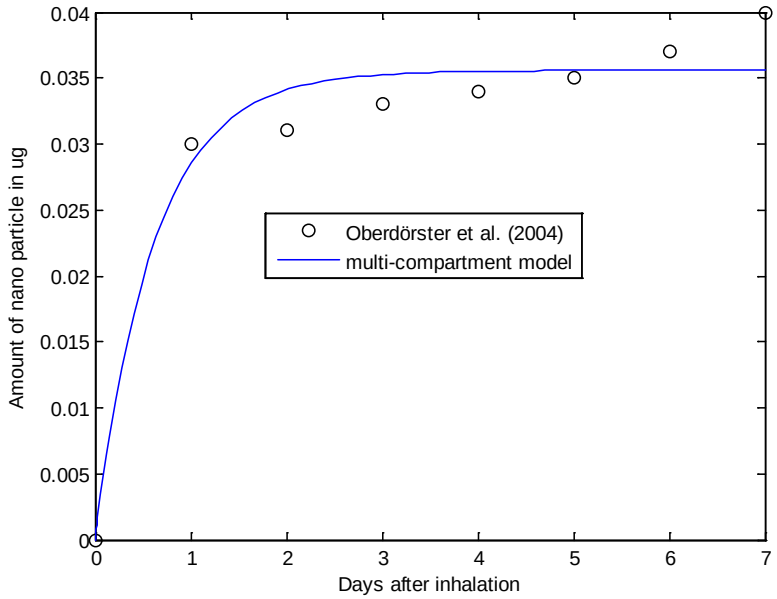

Fig. 5.25. Comparison of amount of nanoparticle translocated to the olfactory bulb, calculated using the model with optimized parameter values with experimental results.

5.8 Validation

The multi-compartment model with optimized transfer rate coefficients was used to predict the biokinetics of ultra-fine particle transfer from rat lung for the experiment done by Takenaka et al., (2006). The lung retention profile produced by the multi-compartment model was compared with the experimental results as shown in Fig. 5.28 and Fig. 5.29 shows the comparison of normalized profiles. The experimental exposure parameters are given in Table 5.14. The initial deposition in the lung and extra-thoracic region was calculated using MPPD. The initial deposition calculated using MPPD was higher than the deposition value reported. The model, as plotted in Fig. 5.28, predicted similar retention profile after day 4, even though the initial depositions were different. The initial lung deposition, calculated using the deposition fraction value obtained from MPPD, was found to be higher than the experimental result. It can be due to experimental error or MPPD modeling error. The MPPD model was found to overestimate the lung deposition in a human scenario (refer chapter 3). So CFPD simulations to calculate lung nanoparticle deposition are recommended. It can be concluded that the model can predict biokinetics of nanoparticle distribution from lung.

Table 5.14. Experimental exposure parameters from Takenaka et al., (2006)

Particle type	Gold
Particle diameter	16 nm (MMD) with GSD=1.5
Aerosol concentration	88 μg / m^3 (average of 170 and 150)
Duration of exposure	6 hours
Breathing scenario	Inhalation

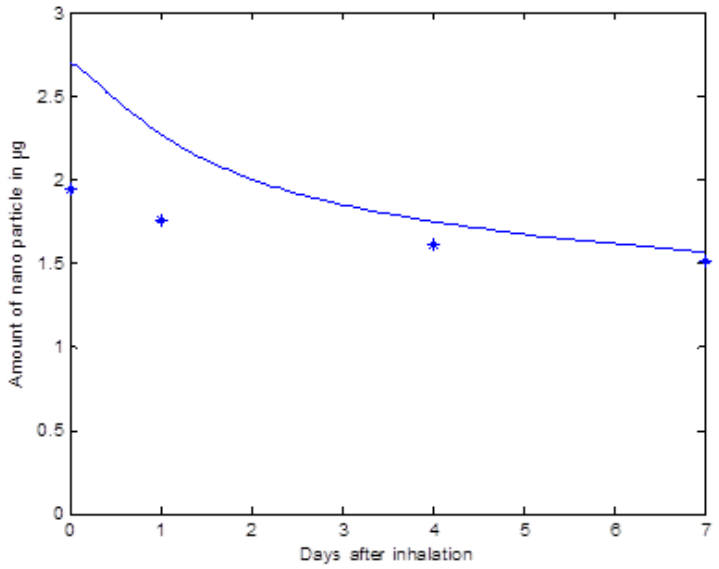

Fig. 5.26. Comparison of rat lung retention predicted by multi-compartment model with the experimental results of Takenaka et al., (2006)

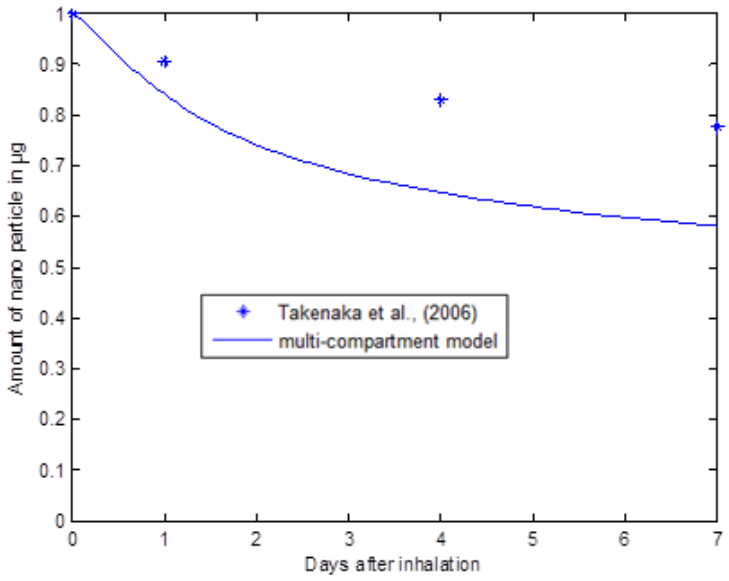

Fig. 5.27. Comparison of normalized retention profiles predicted by multi-compartment model with the experimental results of Takenaka et al., (2006)

From the normalized retention profile predicted by the multi-compartment model (Fig. 5.29), it can be realized that, as per the model, the nanoparticles are cleared faster or in reality the gold nanoparticles are cleared slower than Iridium nanoparticles (the model was calibrated based on Iridium nanoparticle clearance). The surface characteristic and size may affect the nanoparticle clearance. But due to limited clearance data, it is not possible to calculate the transfer rates based on surface characteristics. Introducing a new multiplication factor, from 0 to 10, to account for the surface characteristic may be helpful in predicting nanoparticle clearance. Figure 5.30 shows the comparison of normalized retention profiles predicted by multi-compartment model with the experimental results of Takenaka et al., (2006) after using a multiplication factor of 0.25. The multi-compartment model predictions matched the experimental results well. But finding the multiplication factor for each nanoparticle surface characteristic requires experimental clearance data. Hence creating a database for each particle element is recommended.

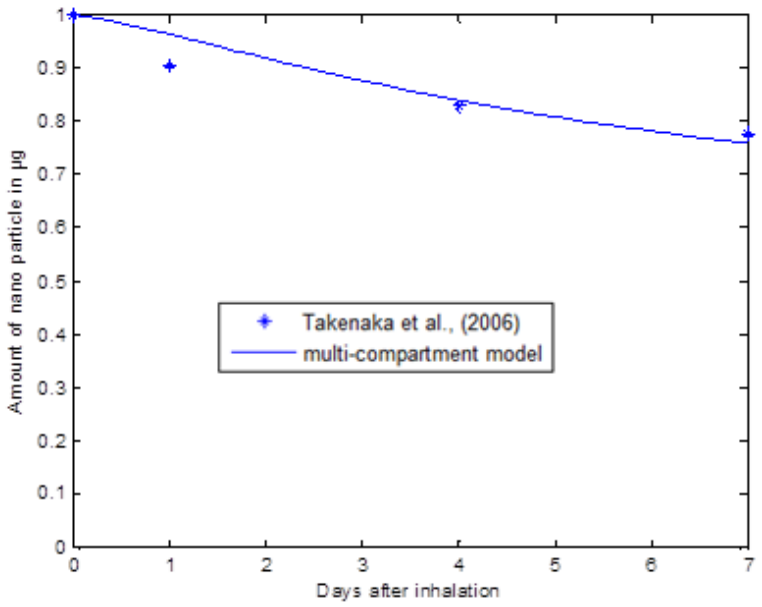

Fig. 5.28. Comparison of normalized retention profiles predicted by multi-compartment model with the experimental results of Takenaka et al., (2006) after using a multiplication factor of 0.25

5.9 Conclusion

The parameters for the proposed multi-compartment model were optimized using experimental results. The predicted results of the multi-compartment model showed good fit with the experimental results. It could be concluded from the estimated transfer rates that the particle clearance from the alveolar region is slow and the sequestered particles will be removed even slower than others. Finally the model was validated with another experiment. However, due to the differences in the initial deposition, and experimental conditions, the initial profiles did not match well. But later on the model predicted results were found to follow the experimental results.

CHAPTER 6
CROSS SPECIES EXTRAPOLATION IN PHARMACOKINETICS

6.1 Introduction

Interspecies correlations of pharmacokinetic parameters obtained from animal tests were used to predict human pharmacokinetics. Most of the drug experiments to check the potential for a chemical agent to produce adverse health effects in humans are often investigated via animal testing. Thus extrapolation of the experimental results from animals to humans has been employed to predict human pharmacokinetics. However lacking detailed information on interspecies differences, it is frequently assumed that experimental results can be extrapolated between species using *body weight scaling*. Allometric scaling, although empirical, is widely used for animal-to-human extrapolation. Allometric scaling is scaling of physiological rates or quantities to relative growth and size (mass or volume) of one animal species relative to another animal species. It is based on the similarity of anatomical, physiological and biochemical variables in mammals.

In general, it is not possible to obtain the retention, clearance and distribution data for hazardous materials directly from observations on humans. There is a pronounced interspecies difference in the deposition, retention, clearance and distribution of inhaled materials. Extrapolation of the results of animal lung clearance experiments to human is not straightforward, as there are often large interspecies differences in the physiological retention and clearance of a material. Interspecies differences in mechanical clearance rates are mainly responsible for differences in the lung retention of similar particles in different animal

species. Previous toxicological studies have shown that if the toxicological response of a particular species can be represented by concentration time profile, then the appropriate interspecies scaling law is (body weight)$^{0.75}$. The underlying premise of such interspecies extrapolations is that similar doses on any species will produce similar effects.

6.2 Body-weight and time scaling

An advantage of the physiologically based model is that by using the appropriate physiological parameters, the same model can be utilized to describe the physiological processes in any species, including mice, rats, and humans. Many of the physiological and metabolic parameters used in pharmacokinetic modeling are directly correlated to the body weight of the particular organism. These physiological parameters generally vary with body weight (BW) according to a power-law which can be expressed as $y = a\ BW^{b}$, where y is a physiological parameter of interest, and a, b are constants. Examples for similar body weight scaling include organ volumes, cardiac output, alveolar ventilation, metabolism and so on. Organ volumes tend to scale across species with the first power of body weight. Total blood volume which scales across species with the 1.02 power of body weight (Stahl et al., 1967) and the mass of the mammalian heart which scales with the 0.98 power of body weight (Prothero et al., 1979). Cardiac output and metabolic rates tend to scale across species with the three-fourths power of body weight (Guyton et al., 1971). Oxygen consumption, food consumption and water consumption rates have been shown to scale across species with the 0.75 power of body weight. A number of other physiological processes, in addition to those listed here, are proportional to $BW^{3/4}$ (West et al., 1997). From these studies it can be

concluded that the 0.75 power of body weight scaling appears to be the most appropriate scaling parameter for cross species extrapolation.

Allometric scaling method has been found to be successful in extrapolating kinetics of pharmacologic agents in relation to BW (e.g., Dedrick et al., 1970; Dedrick et al., 1973; Rhomberg and Lewandowski et al., 2004 and in EPA's Federal Register notice (USEPA, 1992a)). Several studies have demonstrated that various types of toxic material clearance, scale across species with body weight to the 0.75 power. Travis and White et al., (1988) analyzed the dose response relationship of 27 direct acting toxic agents, administered orally in mice, rats, dogs, monkeys, hamsters, and humans. On analyzing the results and the interspecies relationship using regression techniques, they determined that the optimal power of body weight to achieve the best fitting dose response extrapolation is 0.73, i.e., the geometric mean of the cross-species predictions is $BW^{0.73}$.

Several authors have suggested the presence of a species dependent time scale which can be correlated to the body weight (Hill et al., 1950; Dedrick et al., 1973; Boxenbaum et al., 1982; Mordenti et al., 1986; Yates & Kugler et al., 1986). Hill et al., 1950 first suggested that body size served as the regulating mechanism for an internal biological clock, making the rate of all biological events constant across species when compared per unit physiological time. Dedrick et al., 1973, Boxenbaum et al., 1982, 1986, Mordenti et al., 1986 and Lindstedt et al., 1987 verified Hill's conclusions based on experimental results. It has been shown that breath duration, heartbeat duration, longevity, pulse time, breathing rates, and blood flow rates are approximately constant across species when expressed in internal time units. These

time units have been termed physiological time (t') and can be defined in terms of chronological time (t) and body weight *(BW)* as: $t' = t / BW^{0.25}$. Thus, while chronological time is same for all species, physiological time is different for each species (Travis et al., 1990). This means that all species have approximately the same physiological and metabolic rates when measured in the physiological time frame. Comparing the case of men and mice, the body mass and absolute heart mass are both about 2300-fold greater in humans than in mice (scaling to $BW^{1/1}$), cardiac output in humans is only about 300-fold greater than in mice (scaling to $BW^{3/4}$), whereas the heart rate in humans is about 7-fold less than in mice (scaling to $BW^{-1/4}$). The latter relationship, where certain processes between species are related one to another in an inverse manner (i.e., they are decreasing rather than increasing). It follows from the $BW^{0.75}$ allometric scaling that when processes are varying by $BW^{3/4}$, they are normalized against physiological parameter that varies directly as BW^{1}, such that $BW^{3/4} / BW^{1/1} = BW^{-1/4}$. This inverse relationship between the absolute rates of processes and body weight is supported by the concept of physiological time across species (USEPA, 1992a). Thus, processes that are related by $BW^{-1/4}$, such as physiological time, are actually corollaries of the $BW^{3/4}$ scaling. Dedrick et al., (1970) analyzed the cross species relationship in chronological time, called 'pharmacokinetic time', for events like elimination of chemical agents from blood. He plotted normalized plasma concentration on the ordinate by dividing by milligrams per kilogram dose. A clearance adjustment was accomplished by dividing chronological time by $BW^{0.25}$ on the abscissa. The result of this scaling was that dose-adjusted plasma levels when plotted on this new mathematical "space-time" axis were superimposable. The variable of this abscissa, referred to as Pharmacokinetic time (a variable in terms of chronological

time), is shown to be a form of physiological time in which a pharmacokinetic event becomes an independent variable, e.g., disposition half-life in all mammals. He removed the dependency of size on process time by dividing the chronological time by pharmacokinetic scaling factor $BW^{0.25}$. The dose response curve in which normalized concentration (concentration/dose/BW) on the y-axis and normalized time (time/ $BW^{0.25}$) on the x-axis (called 'Dedrick plots') were found to be same across species (see Dedrick plots Fig. 6.1 and Fig. 6.2). Boxenbaum et al., (1982) found that elimination rate constants for drugs in different species are proportional to $BW^{-1/4}$. Observing the methotrexate plasma clearance in mice, rats, dogs, monkeys, and humans, he demonstrated the relationship between pharmacokinetic time and body size, which is $BW^{-0.25}$. This concordance between hypothesis and observations imparts considerable credence to the overall relational postulate of $BW^{-1/4}$ scaling in elimination processes.

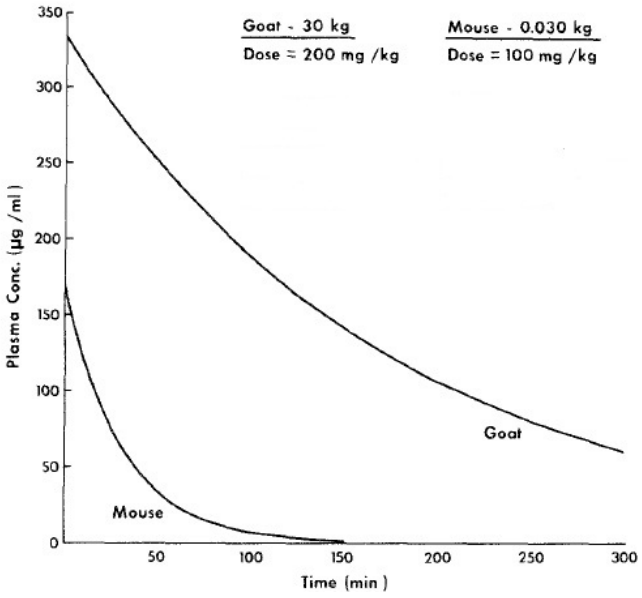

Fig. 6.1. Monoexponential decay curves for a hypothetical single drug in two species (taken from Boxenbaum et al., 1982)

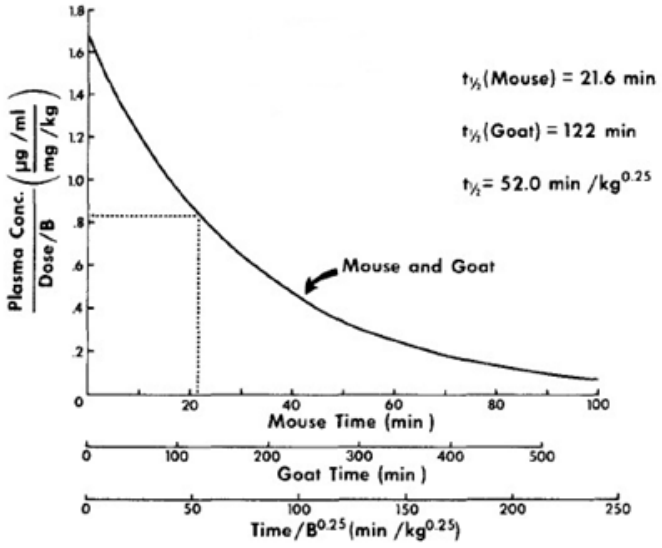

Fig. 6.2. Dedrick plot with normalized concentration on y-axis and normalized time on x-axis (taken from Boxenbaum et al., 1982)

6.3 Scaling to human scenario

A similar approach has been developed to predict particle clearance from human lungs by extrapolating from animal data. The method is based on the assumptions that clearance–time profiles of a chemical agent are similar among species and ‘‘normalized curves’’ from a variety of animal species, including humans, can be superimposed. Normalized curves can be obtained by normalizing the time axis with the pharmacokinetic scaling factor $BW^{-0.25}$ and the y-axis with material deposition at the start of the experiment. The general idea of this method is similar to the Dedrick plot. Using the pharmacokinetic scaling factor $BW^{-0.25}$, clearance time curves in the chronological time scale of an animal are converted to the pharmacokinetic time scale. The pharmacokinetic clearance-time profile is assumed to be similar across species. The clearance-time profile in humans can be predicted from the pharmacokinetic clearance profile by multiplying it with the inverse pharmacokinetic scaling factor $BW^{0.25}$. This method can be applied to any inhaled and deposited material on the assumption that normalized curves from a variety of species can be superimposed.

The applicability of this method has been verified using experimental particle clearance data from the literature. For example Bailey et al., (1989) conducted lung clearance studies on different species like rat, mouse, hamster, dog, baboon, guinea pig and human using ^{57}Co. Lung retention and excretion of ^{57}Co were followed for at least six months after inhalation of monodisperse 0.8 and 1.7 μm diameter (mean geometric diameter) cobalt oxide (Co_3O_4) particles by human volunteers, baboons, dogs, guinea-pigs, rats (three strains) and hamsters, while mice inhaled just the 0.8 μm particles. Lung retention was expressed as a fraction of

the estimated lung content at three days after inhalation, which was taken to be a good estimate of the amount deposited at long-term lung retention sites. Even though the initial lung deposits were different in each species, the normalization using initial lung deposits produced similar retention curves in all species. The initial lung deposit was calculated from the amount of Co deposited on the third day after inhalation so that the material cleared through the rapid phase of mucociliary clearance was excluded. Fig. 6.3 and Fig. 6.4 show the particle retention curves (amount normalized with initial lung deposit) of various species obtained from the experimental study conducted. From the retention curves it can be noticed that, for the BWs increasing the time taken to reach a steady state increases. Clearly, the lung clearance process in man is much slower than any other species. Lung clearance process in a baboon is similar to man even though there is a sudden drop initially which can be due to experimental errors. Since the lung clearance in rat, mouse and hamster reach steady state within 180 days; they can be easily extrapolated to a human scenario.

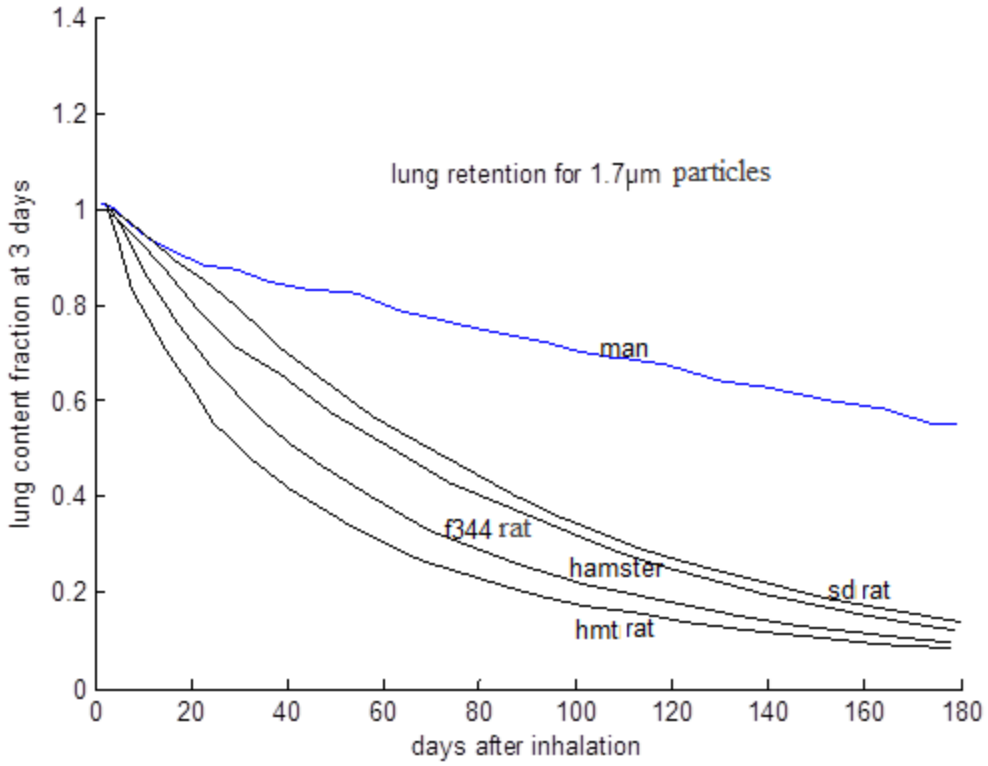

Fig. 6.3. Lung retention of ^{57}Co following inhalation of Co_3O_4 of 1.7μm particles. Y axis represents the normalized amount of particle retained and x axis represents the number of days after inhalation. (Re-plotted from Bailey et al., 1989)

The initial lung deposit for baboon and dog were found to be high when compared to human. So their normalized clearance curve may not be accurately compared with human and hence extrapolation from them was neglected. But for rats, mouse and hamster the initial lung deposit seems to be within a comparable range. It has been noted that if a similar dose concentration is used in a rat and a man, the amount of material deposited in the lungs of a man is about 70 to 80 times the amount of material deposited in the lungs of a rat. A retention

curve for guinea pig was not considered here, because the authors had mentioned uncetainity on the estimated value of initial lung deposit due to the residual pelt contamination.

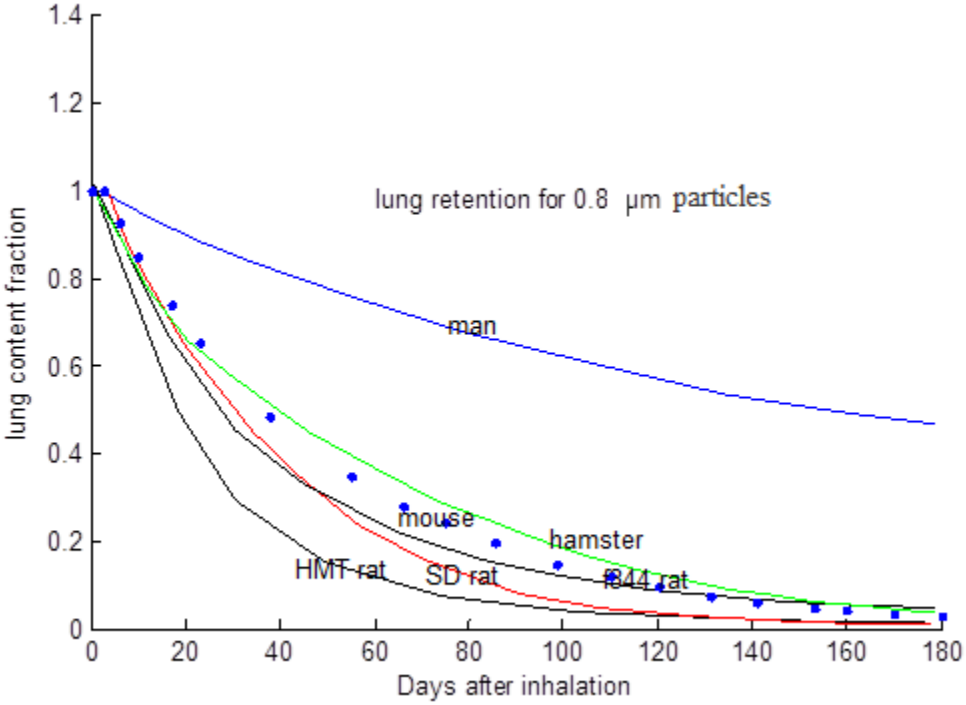

Fig. 6.4. Lung retention of ^{57}Co following inhalation of Co_3O_4 of 0.8μm particles. Y axis represents the normalized amount of particle retained in the lungs and x axis represents the number of days after inhalation. (taken from Bailey et al., 1989)

The average body weights of adult animals and human are shown in Table 1. Dendrick-like normalized retention curves of different species for 1.7μm particles are shown in Fig. 6.5. To confirm the validity of the use of the present approach for prediction, i.e., to confirm that the assumption about the similarity is applicable for humans, the normalized curves for animals were compared with normalized curves for humans. The ordinate which is the lung content,

measured in the succeeding days after inhalation, is normalized by the initial lung deposit. The abscissa, which is the time axis, is normalized using the pharmacokinetic scaling factor $BW^{0.25}$. Although the normalized curves deviate from one another, the trends are similar.

In summary, the assumption of the similarity for normalized concentration–time profiles seems acceptable for lung retention and clearance and it can be assumed that the retention fraction–time profile in humans can be predicted appropriately, using the normalized curve for animals. In addition, to confirm the validity of the use of the present approach for predicting retention fraction–time profile for humans, the normalized curve for humans are also shown in Fig. 6.5. Comparison with those for animals shows good agreement. These results suggest that the assumption of the similar normalized retention fraction–time profile is adequate even for humans, and that the normalized curves for animals can be used to predict the retention fraction–time profile in humans.

Table 6.1. Body Weight for the species considered.

Species	**Body Weight in kg**
Man	73
Rat	SD-0.35, F344-0.3, HMT-0.2
Hamster	0.12
Mouse	0.03

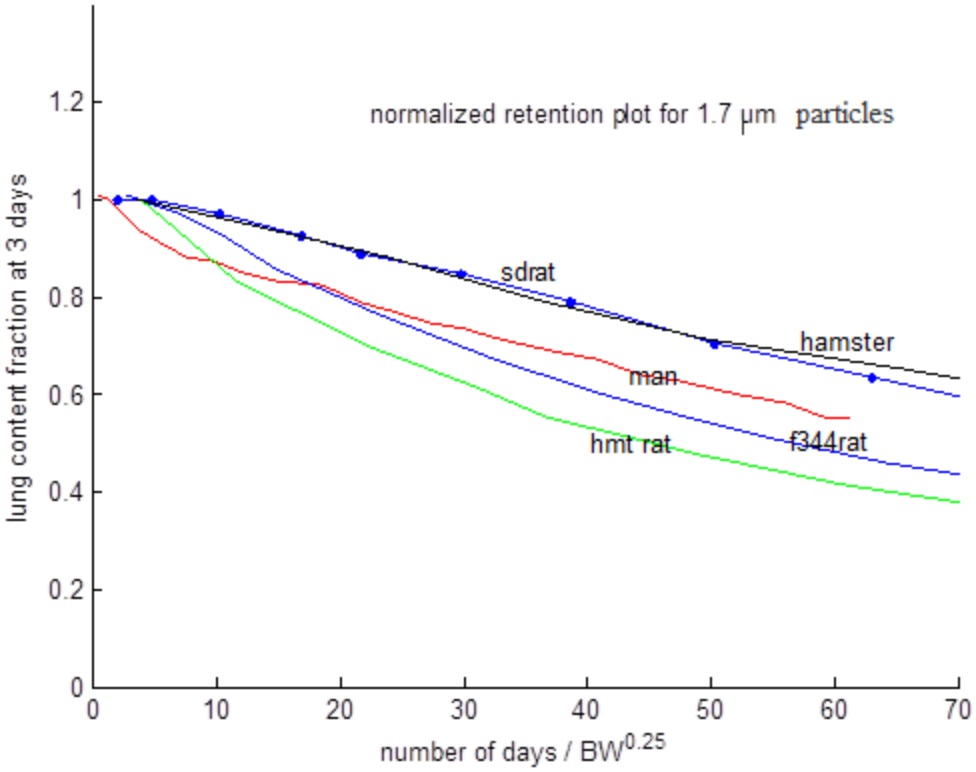

Fig. 6.5. Normalized retention curves for lung retained 1.7μm particles. (Note the time axis normalized using $BW^{0.25}$ – similar to Dedrick plot)

Considering the similarity in the normalized retention fraction–time profile across species, the human retention fraction–time profile is extrapolated from animal retention fraction–time profile. Assuming the normalized retention fraction–time profile are superimposable (neglecting slight deviation across species), the time axis can be equated.

$$\text{Time}_{\text{human}} / BW^{0.25}_{\text{human}} = \text{Time}_{\text{animal}} / BW^{0.25}_{\text{animal}} \qquad (6.a)$$

or

$$\text{Time}_{\text{human}} = (\text{Time}_{\text{animal}} / BW^{0.25}_{\text{animal}}) * BW^{0.25}_{\text{human}} \qquad (6.b)$$

Using Eq. (6.b), the human lung retention fraction–time profile can be extrapolated from animal data. Figure 6.6 shows the human retention fraction–time profile of 1.7μm particles extrapolated from HMT rat, F344 rat, SD rat and Hamster. Human retention fraction–time profile from the experiment is also marked. The extrapolated curves shows good agreement and slight deviation can be attributed to the experimental errors and allometric scaling errors. In order to reduce the error, an average lung retention data of HMT rat, F344 rat, and SD rat was calculated and used to extrapolate to human scenario. Figure 6.7 shows the retention curves of 1.7μm particles extrapolated from average value of HMT-rat, F344-rat, and SD-rat to human. The predicted retention–time profile from rat average data with the observed retention–time data shows good agreement. Figure 6.8 shows the human retention fraction–time profile of 0.8μm particles extrapolated from HMT rat, F344 rat, SD rat and Hamster. The extrapolated curves show good agreement and slight deviation can be attributed to the experimental errors and allometric scaling errors. In order to reduce the error, an average lung retention data of HMT rat, F344 rat, and SD rat was calculated and used to extrapolate to human scenario. Figure 6.9 shows the retention curves of 0.8 μm particles extrapolated from average value of HMT-rat, F344-rat, and SD-rat to human. The extrapolated profile slightly under predicts when compared to the experimental data for 0.8 μm. However, the results for predicting retention–time profiles were still acceptable considering that these are interspecies scaling studies, and could offer useful information for toxicological study.

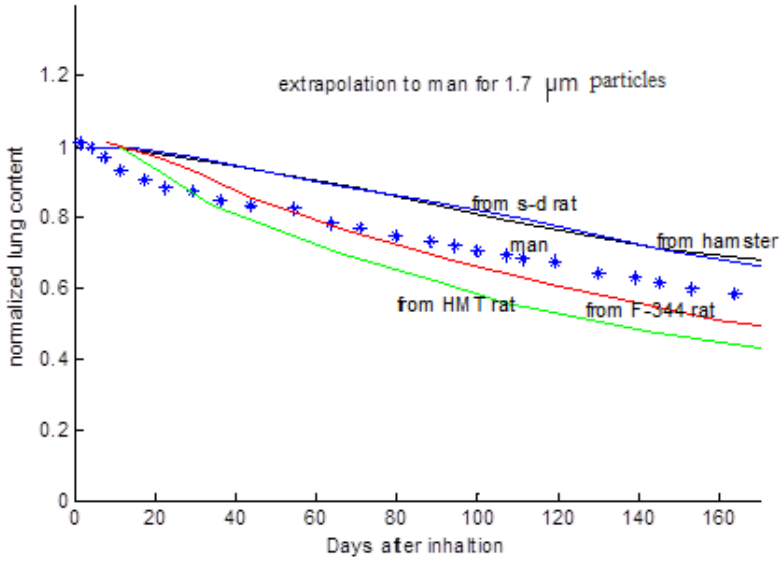

Fig. 6.6. Retention curves of 1.7μm particles extrapolated from HMT rat, F344 rat, SD rat and Hamster to human.

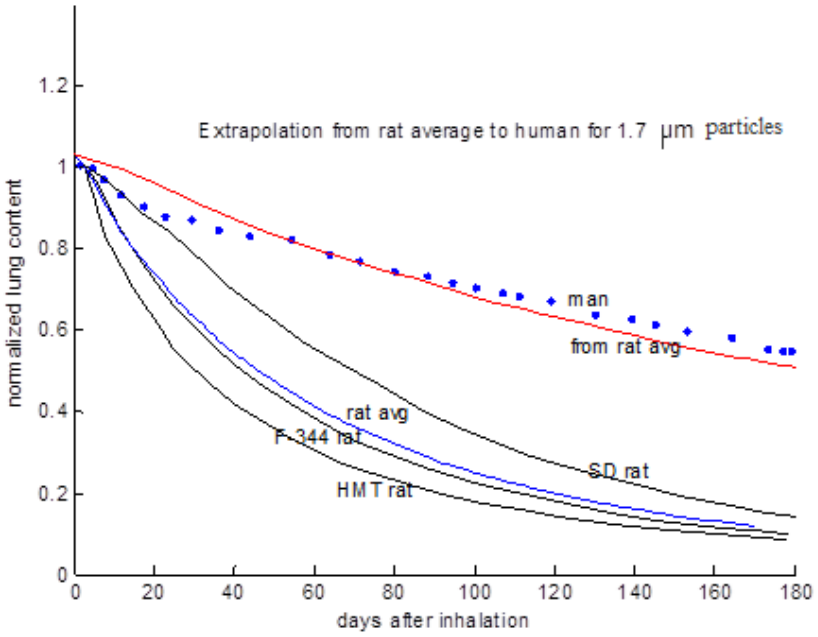

Fig. 6.7. Retention curves of 1.7μm particles extrapolated from average value of HMT rat, F344 rat, and SD rat to human.

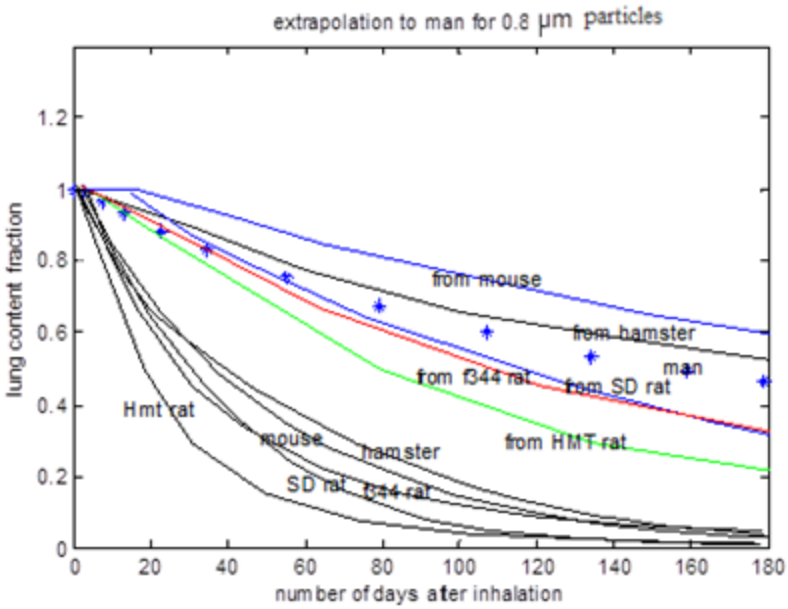

Fig. 6.8. Retention curves of 0.8μm particles extrapolated from HMT rat, F344 rat, SD rat and Hamster to human.

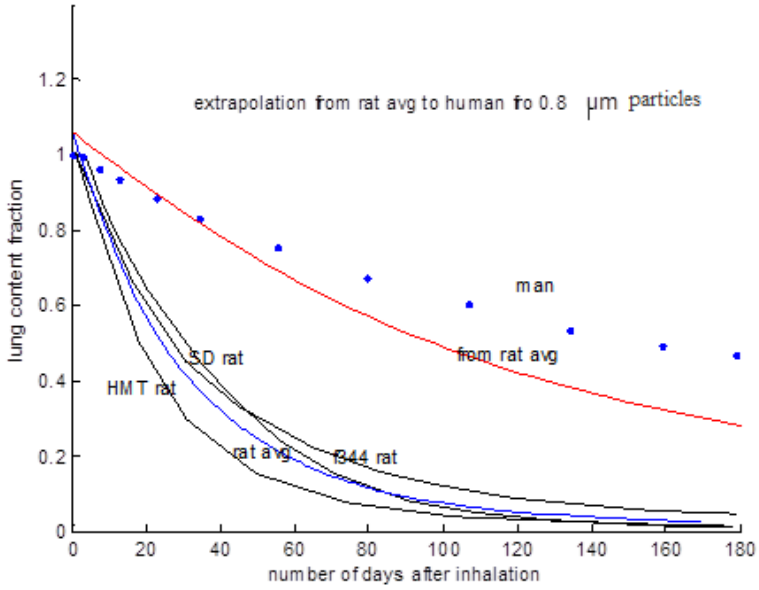

Fig. 6.9. Retention curves of 0.8μm particles extrapolated from average value of HMT rat, F344 rat, and SD rat to human.

The proposed extrapolation method was verified by another experimental result from Kreyling et al., (1998). They conducted lung clearance study on different species like rat, dog, monkey and human using monodisperse Terbium oxide particles. Lung retention and excretion of ^{160}Tb were followed for at least six months after inhalation of monodisperse 1 μm diameter by human volunteers, dogs, monkeys and rats. Lung retention was expressed as a fraction of the estimated lung content at three days after inhalation, which was taken to be a good estimate of the amount deposited in long-term lung retention sites. Even though the initial lung deposits were different in each species, the normalization using initial lung deposit produced similar retention curves in all species. Retention curves for monkey and dog were not considered for extrapolation, because the exposure procedure was different from that of human. Human and rat were exposed to aerosols through inhalation process through mouth and nose, whereas monkey and dog were exposed through endotracheal tubing.

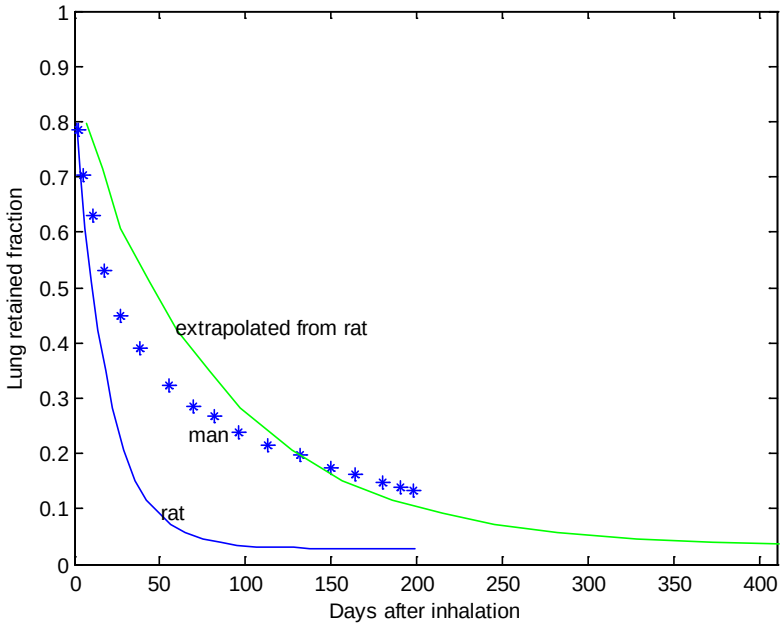

Fig. 6.10. Particle retention curves of rat and man measured by Kreyling et al., (1998) and the human retention curve extrapolated from rat

Figure 6.10 shows the particle retention curves (amount normalized with initial lung deposit) of various species obtained from the experimental study conducted and the human retention curve extrapolated from rat. From the retention curves it can be noticed that, as the BW increases the time taken to reach a steady state increases. Clearly the lung clearance process in man is much slower than any other species. The extrapolated curve shows good agreement and slight deviation can be attributed to the difference in experimental exposure and allometric scaling errors.

6.4 Conclusion

The similarities between extrapolated results based on body-weight and physiological time scaling, with experimental results show that the bio kinetics of deposited nanomaterial in human lungs can be extrapolated from other species. For this analysis it was assumed that the exposure scenario remained the same for human and other species considered. Relying on body weight scaling, $BW^{0.75}$ was used for extrapolating toxicologically equivalent doses. It can be assumed that a toxicologically equivalent dose will produce similar results in all species and even the clearance processes will be similar for all species. Based on this, it can be concluded that, a higher exposure dose in man by a factor of $BW^{0.75}_{human}$ / $BW^{0.75}_{animal}$ will produce similar bio-kinetics in animal and human. If the exposure concentration is higher in man by a factor up to 70 compared to the exposure concentration in a rat, the biokinetics, including retention and clearance, should be similar and the retention curves from rats can be extrapolated. Any overloading effects on rats were not considered in any of the modeling steps, which may be important when dealing with acute exposure concentrations. It was assumed that the exposure concentrations are always below overloading concentrations in both rats and humans.

The results instilled sufficient confidence to extrapolate the result from the rat model to humans and hence apply the multi-compartment model to predict biokinetics in humans. Clearly the deposition of nanomaterial in a human lung is different than in a rat's lung. Therefore new parameters were estimated for the multi-compartment model based, on human lung deposition data.

CHAPTER 7

MULTI-COMPARTMENT MODEL FOR PREDICTING NANOMATERIAL MASS TRANSFER FROM HUMAN LUNG

7.1 Introduction

The normalized rat lung retention profile from Semmler et al., (2004) was extrapolated to human scenario as explained in chapter 6. Based on the extrapolated retention curve the parameters for the multi-compartment model were optimized. The initial deposition in the extra-thoracic region and lung airways were calculated using MPPD model based on multi path human lung deposition model. Since the deposition data was different with respect to a rat lung, the transfer rate coefficients were also different. The transfer rate coefficients for the human lung model are nearly one fourth of that for the rat lung model, implying the clearance process in a human lung is slower by a factor of one fourth than in a rat lung.

7.2 Extrapolation

Tran et al., (2001) extrapolated animal lung model to human by replacing rat based parameters with allometrically scaled parameters and by using human deposition data. He used surface area scaling method for allometric scaling and used lung surface area with a power factor of 0.25 to extrapolate model parameters. Since lung deposition in human is different from rat, replacing the parameters may not always predict the human lung clearance. Instead the multi-compartment model for lung was again optimized to predict the human lung clearance. But the extra-thoracic model parameters were extrapolated using body weight scaling.

The transfer rates coefficients for the human extra-thoracic model was obtained by multiplying the transfer rate coefficients for rat human extra-thoracic model by a factor of 0.256. (Derivation of pharmacokinetic time scale factor 0.256 is explained later). Also it has been reported that, in human only 5 % of the nasal mucosa is olfactory epithelium whereas in rat around 50 % of the nasal mucosa is olfactory epithelium (Oberdörster et al., 2004). To account for this the transfer rate k1r was multiplied by a factor 0.1. It is also believed that trigeminal sensory nerves can carry nanoparticles from the nasal epithelium to olfactory lobe. Also rate of particle clearance to the gastro-intestinal tract from nasal region may not be slower in human as calculated based on extrapolation. The major difficulty in estimating the transfer rate coefficients is that, there is no formal experimental study conducted on humans regarding olfactory transport of nanoparticles to central nervous system.

Same exposure conditions used in experiment by Semmler et al., (2004) were used to calculate the deposition fraction in human lung. As explained in the previous chapter, the deposition fraction was calculated using MPPD. The results from these experiments (only normalized profiles) were extrapolated, using pharmacokinetic time scaling, to human scenario (see Fig. 7.1). As explained in the previous chapter, using MATLAB lung model parameters were optimized using the extrapolated results. The initial values from the rat lung model multiplied by a factor of 0.256 were used to optimize the parameters. Also the upper and lower bounds used for the rat lung model optimization were kept same, but multiplied by a factor of 0.256.

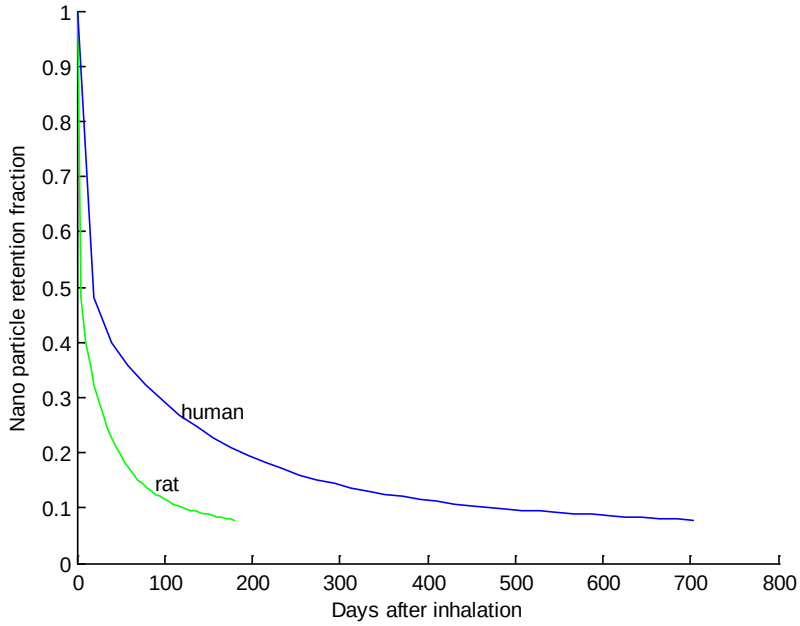

Fig. 7. 1. Human lung retention fraction extrapolated from rat

7.3 Pharmacokinetic time scale factor

The pharmacokinetic time scale for human was calculated using the equation

$$\text{Time}_{human} = (\text{Time}_{animal} / BW^{0.25}_{animal}) * BW^{0.25}_{human} \qquad (7.1)$$

By choosing average weight for rat and human as 0.3 kg and 70 kg respectively, the pharmacokinetic time scale factor can be calculated as

$$BW^{0.25}_{human} / \; BW^{0.25}_{animal} = (70/0.3)^{0.25} = 3.9084 \qquad (7.2)$$

It means that the processes in human body slow down by a factor of 3.9084. So it is expected that the transfer rates would slow down by a factor of 1/ 3.9084 which is equal to 0.256. So the pharmacokinetic time scale factor for extrapolating pharmacokinetic results from rat to human is 0.256.

7.4 Estimated parameters

The estimated parameters for the human multi-compartment model are listed in Table 7.1 and Table 7.2. The initial lung deposition was calculated based on the CFPD deposition fraction results for 17 nm particles (reported in chapter 3, Table 3.12). The deposition fraction and initial deposition are listed in the appendix A2 (table A2.2). The simulation using estimated parameters showed good fit with the experimental results. Similar to the parameter optimization for the multi-compartment rat lung model, the upper bound for the nanoparticle transfer to an interstitial compartment was kept at 4.8 hours. The upper and lower bounds for the transfer rates to the lymphatic system and systemic system were selected in order to obtain similar characteristic profiles as that of a rat lung model. The transfer rates k_{79} and k_{bo} were also multiplied with pharmacokinetic time scale factor 0.256. Since the human lung deposition fractions were different compared to that of a rat lung, the model transfer rates were different from the scaled parameters.

Table 7.1. Estimated parameters for human extra-thoracic model

Transfer rates	Optimized parameter value (day^{-1})
k1r	0.0441*0.256*0.1
ke	0.2575*0.256
k1t	1.3115*0.256
kbr	0.0015*0.256

Table 7.2. Estimated parameters for human lung model

Transfer rates	Optimized parameter values (day^{-1})
k2t	3.465
k23	0.0089
k32	3.465
k42	3.465
k45	0.0089
k54	3.465
k64	3.465
k76	0.0004426
k86	3.465
k98	0.0448
kg8	0.0025
k3b	0.0046
k5b	0.0030
k9b	0.0046
k9g	0.0347
k3l	0.0046
k5l	0.0030
k8l	0.00463
k9l	0.00463

The transfer rate coefficients from the alveolar region are very low, implying slow clearance from the alveolar region. Previous studies using ultrafine particle showed slow clearance from lung periphery which is in good agreement with the model parameter estimation. Even though the mucociliary clearance rate for particles in the upper airways is slow in human

when compared to rat, particle clearance rate from the upper airways to the gastrointestinal tract seems similar in both rat and human.

7.5 Simulation of nanomaterial transfer from human lung

The multi-compartment model was used to simulate the retention and clearance of nanoparticles from human lung. The initial lung deposition was calculated based on the CFPD deposition fraction results for 37 nm particles for an inspiratory phase of 2sec (reported in chapter 3). The deposition fraction and initial deposition are listed in the appendix A2 (table A2.1). The exposure conditions used were similar to experiment conducted by Oberdörster et al., (2004), so that the particle clearance and translocation rates in human and rat lung can be compared. Also the experiment is similar to real life scenario where atmospheric particulate matters are inhaled through nose. Previous reports indicate that atmosphere concentration of particulate matter, with a high concentration of ultrafine particles, ranges between 20 to 200 $\mu g/m^3$ (Seaton et al., 1995). So the simulation results could be compared with the ultrafine particle clearance from a human lung after normal inhalation from ambient air. But here for the simulation, it was assumed that the exposure duration was only 6 hrs.

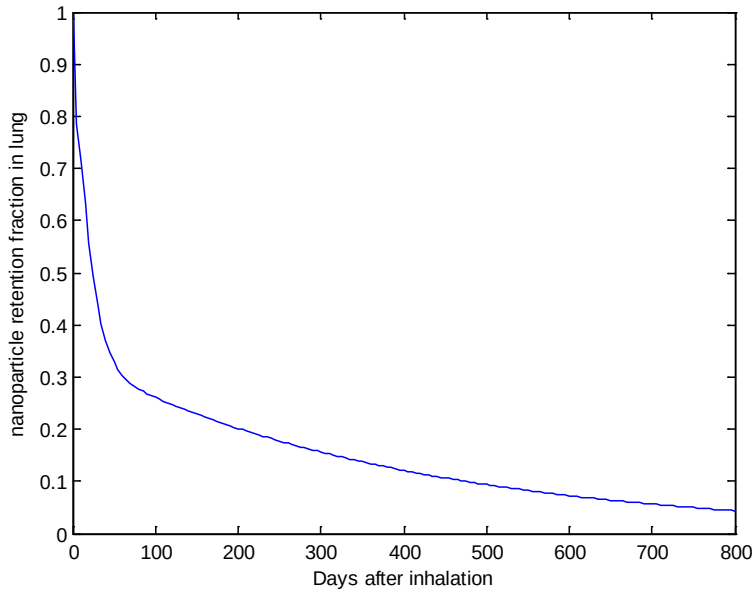

Fig. 7. 2. Nanoparticle retention fraction

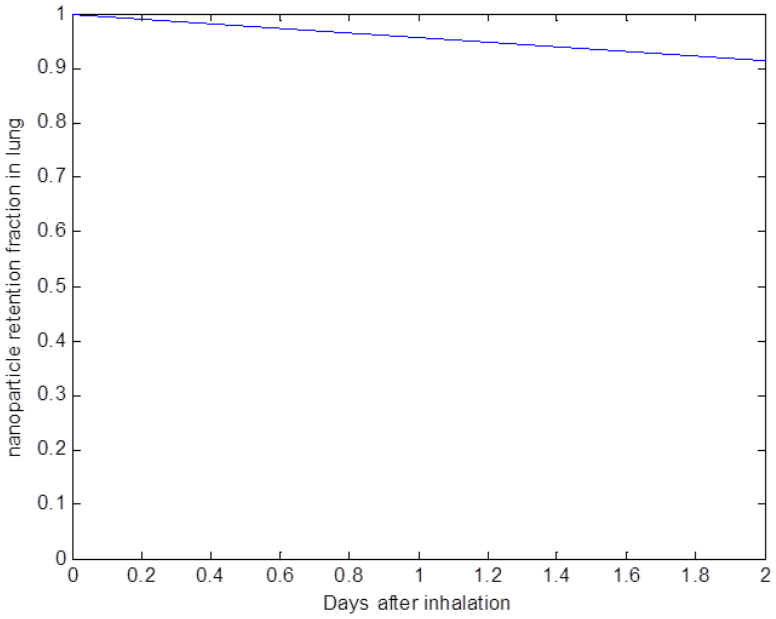

Fig. 7. 3. Nanoparticle retention fraction followed for 2 days after inhalation.

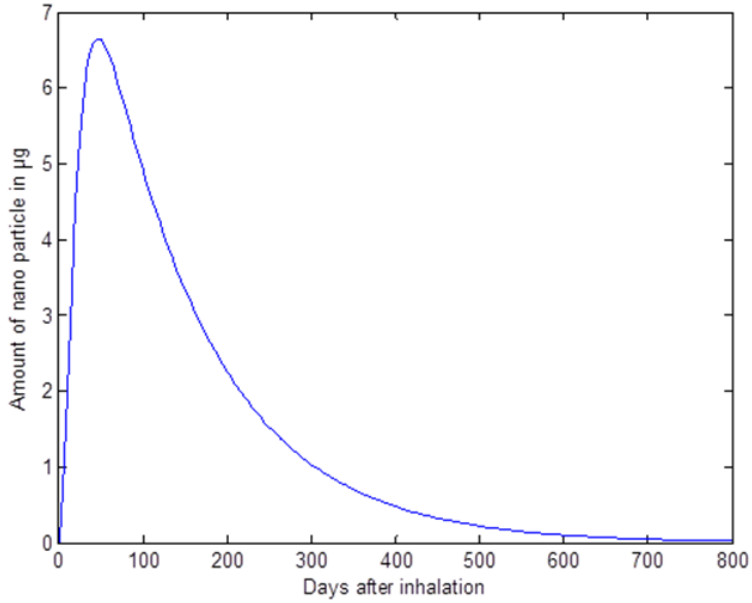

Fig. 7. 4. Amount of nanoparticle translocated to blood circulation system.

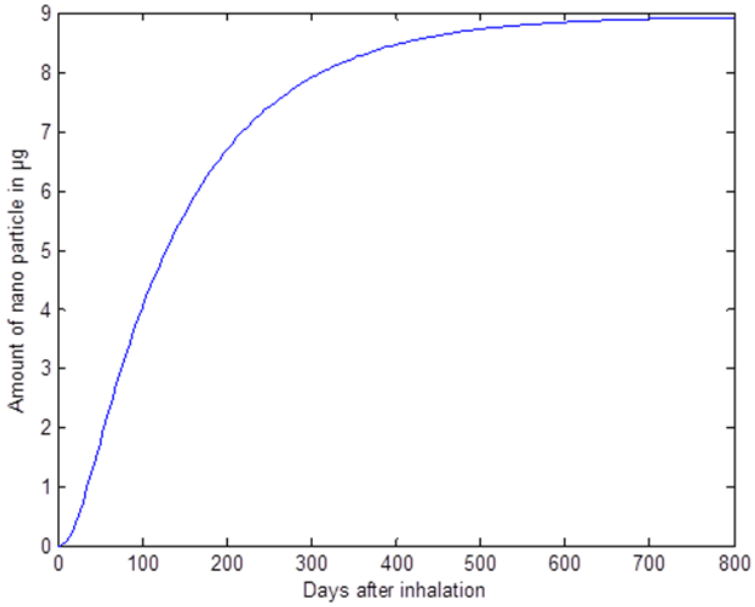

Fig. 7. 5. Amount of nanoparticle translocated to other organs from blood circulation system.

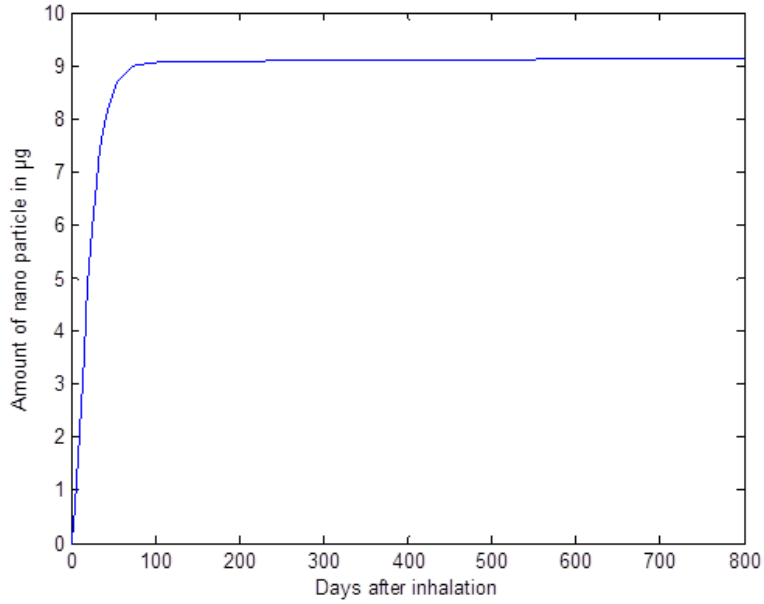

Fig. 7. 6. Amount of nanoparticle translocated to lymphatic system.

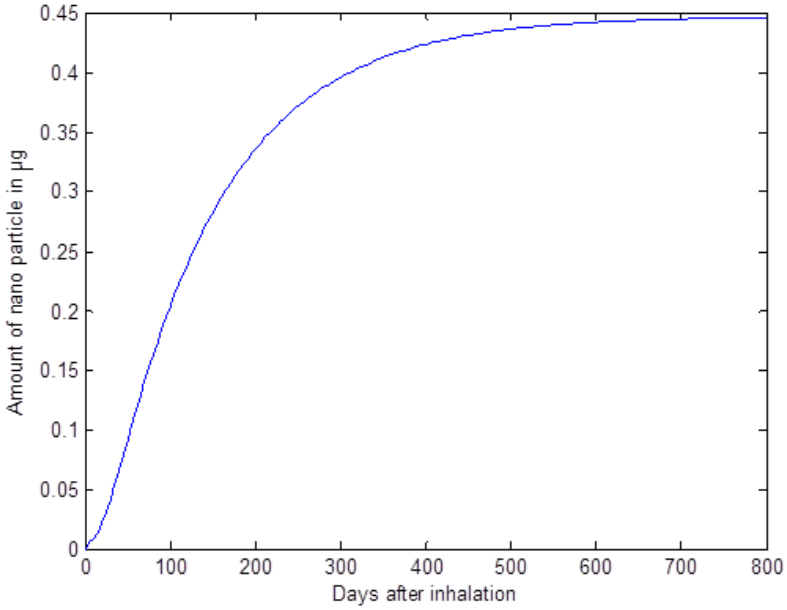

Fig. 7.7. Amount of nanoparticle translocated to olfactory lobe in brain.

7.6 Nanoparticle distribution from blood circulation system to other organs

The whole body physiology based compartment model used in chapter 5, to analyze the distribution of nanoparticles from blood circulation system to other organs or tissues like Kidneys, Gut, Spleen, Pancreas, Lung, Heart, Fat, Muscle, skeletal, Bone, Skin, is extrapolated to a human scenario. Figure 7.8 shows the multi-compartment model depicting the transport of nanoparticle through blood circulation system to the organs and tissues. The amount of nanoparticle in the blood circulation system can be calculated from the multi-compartment model. Based on the assumption that, any soluble or insoluble substance in the blood will be distributed to organs and tissues according to the blood flow rate ratio to each individual organ or tissue, the amount of nanoparticle transporting to these organs and tissues can be calculated. Table 7.3 lists the blood flow rate to individual organs as a fraction of cardiac output calculated for a rat. It is assumed that the nanoparticles translocated to the pulmonary blood system enter the heart before being pumped into the aorta. The clearance of nanoparticles from organs and tissues are not calculated in this study. Clearance of nanoparticles has been found to depend on the material property of the particle. Further investigation should be done in order to calculate the transfer rates of nanoparticles from tissues and organs to the venous blood circulation system. Also it should be noted that the macrophages in liver can phagocytize particles from blood circulation system. Connecting the multi-compartment lung model to the multi-compartment organ model, we can predict the total amount of nanoparticles translocated to each organ and tissue over time. Figure 7.9 to Fig. 7.15 show the distribution of nanoparticles from blood circulation system to Heart, Fat, skeletal Muscle, Bone, Skin, Kidneys and Lung respectively.

Table 7.3. Blood flow rate to individual organs as a fraction of cardiac output calculated for a man (mean data compiled from the literature)

Tissue	**Blood flow rate (fraction of cardiac output)**
Fat	0.07
Muscle skeletal	0.278
Bone	0.122
Skin	0.058
Kidneys	0.141
Gut	0.131
Spleen	0.02
Pancreas	0.01
Liver	Arterial-0.065; Total-0.226

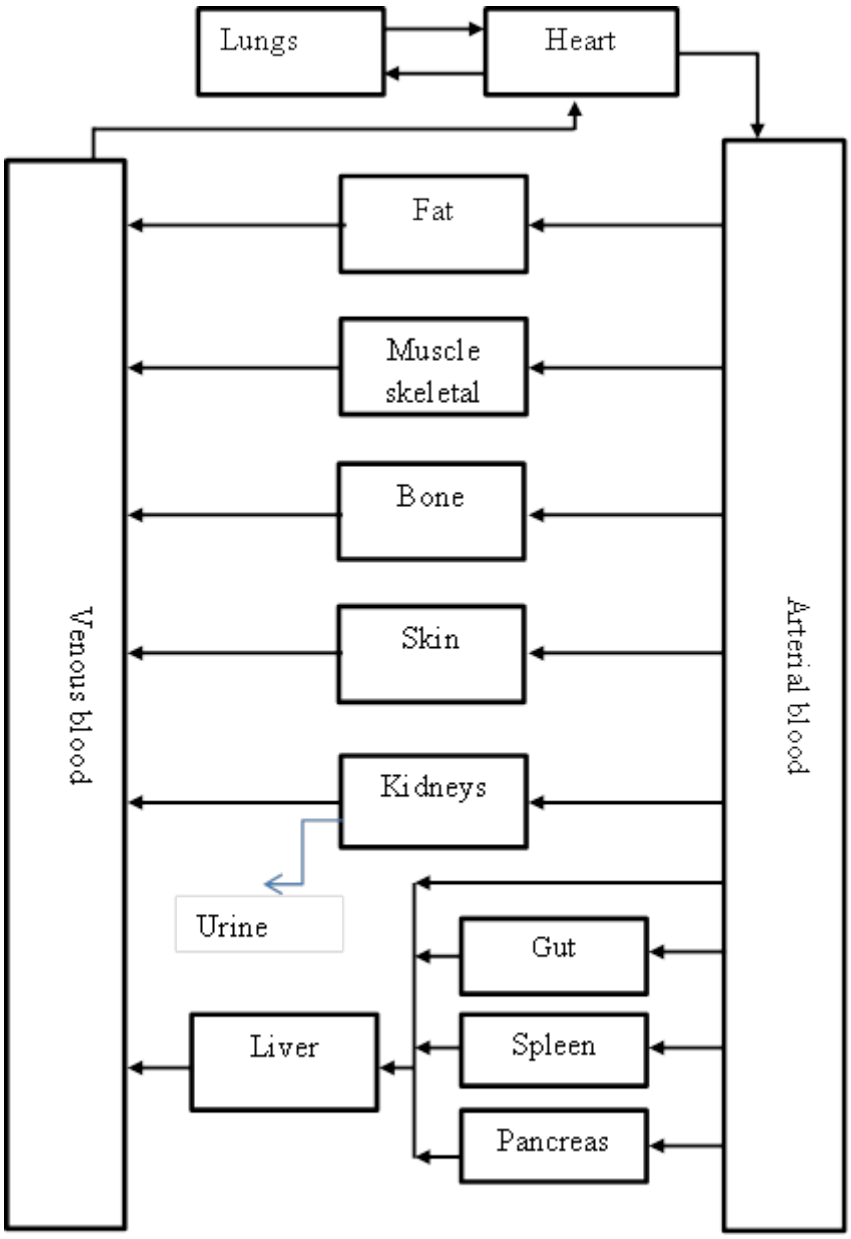

Fig. 7.8. Multi-compartment model depicting the transport of nanoparticle through blood circulation system to the organs and tissues.

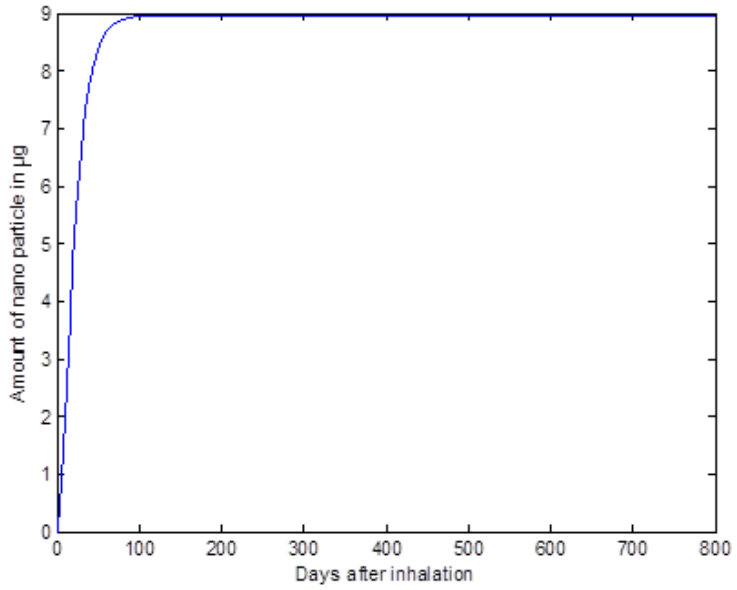

Fig. 7.9. Amount of ultra-fine particles translocated to heart through blood circulation

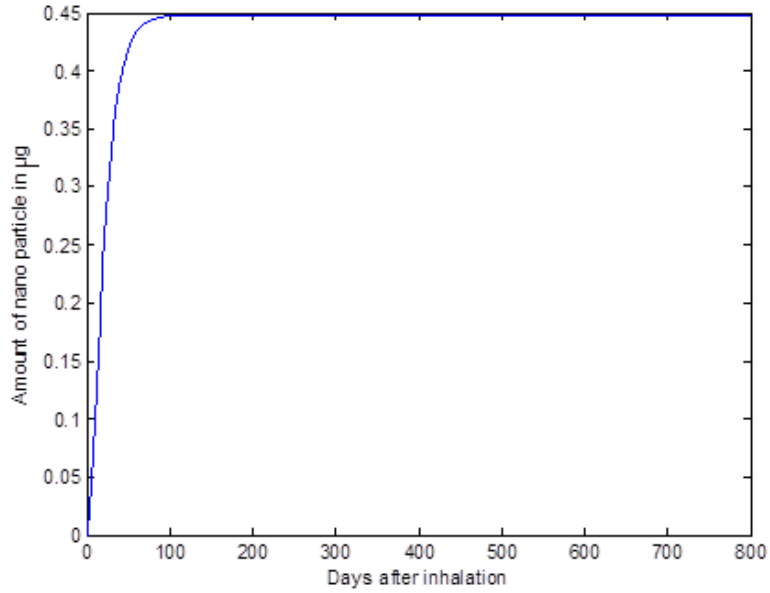

Fig. 7.10. Amount of ultra-fine particles translocated to fat tissue through blood circulation system

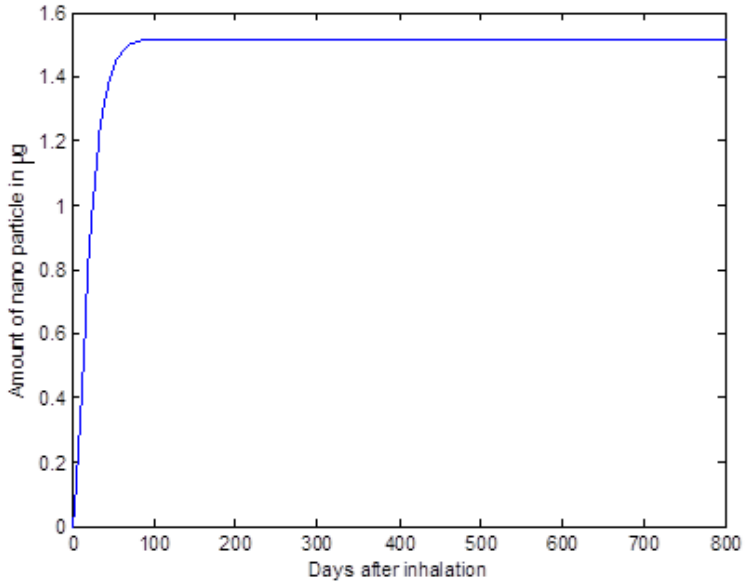

Fig. 7.11. Amount of ultra-fine particles translocated to skeletal muscle tissue through blood circulation system

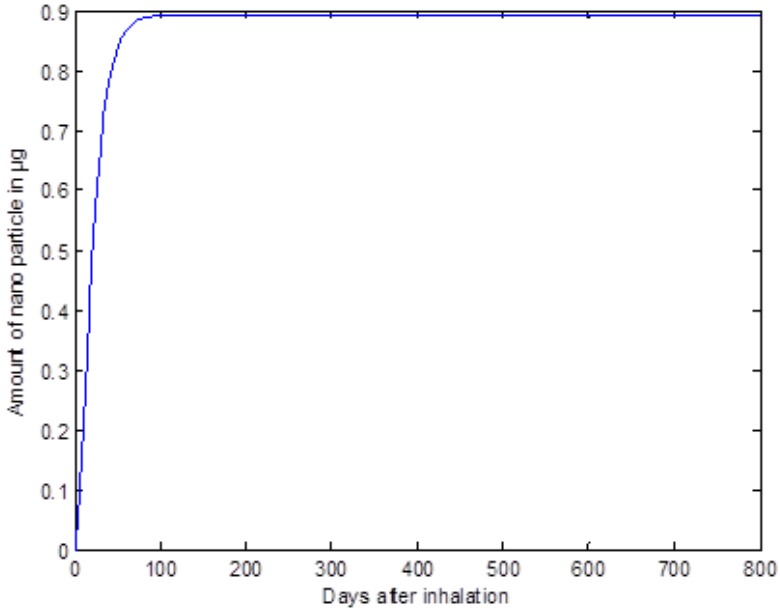

Fig. 7.12. Amount of ultra-fine particles translocated to bone tissue through blood circulation system

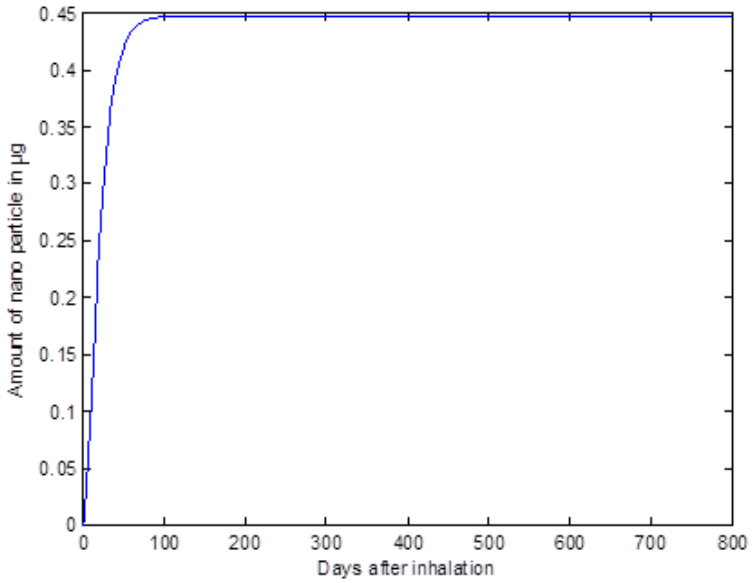

Fig. 7.13. Amount of ultra-fine particles translocated to skin tissue through blood circulation system

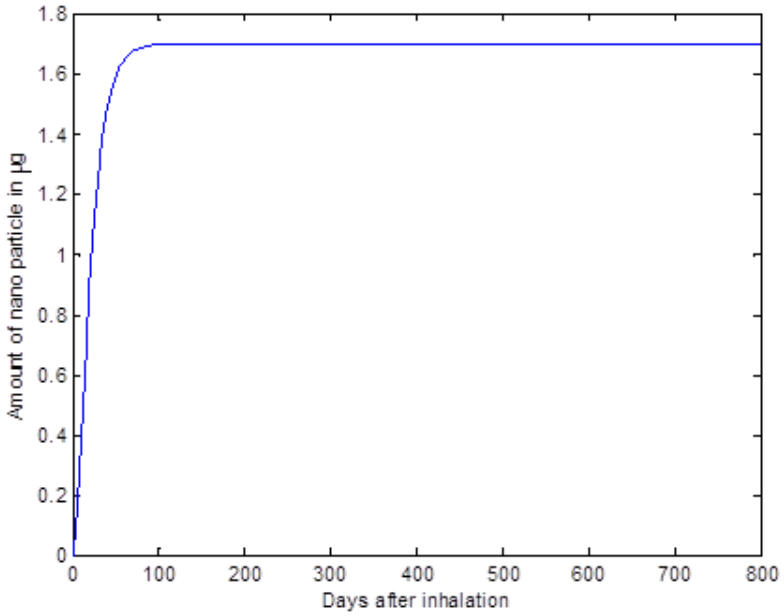

Fig. 7.14. Amount of ultra-fine particles translocated to kidneys through blood circulation system

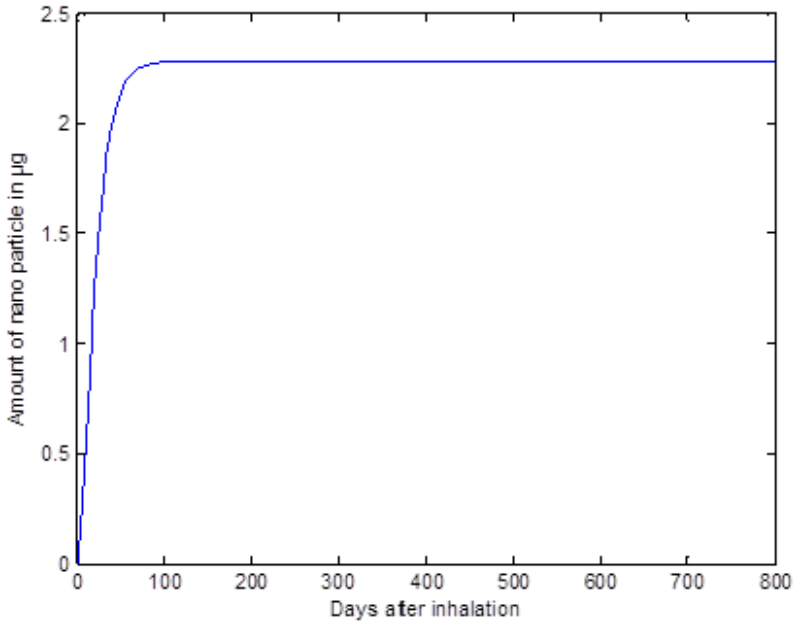

Fig. 7.15. Amount of ultra-fine particles translocated to liver through blood circulation system

7.7 Discussion

Only limited information is available concerning the nanoparticle clearance from the human respiratory tract. Reported animal studies indicate a slow particle clearance especially from alveolar region of the lung. It is expected that the human alveolar particle clearance will be much slower than any other laboratory animals. The multi-compartment model predicted the lung clearance half-life period of nearly 40-50 days. Roth et al., (1993) conducted experiment on human subjects using radioactive Indium ultrafine particles. They reported a half-life period of 40 days for the slow particle clearance which validates the multi-compartment model prediction. Even though the experimental parameters are not the same, the experimental results could be compared because the particle clearance was monitored

after an initial deposition. Fig. 7.2 shows the nanoparticle retention fraction in human lung and Fig. 7.3 shows nanoparticle retention fraction followed for 2 days after inhalation. Roth et al., (1993) measured the lung retention after inhalation for nearly 10 days. Nearly 87 % of the initial ultrafine particle deposition retained in lungs even after 2 days. Similar result can be noticed in Fig. 7.3, where nearly 91 % of the initial deposition was retained even after 2 days. Moller et al., (2007) conducted lung clearance study on human subjects using Technetium (^{99m}Tc) radiolabeled carbon particles (100-nm diameter) and reported particle retention of 96% in the lung periphery after 24 hours. They neglected the particle deposition and mucociliary clearance in the central airways, while measuring the clearance from lung periphery. They also reported 75% particle retention in the central lung airways after 24 hours. One of the advantages of the current model is that, it can predict NP retention in individual lung regions. Considering the alveolar region separately for the current simulation, the model predicts around 99% particle retention 24 hours after exposure, which might be close to experimental result for peripheral lung retention with mucociliary clearance deduction. Also, according to model prediction, the retention in the upper lung airways after 24 hours is around 80%. This does not exclude the particle transfer from alveolar region. Klepczynska-Nyström et al., 2012 conducted experiments on human subjects using radioactive Indium labeled ultrafine carbon particles. They reported around 95% peripheral lung retention, seven days after exposure. They estimated the peripheral lung clearance by subtracting the free activity leaching and mucociliary clearance. The alveolar retention for the present model prediction is around 93%, seven days after exposure. Clearly, the present model predicts similar retention profiles as recorded in the experimental studies.

Figure 7.4 shows the amount of nanoparticle translocated to blood circulation system from lung airways including the alveolar region. The issue of particle translocation to blood circulation system is contradictory. Nemmar et al., (2002) reported that 5- to 10-nm technetium-labeled particles could pass from the lungs into blood and extra pulmonary organs. But Brown et al., (2002) and Mills et al., (2006) reported that the translocation from lungs to secondary organs as negligible. Slow translocation of nanoparticles from lung to blood can be noticed in Figure 7.4, where the amount in blood reached a maximum in 120 days. Based on the plotted result, the amount of nanoparticle in blood was less than 0.1 % of initial deposition after 24 hours. Similar result was reported by Brown et al., (2002). Figure 7.5 shows the amount of nanoparticle translocated to other organs from blood circulation system. Organs other than lungs where the particles can be deposited through blood circulation, like liver, kidney, spleen, brain, heart, were modeled as a closed compartment, 'Other Organs' without any clearance from it. Even though the particles from organs will be cleared to venous blood, it was not considered in this model. This modeling technique will help in predicting the total amount of nanoparticles transferred to organs other than lungs. Nearly 4.2% of the initial deposition reached extra pulmonary organs through blood. The amount of ultra-fine particles translocated from lung to the lymphatic system is plotted in Fig. 7.6. The lymphatic system has significant influence on nanoparticle distribution. Nanoparticles that enter the local tissues from the airways and alveolar region can easily migrate to lymphatic system, resulting in lymphatic system accumulation. In the respiratory system, a vast network of lymphatic vessels drains both the airways and the alveolar regions and terminates in lymph nodes. As per the model prediction, nearly 4.2% of the initial

nanoparticle deposition was cleared from lungs to the lymphatic system. Figure 7.7 shows the amount of nanoparticle translocated to olfactory lobe in brain. Nearly 0.21% of the initial nanoparticle deposition was translocated to olfactory lobe in 800 days. Altogether the multi-compartment model results showed good agreement with the experimental results.

CHAPTER 8
CONCLUSION AND FUTURE WORK

8.1 Conclusion

The field of nanotechnology has made critical influence in our day today life. Nanotechnology has emerged rapidly during the past few years. It has helped to develop new materials with a wide range of applications in in science, technology and medicine. At the same time, toxicological studies have showed that the nanoparticles can cause severe health problems especially when they are inhaled. From the epidemiological and pathological studies of occupational and environmental exposures to nanoparticles, it can be concluded that many of the pulmonary and cardiovascular diseases are an outcome of these inhaled aerosols. Nanoparticles, which constitute a major portion of the urban particulate air pollution, are found to have increased toxicity than larger particles made of the same material. Hence, the rapid development of nanoparticle applications needs to be complemented by assessing possible health implications of those nanoparticles.

In this study a new method to predict the biokinetics of inhaled nanoparticles is proposed. Many of the analytical models developed to predict the deposition of nanoparticles were found inaccurate. Hence a computational method utilizing Computational Fluid Particle Dynamics (CFPD) was used to calculate the nanoparticle deposition in the extra thoracic and lung airways. The CFPD nanoparticle deposition results were found to provide more accurate results. A multi-compartment model was developed to predict the kinetics of deposited nanoparticles from lung airways. The deposition of nanoparticles, in key segments of the

human lung and upper airways, was used as an initial condition for the multi-compartment model. The multi-compartment model was first calibrated using experimental nanoparticle clearance study on rats, as suitable human lung data are not available. Due to the lack of experimental NP-clearance results for humans (most of the experimental nanoparticle clearance studies on humans were followed for hours after exposure), the experimental results for rat-lung clearance were extrapolated to humans, using pharmacokinetic body-weight scaling and the multi-compartment human lung model parameters were optimized using the extrapolated results. The validated multi-compartment human lung model was used to predict the clearance profiles for an exposure to a normal atmospheric NP concentration and the results of the model were found to match existing experimental data. Similar simulations can be done to estimate the risk to any NP exposure. Even though the current model does not consider the physico-chemical properties of the nanoparticles, a method has been suggested to account for NP surface properties. It is hoped that the current model can provide a benchmark in NP-clearance studies.

In summary, the novel contributions of this study include a new compartmental model to predict the biokinetics of inhaled nanoparticles and a more accurate CFPD model to calculate the deposition of inhaled nanoparticles in complete human-lung airways. The results of this study provide critical insight into nanomaterial deposition in human respiratory tracts and subsequent mass transfer to systemic regions. The results are useful in fields such as toxicology and pharmacology to analyze risk to a given exposure of toxic nanomaterial and to assist in the development of multifunctional nanoparticles.

8.2 Input data needed

Input category	
Aerosol concentration	Refer Gangwal et al. (2011)
Breathing pattern	Rest, heavy exercise – determines the number of breaths per minute
Breathing scenario	Nasal , Oral or combined
Particle properties	Diameter (for spherical shape)

8.3 Future work

The CFPD model used in this study is based on many assumptions. In order to improve the accuracy of the current model, higher resolution models must be used. Future research will focus on the following areas.

- Improve CFPD simulations by utilizing:
  - Alveolar wall movement model
  - Realistic lung airway geometry
  - Transient flow simulations

- Particle inertia effects
- Accurate turbulence models like LES

The multi-compartment model for rat was calibrated with experimental clearance result for the lung. Model can be refined with in depth experimental study considering individual transfer paths, particularly clearance through macrophages. The multi-compartment model for human was developed based on extrapolated experimental nanoparticle clearance results from rat. Further refining should be done by calibrating with experimental clearance data in human. Influence of physico-chemical properties of nanoparticles like shape, surface coatings, and surface charge on the deposition and disposition processes should be addressed. Shape is an important factor especially when exposed to carbon nanotubes, fibers, which affects the deposition and disposition of nanoparticles from lungs. Also the effects coagulation and agglomeration of nanoparticles should be studied.

➢ Improve multi-compartment model by:

- Using experimental nanoparticle retention and clearance studies on human.
- Estimating transfer rates based on physico-chemical properties of nanoparticles.
- Estimating the influence of coagulation and agglomeration of nanoparticles on deposition and disposition from lungs.

➢ Improve the organ distribution model by considering the nanoparticle translocation to the venous blood circulation and excretion.

REFERENCES

Chapter 1

Albert, R. E., Lippmann, M., and Briscoe, W. (1969). The characteristics of bronchial clearance in humans and the effect of cigarette smoking. Environ. Health 18: pp. 738-755

Altshuler, B., Palmes, E., and Nelson, N. (1967). Regional aerosol deposition in the human respiratory tract. Inhaled Particles and Vapors, edited by C. N. Davies. Oxford: Perganronp. Pp. 323-335.

Aasmundsson, T., and H.kilburn, K. (1970). Mucociliary clearance rates at various levels of dog lungs. Am. reu. respirat. diseases 102 : pp. 388-397

Asgharian, B., Hofmann, W., & Miller. (2001). Mucociliary clearance of insoluble particles from the tracheobronchial airways of the human lung J. of Aerosol Science 32 pp. 817-832

Bailey, M.R., Hodgson, A., and Smith, H. (1985a). Respiratory Tract Retention of Relatively Insoluble Particles in Rodents. J. Aerosol Sci. 16, pp. 279-293.

Bailey, M.R., Fray, F.A., and James, A.C. (1985b). Long-Term Retention of Particles in the Human Respiratory Tract. J. Aerosol Sci. 16(4), pp. 295-305.

Bellmann, B., Muhle, H., and Creutzenberg, O. (1986). The Effect of a "Nuisance" Dust Inhalation of Lung Clearance. In Aerosols: Formation and Reactivity. 2nd Intl. Aerosol Cpnf. Berlin. Pergamon Journals Ltd. Printed in Great Britain, pp. 209-211.

Basser PJ, McMahon TA, Griffith P. (1989). The mechanism of mucous clearance in cough. J. Biomech. Eng. pp. 111

Bolton, R.E., Vincent, J.H., Jones, A.D., Addison, J., and Beckett, S.T. (1983). An Overload Hypothesis for Pulmonary Clearance of UICC Amosite Fibers Inhaled by Rats. Brit. J. Ind. Med. 40, pp. 264-272.

Brain, J.D. (1986). Toxicological Aspects of Alterations of Pulmonary Macrophage Function. Ann. Rev. Pharmacol. Toxicol. 26, 547-565.

Brain, J.D. (1988). Lung Macrophages: How Many Kinds Are There? What Do They Do? Am. Rev. Resp. Dis. 137, pp. 507-509.

Brain JD, Godleski JJ, Sorokin SP. (1977). Quantification, origin and fate of pulmonary macrophages. In: Brain JD, Proctor DF, Reid LM, eds. Respiratory defense mechanisms. New York: Marcel Dekker, 849-92, pp. 288–97

Cuddihy, R. G., & Yeh, H. C. (1988). Respiratory tract clearance of particles and substances dissociated from particles. In U. Mohr (Ed.), Inhalation toxicology: The design and interpretation of inhalation studies and their use in risk assessment. pp. 169–193 Berlin: Springer.

Ferin, J. (1977). Effect of particle content of lung on clearance pathways. in pulmonary macrophage and epithelial" cells. Eds. C.L. Sanders, R.P.Schneider, G.E. Dagle, and H.A. Ragan. Virginia; Tech. Information Center, Energy Research and Development Administration, pp. 414-423

Ferin, J., and Feldstein, M. L. (1978). Pulmonary clearance and hilar lymph node content in rats after particle exposure. Environ. Res.16: pp. 342-352.

Ferin, J., Oberdörster, G., and Penney, D. P. (1992). Pulmonary retention of ultrafine and fine particles in rats. Am. J. Respir. Cell Mol. Biol. 6: pp. 535–542.

Ferin, J., Oberdörster, G., (1992). Translocation of particles from pulmonary alveoli into the interstitium. Journal of aerosol medicine volume 5 , number 3.

Freedman, A.P. and Robinson, S.E. (1988). Noninvasive Magnetopneumographic Studies of Lung Oust Retention and Clearance in Coal Miners. Irrespirable dust in the Mineral Industries: Health Effects. Characterization and Control. Ed. R.L. Frantz and R.V. Raman. The Pennsylvania State University, University Park. pp. 181-186.

Gradon, L. and Porgorski A. (1992). Mathematical model of dust retention in the human respiratory system. Journal of Aerosol Medicine, pp. 229–2340

Gregoratto, D., Bailey, M R., and Marsh, J w. (2010). Modeling particle retention in the alveolar –interstitial region of the lungs, J. Radiol. Prot. 30, pp. 491-512

Gore D.J and G. Patrick, (1978). The distribution and clearance of inhaled UO2 particles on the first bifurcation and trachea of rats. Physics in Medicine & Biology, pp. 730–737.

Hahn, F.F., Newton, G.J., and Bryant, P.L. (1977). In vitro phagocytosis ofrespirable-sized monodispersed particles by alveolar macrophages. In pulmonary macrophages and epithelial

cells. Ed. C.L. Sanders, R.P.Schneider, G.E. Oagle, and H.A. Ragan. Virginia; Tech. Information Center, Energy Research and Pevelopment Administration, pp. 424-435.

Harmsen, A.G., Muggenburg, B.A., Snipes, M.B., and Bice, P.E. (1985). The Role of Macrophages in Particle Translocation from Lungs of Lymph Nodes. Sei.230, Pec. 13, pp. 1277-1280.

Hilding, A. C. (1957). Ciliary streaining in the lower respiratory tract. Am. J. Physiol. 19 1: pp. 404- 410.

Hilding, A. C. (1961). Experimental studies on some little understood aspects of the physiology of the respiratory tract and their clinical importance. Trans. Am. Acad. Ophthalmol. Otoluryngol. 65: pp. 475-495.

Hofmann W., Asgharian B. (2003). The effect of lung structure on mucociliary clearance and particle retention in human and rat lungs. Toxicol Sci; 73: 448–456.

Hofmann, W and Daschil, F (1986). Biological variability influencing lung dosimetry for inhaled Rn and Rn decay products. Health Physics, 50 pp. 345–367

Iravani, J., and Van as, A. (1972). Mucus Transport in the Tracheobronchial Tree of Normal and Bronchitic Rats. J. Pathol. 106, pp. 81-93

Katsnelson, B. A., Konysheva, L. K., Privalova, L. I., Morosova, K. I. (1992). Development of a multi-compartmental model of the kinetics of quartz dust in the pulmonary region of the lung during chronic inhalation exposure of rats. British Journal of Industrial Medicine 49:pp. 172-181

Kreyling, W.G., Semmler, M., Erbe, F., Mayer, P., Takenaka, S., Schulz, H. (2002). Translocation of ultrafine insoluble iridium particles from lung epithelium to extrapulmonary organs is size dependent but very low. J Toxicol Environ Health; 65: pp. 1513–1530.

Kreyling, W. G., Semmler, M., Möller, W. (2004). Dosimetry and toxicology of ultrafine particles. J Aerosol Med; 17: pp. 140–152.

Kreyling, W.G., Geiser, M., (2010). Deposition and biokinetics of inhaled nanoparticles; Particle and Fibre Toxicology, 7:pp. 2

Lee, P.S., Gerrity, T.R, Hass, F.J. and Lourenco R.V., (1979). A model for tracheobronchial clearance of inhaled particles in man and a comparison with data. IEEE Transactions on Biomedical Engineering, 26, pp. 624–630

Lippmann, M., and K. E. Albert. (1969). The effect of particle size on the regional deposition of inhaled aerosols in the human respiratory tract. Am. Ind. Hyg. Assoc. J. 30: pp. 257-275.

Lundborg, M., Lind B. and Camner P., Ability of Rabbit Alveolar Macrophages to Dissolve Metals, Experimental Lung Research, 7, No. 1 , pp. 11-22

Mercer R.R., M.L. Russell and J.D. Crapo, (1992). Mucous lining layers in human and rat airways. Annual Reviews of Respiratory Diseases, 145 pp. 355.

Morrow, P. E. (1970). Dynamics of dust removal from the lower airways: Measurements and interpretations based upon radioactive aerosols. In: Airway Dynamics, edited by A. Bouhuys. Springfield, Ill: Thomas, pp. 299-312.

Morrow, P.E. (1972). Lymphatic Drainage of the Lung in Dust Clearance. Ann.New York Acad. 200, pp. 46-65.

Morrow, P.E. (1973). Alveolar Clearance of Aerosols. Arch. Intern. Med. 131, 101-108.

Morrow, P.E. (1974). Theoretical and Experimental Models for Dust Deposition and Retention in Man. Rev. Environ. Hlth. 1, pp. 186-212.

Morrow, P.E. (1977). Clearance Kinetics of Inhaled Particles. In Respiratory Defense Mechanisms. Part II, Vol. 5. Eds. J.D. Brain, D.F. Proctor, and L.M. Reid. Marcel Dekker, Inc., New York and Basel, pp. 491-543.

Morrow, P.E. (1988). Possible Mechanisms to Explain Dust Overloading of theLungs. Fund. Appl. Tox. 10, pp. 369-384.

Morrow, P.E., and Mermelstein, R. (1988). Chronic Inhalation Toxicity Studies.In Inhalation Toxicology: The Design and Interpretation of InhalationStudies and Their Use in Risk Assessment. Ed. U. Mohr. Springer Verlag,Berlin, pp. 103-117.

Morrow, P.E., and Yu, C.P. (1985). Models of Aerosol Behavior in Airways. InAerosols in Medicine. Principles. Diagnosis and Therapy. Eds. F. Moren,M.T. Newhouse, and M.B. Dolovich. Elsevier Science Publishers, BiomédicalDivision, Ch. 6, pp. 149-191.

Muhle, H., Bellmann, B., Crentzenberg, 0., Stöber, W., Kilpper, R., Mac Kenzie, J., Morrow, P., and Mermelstein, R. (1988). Pulmonary Peposition, Clearance and Retention of Test Toner, TÍO2 and Quartz Puring a Long-Term Inhalation Study in Rats. The Toxicologist 8, pp. 272.

Nemmar, A., Vanbilloen, H., Verbruggen, A., Mortelmans, A., Hoylaerts, M., Hoet, M., Thomeer, M.,and Nemery, B. (2001). Evaluation of the passage of inhaled 99mTc-labelled ultrafine carbon particles into the systemic circulation in humans. [Abstracts, 2001 Intl. Conference, May 18–23, San Francisco, CA, ATS]. Am. J. Respir. Crit. Care Med. 163: pp. A311.

Newhouse, M. T., F. J. Wrigmt, M. Dolovich, and O. L. Hopkins. (1970). Clearance of RISA aerosol from the human lung. In: Airway Dynamics, edited by A. Bouhuys. Springfield, Ill.

Oberdörster, G., Morrow, P.E., and Spurny, K. (1988). Size dependent lymphatic short-term clearance of amosite fibers in the lung. Ann. Occup. Hyg.32, pp. 149-156.

Oberdörster G, Ferin J, Gelein R, Soderholm SC, Finkelstein J. (1992). Role of the alveolar macrophage in lung injury: studies with ultrafine particles. Environ Health Perspect. 97: pp. 193–199

Oberdörster G., Sharp Z., Atudorei V., Elder A., Gelein R., Lunts A., Kreyling W., Cox C. (2002). extrapulmonary translocation of ultrafine carbon particles following whole-body inhalation exposure of rats; journal of toxicology and environmental health, part a, 65: pp. 1531–1543,

Patrick, G. (1979). The retention of uranium dioxide particles in the trachea of the rat. International Journal of Radiation Biology, 35, pp. 571–576

Patrick, G. and Stirling C., (1977). The retention of particles in large airways of the respiratory tract. Proceedings of the Royal Society of London B. Biological Sciences, 198 , pp. 455–462

Ross SM, Corrsin S. (1974). Results of an analytical model of mucociliary pumping. J Appl Physiol; 37: pp. 333-400.

Sanchis, J., M. Dolovich, R. Chalmers, and M. Newhouse. (1972). Quantitation of regional aerosol clearance in the normal human lung. J. Appl. Physiol. 33(6):pp. 757-762.

Semmler M, Seitz J, Erbe F, Mayer P, Heyder J, Oberdörster G, Kreyling WG: (2004). Long-term clearance kinetics of inhaled ultrafine insoluble iridium particles from the rat lung, including transient translocation into secondary organs. Inhal Toxicol, 16: pp. 453-459.

Semmler-Behnke M, Takenaka S, Fertsch S, Wenk A, Seitz J, Mayer P, Oberdörster G, Kreyling WG. (2007). Efficient elimination of inhaled nanoparticles from the alveolar region: evidence for interstitial uptake and subsequent re-entrainment onto airways epithelia. Environ Health Perspect: pp. 728–733

Smith, T.J. (1985). Development and Application of a Model for Estimating Alveolar and Interstitial Dust Levels. Ann. Occup. Hvq. 29(4), pp. 495-516.

Smith D. J., Gaffney E. A., Blake J.R. (2007). A Viscoelastic Traction Layer Model of Muco-Ciliary Transport , Bulletin of Mathematical Biology 69: pp. 289–327

Snipes, M.B., Boecker, B.B., and MC Clellan, R.O. (1983). Retention of Monodisperse or Polydisperse Aluminosilicate Particle Inhaled by Dogs, Rats, and Mice. Toxicol. Appl. Pharmacol. 69, pp. 345-362.

Snipes, M.B., Chavez, CT., and Muggenburg, B.A. (1984). Disposition of 3-, 7-, and 13-um Microspheres Instilled into Lungs of Pogs. Environ. Res. 33, pp. 333-342.

Stöber W, Morrow P.E and Hoover M.D., (1989). Compartmental modeling of the long-term retention of insoluble particles deposited in the alveolar region of the lung. Fundam. appl. Toxicol., 13 pp. 823–842

Strom, K.A., Chan, T.L., and Johnson, J.T. (1988). Pulmonary Retention of Inhaled Submicron Particles in Rats: Diesel Exhaust Exposures and Lung Retention Model. Ann. Occup. Hyg. 32, pp. 645-657

Takenaka, S., Karg, E., Kreyling,W., Lentner, B., Schulz, H., Ziesenis, A., Becke, H., Heinzmann, U., Schramel, P., and Heyder, J.(2003). Distribution patterns of inhaled ultrafine silver particles in the rat lung. AAAR PM Meeting Particulate Matter

Tran C. L., Jones A. D, Cullen R. T. (1999). Mathematical modeling of the retention and clearance of low-toxicity particles in the lung, Inhalation Toxicology, 11:1059–1076,

Watson A.Y. and Brain J.D., (1979). Uptake of iron oxide aerosols by mouse airway epithelium. Laboratory Investigations, pp. 450–459.

Yu, C. P., Hu, J. P., Yen, B. M., Spektor, D. M., & Lippmann, M. (1986). Models for mucociliary particle clearance in lung airways. In: S.D. Lee, T. Schneider, L.D. Grant, & P.J. Verkerk (Eds.), Aerosols: Research, risk assessment and control strategies pp. 569–578.

Yu, C.P., and Morrow, P.E. (1987). A Non-Linear Model of Particle Retention in the Lung. Presented at American Association of Aerosol Research, Seattle Washington, Sept. pp. 14-17

Chapter 2 and chapter 3

Asgharian, B., and Price, O. T. (2006). Airflow distribution in the human lung and its influence on particle deposition. Inhalation Toxicology. 18:795-801.

Balashazy, I., and Hoffman, W. (1995). Deposition of aerosols in asymmetric airway bifurcations. J. Aerosol Sci. 26:273–292.

Balashazy, I., Heistracher, T., and Hoffman, W. (1996). Air flow and particle deposition patterns in bronchial airway bifurcations: The effect of different CFD models and bifurcation geometries.

Balashazy, I., Hoffman, W. and Heistracher, T. (1999). Computation of local enhancement factors for the quantification of particle deposition patterns in airway bifurcations. J. Aerosol Sci. 30:185–203.

Berg, E.J., Weisman, J.L., Oldham, M.J., Robinson, R.J. (2010). Flow field analysis in a compliant acinus replica model using particle image velocimetry (PIV). J Biomech 43:1039–1047

Cheng, K.H.,Cheng,Y.S.,Yeh, H.C.,& Swift, D.L.(1995). Deposition of ultrafine aerosols in the head airways during natural breathing and during simulated breath-holding using replicate human upper airway casts. Aerosol Science and Technology, 23, 465–474.

Comer, J. K., Kleinstreuer, C., and Zhang, Z., (2001). Flow structures and particle deposition patterns in double-bifurcation airway models. Part 2. Aerosol transport and deposition. J. Fluid Mech. 435:55–80

Comer, J. K., Kleinstreuer, C., and Zhang, Z. (2001). Flow structures and particle deposition patterns in double-bifurcation airway models. Part 1. Air flow fields. J. Fluid Mech. 435:25–54 J. Aerosol Med. 9:287–301.

Darquenne, C. (2001). A realistic two-dimensional model of aerosol transport and deposition in the alveolar zone of the human lung. Journal of Aerosol Science, 32, 1161–1174.

Darquenne, C. (2002). Heterogeneity of aerosol deposition in a two-dimensional model of human alveolated ducts. Journal of Aerosol Science, 33, 1261–1278

Darquenne, C., and Paiva, M. (1996). Two- and three-dimensional simulations of aerosol transport and deposition in alveolar zone of the human lung. Journal of Applied Physiology 80:1401-1414.

Haber, S, Yitzhak, S.D., and Tsuda, A. (2003). Gravitational deposition in a rhythmically expanding and contractingalveolus. J. Appl. Physiol., 95:657–671

Haber, S. and Tsuda , A. (1998). The effect of flow generated by a rhythmically expanding pulmonary acinus on aerosoldynamics. J. Aerosol Sci., 29:309–322

Haefeli-Bleuer, B. and Weibel, E.R. (1988). Morphometry of the human pulmonary acinus. Anat. Rec., 220:401–414

Harding, E. and Robinson, R. J. (2010). Flow in a terminal alveolar sac model with expanding walls using computational fluid dynamics, Inhalation Toxicology, 2010; 22(8): 669–678

Henry, F.S., Butler, J.P., and Tsuda, A. (2002). Kinematically irreversible acinar flow: a departure from classical dispersive aerosol transport theories. Journal of Applied Physiology 92:835-.45

Heyder, J, Blanchard JD, Feldman, HA, and Brain JD. (1988). Convective mixing in human respiratory tract: estimates with aerosol boli. J. Appl. Physiol., 64:1273–1278

Jiang, J., & Zhao, K., (2010). Airflow and nanoparticle deposition in rat nose under various breathing and sniffing conditions—a computational evaluation of the unsteady and turbulent effect. Journal of Aerosol Science, 41, 1030–1043.

Jayaraju, S.T., Brouns, M., Lacor, C., Belkassem, B., Verbanck, S. (2008). Large eddy and detached eddy simulations of fluid flow and particle deposition in a human mouth throat, Journal of Aerosol Science, vol. 39, pp. 862-875

Kelly, J.T., Asgharian, B., Kimbell, J.S., Wong, BA. (2004). Particle deposition in human nasal airway replicas manufactured by different methods. Part II: ultrafine particles. Aerosol Sci. Technol. 38:1072–79

Kepler, G.M., Richardson, R.B., Morgan, K.T., Kimbell, J.S. (1998). Computer simulation of inspiratory nasal airflow and inhaled gasuptake in a rhesus monkey, Toxicol. Appl. Pharmacol. 150–11.

Kim, C.S., Jaques, P.A. (2004). Analysis of total respiratory deposition of inhaled ultrafine particles in adult subjects as various breathing patterns. Aerosol Sci. Technol. 38:525–40

Kim, C. S., & Jaques, P. A. (2005). Total lung deposition of ultrafine particles in elderly subjects during controlled breathing. Inhalation toxicology, 17(7-8), 387-399

Kimbell, J.S., Gross, E.A., Joyner, D.R. (1993). Godo, M.N., Morgan K.T., Application of computational fluid dynamics to regional dosimetry of inhaled chemicals in the upper respiratory tract of the rat, Toxicol. Appl. Pharmacol. 121 253–263.

Kleinstreuer, C., Zhang, Z. (2009). An adjustable triple-bifurcation unit (TBU) model for air-particle flow simulations in human tracheobronchial airways. J. Biomech. Eng. Trans. ASME 131:021007

Kleinstreuer, C., Zhang, Z., Donohue, J.F. (2008). Targeted drug-aerosol delivery in the human respiratory system. Annu. Rev. Biomed. Eng. 10:195–220

Kumar, H, Tawhai, MH, Hoffman, EA, Lin CL. (2009). The effects of geometry on airflow in the acinar region of the human lung. J Biomech 42:1635–1642.

Li, Z., & Kleinstreuer, C. (2011). Airflow analysis in the alveolar region using the lattice-Boltzmann method. Medical and Biological Engineering and Computing, 49(4), 441-451.

Longest, P.W., and Vinchurkar S. (2007). Validating CFD predictions of respiratory aerosol deposition: Effects of upstream transition and turbulence, Journal of Biomechanics, vol. 40, pp. 305-316

Ma, B. and Darquenne, C. (2011). Aerosol deposition characteristics in distal acinar airways under cyclic breathing conditions. J Appl Physiol 110: 1271–1282

Ma, B., Lutchen, K. (2009). CFD simulation of aerosol deposition in an anatomically based human large-medium airway model. Ann. Biomed. Eng. 37:271–85

Martonen, T. B. and Katz, I. M. (1993). Deposition patterns of aerosolized drugs within human lungs: effects of ventilatory parameters. Pharm. Res. 10, 871-878.

Martonen, T. B. and Katz, I. M. (1993). Deposition patterns of poly disperse aerosols within human lungs. J. Aerosol Med. 6, 251-274.

Mazaheri, A.R. and Ahmadi, G. (2003). Inspiratory Particle Deposition in the Upper Three Airway bifurcation. 21st Annual Conference of the American Association for Aerosol Research, AAAR 2002, Charlotte, NC, October 7-11, 2002.

Mazaheri, A.R. and Ahmadi, G. (2004). Modeling Inspiratory Particle Deposition. ASME Heat Transfer/Fluid Engineering Summer Conference, Charlotte, NC, July 11-15, 2004.

Matida, E.A., Finlay, W.H., Lange, C.F., Grgic, B. (2004). Improved numerical simulation of aerosol deposition in an idealized mouth-throat, Journal of Aerosol Science, vol. 35, pp. 1-19

Menter, F.R. (1993). Zonal two-equation k-w turbulence model for aerodynamic flows. AIAA Paper 1993-2906.

Menter, F.R., (1994). Two-equation eddy-viscosity turbulence models for engineering applications. AIAA-Journal, 32(8), pp. 269-289, 1994

Moskal, A., and Gradon, L. (2002). Temporary and spatial deposition of aerosol particles in the upper human airways during breathing cycle. Journal of Aerosol Science, vol. 33, pp. 1525-1539

Nowak, N., Kakade, P.P. & Annapragada, A.V. (2003). Computational fluid dynamics simulation of airflow and aerosol deposition in human lungs. Ann Biomed Engineering 31, 374–390.

Oakes, JM, Day, S, Weinstein, SJ, Robinson, RJ. (2010). Flow field analysis in expanding healthy and emphysematous alveolar models using particle image velocimetry. J Biomech Eng 132:021008-1–021008-9.

Shi, H., Kleinstreuer, C., Zhang, Z. (2008). Dilute suspension flow with nanoparticle deposition in a representative nasal airway model. Physics of Fluids; **20**:013301.

Sosnowski, T. R., Moskal, A., and Gradon, L. (2006). Dynamics of Oropharyngeal Aerosol Transport and Deposition With the Realisitic Flow Pattern, Inhalation Toxicol., 18(10) , pp. 773–780.

Sznitman, J., Heimsch, F., Heimsch, T., Rusch, D., Rosgen, T. (2007). Three-dimensional convective alveolar flow induced by rhythmic breathing motion of the pulmonary acinus. J Biomech Eng 129:658–665.

Sznitman, J., Heimsch T., Wildhaber J.H., Tsuda A., Rosgen T. (2009). Respiratory flow phenomena and gravitational deposition in a three-dimensional space-filling model of the pulmonary acinar tree. J Biomech Eng 131:031010-1–031010-16.

Sznitman, J., Schmuki, S., Sutter, R., Tsuda, A., Rosgen, T. (2007b). CFD investigation of respiratory flows in a space-filling pulmonary acinus model. Model Med Biol VII 12:147–155.

Tian, L. and Ahmadi, G. (2007). Particle Deposition in Turbulent Duct Flows - Comparisons of Different Model Predictions. J. Aerosol Science, Vol. 38, pp. 377-397.

Tsuda, A., Henry, F.S., and Butler, J.P., (1995). Chaotic mixing of alveolated duct flow in rhythmically expanding pulmonaryacinus. J. Appl. Physiol., 79:1055–1063

Tsuda, A., Otani, Y., and Butler, J.P., (1999). Acinar flow irreversibility caused by perturbations in reversible alveolar wallmotion. J. Appl. Physiol., 86:977–984

Tsuda, A., Rogers, R.A., Hydon, P.E., and Butler J.B., (2002). Chaotic mixing deep in the lung. Proc. Natl. Acad. Sci. USA,99:10173–10178

Varghese, S.S., Frankel, S.H. (2003).Numerical modeling of pulsatile turbulent flow in stenotic vessels. Journal of Biomechanical Engineering—Transactions of the ASME; 125:445–460.

Weibel, E.R., 1963. Morphometry of the Human Lung. Academic Press, New York, Springer, Berlin

Xi, J., and Longest P. W. (2007). Effects of oral airway geometrycharacteristics on the diffusional deposition of inhaled nanoparticles. ASME J. Biomech. Eng. 130:011008.

Yu, G., Z. Zhang, Z., Lessmann, R. (1998), Fluid flow and particle diffusion in the human upper respiratory system, Aerosol Sci. Technol. 28 146–158.

Yu, G., Zhang, Z., Lessmann, R. (1996), Computer simulation of the flow field and particle deposition by diffusion in a 3-D human airway bifurcation, Aerosol Sci. Technol. 25 338–352.

Zhang Y., Finlay WH. (2005). Measurement of the effect of cartilaginous rings on particle deposition in a proximal lung bifurcation model. Aerosol Sci. Technol. 39:394–99

Zhang,Z., & Kleinstreuer, C.(2011). Computational analysis of airflow and nanoparticle deposition in a combined nasal-oral-tracheobronchial airway model. Journal of Aerosol Science, 42, 174–194.

Zhang Z, Kleinstreuer C. (2011). Laminar-to-turbulent fluid–nanoparticle dynamics simulations: Model comparisons and nanoparticle-deposition applications. International Journal for Numerical Methods in Biomedical Engineering; **27**: 1930–1950

Zhang, Z., Kleinstreuer, C., and Kim, C. S. (2008). Airflow and Nanoparticle Deposition in a 16-Generation Tracheobronchial Airway Model. Ann. Biomed. Eng., 36(12):2095–2110.

Zhang, Z. and Kleinstreuer, C. (2003). "Low-Reynolds-number turbulent flows in locally constricted conduits: A comparison study," AIAA J. 41, 831

Zhang, Z., Kleinstreuer, C. (2004). Airflow structures and nano-particle deposition in a human upper airway model. Journal of Computational Physics; 198:178–210.

Zhang, Z., Kleinstreuer, C. (2003). Low-Reynolds-number turbulent flows in locally constricted conduits: a comparison study. AIAA Journal; 41:831–840.

Zhang, Y., and Finlay, W. H. (2005). Measurement of the effect of cartilaginous rings on particle deposition in a proximal lung bifurcation model. Aerosol Science and Technology. 39:394-399

Zhang, Z., and Kleinstreuer, C. (2002). Transient airflow structures and particle transport in a sequentially branching lung airway model. Phys. Fluids 14:862–880.

Zhang, Z., Kleinstreuer C. Donohue, J. F., and Kim, C. S. , (2005) Comparison of micro- and nano-size particle depositions in a human upper airway model. J. Aerosol Sci. 36:211–233.

Zhang, Z., Kleinstreuer, C. and Kim, C. S., (2002). Cyclic micron size particle inhalation and deposition in a triple bifurcation lung airway model. J. Aerosol Sci. 33:257–281

Zhang, Z., Kleinstreuer, C. (2001). Effect of particle inlet distributions on deposition in a triple bifurcation lung airway model. J. Aerosol Med. 14:13–29

Chapter 4

Albert, R.E. and Arnett, L.C. (1955). Clearance of Radioactive Dust from the Human Lung. Arch. Ind. Health 12:99-106

Brown, J.S., Zeman, K.L., Bennett W. D. (2002). Ultrafine particle deposition and clearance in the healthy and obstructed lung. Am J Respir Crit Care Med, 166: 1240-1247

Brown, J. S., Wilson,W. E., and Grant, L.D. (2005). Dosimetric comparisons of particle deposition and retention in ras and humans. Inhal. Toxicol. 17(7–8):355–386.

Donaldson, K., V. Stone, C.L. Tran, W. Kreyling & Borm, P.J.A. (2004). Nanotoxicology. Occup. Environ. Med. 61, 727–728.

Elder, A.; Gelein, R.; Silva, V.; Feikert, T.; Opanashuk, L.; Carter, J.; Potter, R.; Maynard, A.; Ito, Y.; Finkelstein, J.; Oberdörster, G. (2006). Translocation of inhaled ultrafine manganese oxide particles to the central nervous system. Environ Health Perspect, 114: 1172-1178

Geiser, M., Rothen-Rutishauser, B., Kapp, N., Schürch, S., Kreyling, W., Schulz, H., Semmler, M., Im Hof V, Heyder, J., Gehr, P. (2005). Ultrafine particles cross cellular membranes by non-phagocytic mechanisms in lungs and in cultured cells. Environ Health Perspect, 113:1555-1560.

Geiser, M., Kreyling, W. G. (2010), Deposition and bio kinetics of inhaled nanoparticles. Particle and Fibre Toxicology , 7:2

Holgate, S.T. (2010). Exposure, uptake, distribution and toxicity of nanomaterials in humans. J Biomed Nanotechnol;6(1):1–19

ICRP. (1994). Human Respiratory Tract Model for Radiological Protection. Annals of the ICRP. Publication 66, 24((1-3)).

Kato, T., Yashiro, T., Murata, Y. (2003), Evidence that exogenous substances can be phagocytized by alveolar epithelial cells and transported into blood capillaries, Cell Tissue Res. 311:47–51.

Katsnelson, B. A., Konysheva, L. K., Privalova, L. I., and Morosova, K. I. (1992). Development of a multicompartmental model of the kinetics of quartz dust in the pulmonary region of the lung during chronic inhalation exposure in rats. Br. J. Ind. Med. 49:172–181

Kreyling, W.G., Takenaka, S., Schumann, G., Ziesenis, A.: (2001). Particles are predominantly transported from the canine epithelium towards the interstitial spaces and not to larynx! Analogy to human lungs? Am J Respir Crit Care Med, 163:A166

Kreyling, W.G., Semmler, M., Erbe, F., Mayer, P., Takenaka, S., Schulz, H. (2002). Translocation of ultrafine insoluble iridium particles from lung epithelium to extrapulmonary organs is size dependent but very low. J Toxicol Environ Health, 65:1513-1530.

Kreyling, W.G. Hirn, S., Schleh, C. (2010). Nanoparticles in the lung. Nature biotechnology volume 28 number 12 December (2010)

Kuempel, E. D., (2000). Comparison of human and rodent lung dosimetry models for particle retention. Drug. Chem. Toxicol. 23(1):203–222.

Kuempel, E. D., O'Flaherty, E. J., Stayner, L. T., Smith, R. J., Green, F. H. Y., and Vallyathan, V. (2001a). A biomathematical model of particle clearance and retention in the lungs of coal miners. Part I. Model development. Regul. Toxicol. Pharmacol. 34:69–87.

Kuempel, E.D., Tran, C.L., Smith, R.J., Bailer, A.J. (2001). A biomathematical model of particle clearance and retention in the lungs of coal miners. II. Evaluation of variability and uncertainty. Regulatory Toxicol Pharmacol , 34:88-101

Kuempel, E. D., and Tran, C. L. (2002). Comparison of human lung dosimetry models: Implications for risk assessment. Ann. Occup. Hyg. 46(suppl, 1):337–341.

MacCalman L, Tran, C. L., and Kuempel, E. (2009). Development of a bio-mathematical model in rats to describe clearance, retention and translocation of inhaled nanoparticles throughout the body, Journal of Physics: Conference Series **151** ((2009)) 012028.

Mills, NL; Amin, N.; Robinson, S.D.; Anand, A.; Davies, J.; Patel, D.; de la Fuente J.M.; Cassee, F.R.; Boon, N.A.; Macnee, W.; Millar, A.M.; Donaldson, K.; Newby, D.E . (2006). Do inhaled carbon nanoparticles translocate directly into the circulation in humans? Am J Respir Crit Care Med, 173: 426-431

Morrow, P. E., (1988). Possible mechanisms to explain dust overloading of the lungs. Fundam. Appl. Toxicol. 10:369–384.

Morrow, P. E., (1992). Dust overloading of the lungs: Update and appraisal. Toxicol. Appl. Pharmacol. 113:1–12.

Nemmar, A., H. Vanbilloen, M.F. Hoylaerts, P.H.M. Hoet, A. Verbruggen & Nemery, B. (2001). Passage of intratracheally instilled ultrafine particles from the lung into the systemic circulation in hamster. Am. J. Respir. Crit. Care Med. 164(9), 1665–1668.

Nemmar, A, Hoet, P.H.M., Vanquickenborne ,B., Dinsdale, D., Thomeer, M., Hoylaerts, M.F. (2002). Passage of inhaled particles into the blood circulation in humans. Circulation; 105:411–4.

Oberdörster, G., Sharp, Z., Atudorei, V., Elder, A., Gelein, R., Lunts, A., Kreyling, W.G., Cox, C. (2002). Extrapulmonary translocation of ultrafine carbon particles following whole-body inhalation exposure of rats. J Toxicol Environ Health, 65:1531-1543.

Oberdörster, G., Sharp, Z. ,Atudore, V. ,Elder, A ., Gelein, R. ,Kreylin, ,W. (2004).Translocation of inhaled ultrafine particle to the brainI. Inhal Toxicol 16(6/7):437-445

Oberdörster, G., Oberdörster, E., Oberdörster, J. (2005). Nanotoxicology: an emerging discipline evolving from studies of ultrafine particles. Environ Health Perspect, 113:823-839.

Semmler, M., Seitz ,J., Erbe, F., Mayer, P., Heyder, J., Oberdörste,r G., Kreyling, W.G. (2004). Long-term clearance kinetics of inhaled ultrafine insoluble iridium particles from the rat lung, including transient translocation into secondary organs. Inhal Toxicol, 16:453-459.

Semmler-Behnke, M., Takenaka, S., Fertsch, S., Wenk, A., Seitz, J., Mayer, P., Oberdörster, G., Kreyling, W.G. (2007). Efficient elimination of inhaled nanoparticles from the alveolar region: Evidence for interstitial uptake and subsequent reentrainment onto airways epithelia. Environ Health Perspect, 115:728-733.

Stöber, W., Morrow, P. E., and Hoover, M. D. (1989). Compartmental modeling of the long-term retention of insoluble particles deposited in the alveolar region of the lung. Fundam. Appl. Toxicol. 13:823–842.

Stöber, W., Morrow, P. E., and Morawietz, G. (1990a). Alveolar retention and clearance of insoluble particles in rats simulated by a new physiology-oriented compartmental kinetics model. Fundam. Appl. Toxicol. 15:329–349.

Stöber, W., Morrow, P. E., Morawietz, G., Koch, W., and Hoover, M. (1990b). Developments in modeling alveolar retention of inhaled insoluble particles in rats. J. Aerosol Med. 3(suppl. 1):129– 154

Smith, T. J. (1985). Development and application of a model for estimating alveolar and interstitial dust levels. Amer. Occup Hyg. 29,495-516.

Strom, K. A., Chan, T. L., and Johnson, J. T., (1987). Pulmonary Retention of Inhaled Submicron Particles in Rats: Diesel Exhaust Exposures and Lung Retention Model. Research Publication GMR-5718, General Motors Research Laboratories, Warren, MI

Sturm, R. (2007). A computer model for the clearance of insoluble particles from the tracheobronchial tree of the human lung. Computers in Biology and Medicine.37 (5):680-90.

Takenaka, S. Karg, E. Kreyling, W. Lentne,r B. Möller, W. Behnke-Semmler, M. Jennen, L. Walch, A. Michalke, B. Schramel, P. (2006). Distribution Pattern of Inhaled Ultrafine Gold Particles in the Rat Lung. Inhal Toxicol, 18: 733-740.

Tran, C.L., Jones, A., Cullen, R.T., Donaldson, K. (1999). Mathematical modeling of the retention and clearance of low-toxicity particles in the lung. Inhal Toxicol; 11:1059–76.

Tran, C. L., and Buchanan, D. (2000). Development of a biomathematical lung model to describe the exposure-dose relationship for inhaled dust among U.K. coal miners. Edinburgh, UK: Institute of Occupational Medicine. IOM Research Report TM/00/02.

Vincent, J. H., Jones, A. D., Johnston, A. M., Mcmillan, C, Bolton, R. E., and Cowie, H. (1987). Accumulation of inhaled mineral dust in the lung and associated lymph nodes: Implications for exposure and dose in occupational lung disease. Ann. Occup. Hyg. 31, 375-393

Wang, J.X.; Chen, C.Y.; Yu, H.W.; Sun, J.; Li, B.; Li, Y.F.; Gao, Y.X.; He, W.; Huang, Y.Y.; Chai, Z.F . (2007). Distribution of TiO 2 particles in the olfactory bulb of mice after nasal inhalation using microbeam SRXRF mapping techniques. Journal of Radioanal Chem, 272: 527-531.

Chapter 5

Oberdörster, G., Sharp, Z. ,Atudore, V. ,Elder, A. , Gelein, R. ,Kreylin, W. (2004).Translocation of inhaled ultrafine particle to the brainI. Inhal Toxicol 16(6/7):437-445

Semmler, M., Seitz, J., Erbe, F., Mayer, P., Heyder, J., Oberdörster, G., Kreyling, W.G. (2004). Long-term clearance kinetics of inhaled ultrafine insoluble iridium particles from the rat lung, including transient translocation into secondary organs. Inhal Toxicol, 16:453-459.

Semmler-Behnke, M., Takenaka, S., Fertsch, S., Wenk, A., Seitz, J., Mayer, P., Oberdörster, G., Kreyling, W.G. (2007). Efficient elimination of inhaled nanoparticles from the alveolar region: Evidence for interstitial uptake and subsequent reentrainment onto airways epithelia. Environ Health Perspect, 115:728-733.

Takenaka, S. Karg, E. Kreyling, W. Lentner, B. Möller, W. Behnke-Semmler, M. Jennen, L. Walch, A. Michalke, B. Schramel, P. (2006). Distribution Pattern of Inhaled Ultrafine Gold Particles in the Rat Lung. Inhal Toxicol, 18: 733-740.

Chapter 6

Bailey, M.R., Kreyling, W.G., Andre, S. Batchelor, A. Black, A. Collier, CG. Drosselmeyer, E. Ferron, G.A., Foster, P. Haider, B., Hodgson, A., Metivier, H. Moores, S.R. Morgan, A. Müller, H.L Patrick, G. Pearman, I. Pickering, S. Ramsden, D. Stirling and C. Talbot, R.J. (1989). An Interspecies Comparison of the Lung Clearance of Inhaled Monodisperse Cobalt Oxide Particles - Part I: Objectives and Summary of Results. J. Aerosol Sei. 20, 169-188.

Boxenbaum, H. (1982). Interspecies scaling, allometry, physiological time, and the ground plan of pharmacokinetics. J Pharmacol Biopharm 10:201-227.

Dedrick, R; Bischoff, KB; Zaharko, DS. (1970). Interspecies correlation of plasma concentration history of methotrexate (NSC-740). Cancer Chemother Rep 54: 95-101

Dedrick, RL. (1973). Animal scale-up. J Pharmacokinet Biopharm 1:435-61

Guyton, A. C. (1971). Textbook of Medical Physiology. 4th edn. Philadelphia, PA: W. B. Saunders.

Hill, A. V. (1950). The dimensions of animals and their muscular dynamics. Proc. R. Inst. Great Britain 34, 450-471

Jarabek, AM. (1995a). Interspecies extrapolation based on Mechanistic Determinants of Chemical Disposition. Hum Ecol Risk Assess 1:641-662.

Jarabek, AM. (1995b). The application of dosimetry models to identify key processes and parameters for default dose-response assessment approaches. Toxicol Lett 79:171-184

Klepczynska-Nyström, A., A. Sanchez-Crespo, M. Andersson, R. Falk, A. Lundin, B. Larsson, and M. Svartengren. (2012).The pulmonary deposition and retention of indium-111 labeled ultrafine carbon particles in healthy individuals. Inhal. Toxicol. 24:645-651,

Kreyling, W. G., Hodgson, A., Guilmette, R. A., Scarlett, C., Badmin, A., & Stradling, G. N. (1998). Interspecies comparison of lung clearance using monodisperse terbium oxide particles. *Radiation protection dosimetry*, *79*(1-4), 241-243.

Lindstedt, S. L. (1987). Allometry: body size constraints in animal design. In: Drinking Water and Health. Pharmacokinetics in Risk Assessment. Vol. 8. Washington, D.C.: National Academy Press.

Mordenti, J. (1986). Man versus beast: pharmacokinetic scaling in mammals. J. pharma. Sci. 75, 1028-1040.

Prothero, O. (1979). Heart weight as a function of body weight in mammals. Growth 43, 139-150.

Rhomberg, LR and Caprario, LC. (1999). Cross-species and cross-route comparisons of acute lethal doses: Further results of analysis of a large database. In: Society for Risk Analysis Annual Meeting, December 6.

Rhomberg, L.R. and Wolff, S.K. (1998). Empirical scaling of single oral lethal doses across mammalian species base on a large database. Risk Anal 18:741-753.

Rhomberg, L.R. and Lewandowski, T.A. (2004). Methods for identifying a default cross-species scaling factor. Submitted to USEPA under Contract No. 3W-0477-NASX. Available at: http://www.epa.gov/raf/publications/pdfs/RHOMBERGSPAPER.PDF.

Seaton, A., Godden D., MacNee W., and Donaldson K. (1995). Particulate air pollution and acute health effects. The Lancet 345:176-178.

StahL, W. R. (1967). Scaling of respiratory variables in mammals. J. appl. Physiol. 48, 1052-1059.

Travis, CC and White, RK. (1988). Interspecies scaling of toxicity data. Risk Anal 8:119-125.

Travis, C. C., R. K. White, and R. C. Ward. (1990). Interspecies extrapolation of pharmacokinetics. J. Theor. Biol. 142:285-304.

USEPA (U.S. Environmental Protection Agency). 1992a. Draft Report: A cross-species scaling factor for carcinogen risk assessment based on equivalence of mg/kg3/4/Day; Notice. Fed Reg 57: 24152-2424173.

USEPA (U.S. Environmental Protection Agency). 1992b. Guidelines for Exposure Assessment. EPA/600/Z-92/001. Risk Assessment Forum, Washington, DC. Available at: http://www.epa.gov/raf/publications/guidelines-for-exposure-assessment.htm.

USEPA (U.S. Environmental Protection Agency). 1994. Methods for Derivation of Inhalation Reference Concentrations and Application of Inhalation Dosimetry, EPA/600/8-90/066F. Available at: http://cfpub.epa.gov/ncea/cfm/recordisplay.cfm?deid=71993

USEPA (U.S. Environmental Protection Agency). (2002). A Review of the Reference Dose and Reference Concentration Processes. EPA/630/P-02/002F. Risk Assessment Forum, Washington, DC. Available at: http://www.epa.gov/raf/publications/review-reference-dose.htm.

USEPA (U.S. Environmental Protection Agency). (2005). Guidelines for Carcinogen Risk Assessment. EPA/630/P-03/001F. Risk Assessment Forum, Washington DC. Available at: www.epa.gov/cancerguidelines.

Watanabe, K; Bois, FY; Zeise, L. (1992). Interspecies extrapolation: a reexamination of acute toxicity data**.** Risk Anal 12:301-10.

West, GB; Brown, JH; Enquist, BJ. (1997). A general model for the origin of allometric scaling laws in biology. Science 276:122-126.

Yates, F. E. & Kugler, P. N. (1986). Similarity principles and intrinsic geometrics: contrasting approaches to interspecies scaling. J. pharma. Sci. 75, 1019-1027.

Chapter 7

Brown, J.S., Zeman, K.L., Bennett, W.D. (2002). Ultrafine particle deposition and clearance in the healthy and obstructed lung. Am J Respir Crit Care Med, 166: 1240-1247

Gangwal S., Brown J.S., Wang A., Houck K.A., Dix D.J., Kavlock R.J., Hubal E. A. C., (2011). Informing selection of nanomaterial concentrations for ToxCast in vitro testing based on occupational exposure potential. Environ Health Perspect. 119:1539–1546.

Mills, N.L.; Amin, N.; Robinson, S.D.; Anand A; Davies, J.; Patel, D.; de la Fuente, J.M.; Cassee FR; Boon NA; Macnee W; Millar AM; Donaldson K.; Newby D.E. (2006). Do inhaled carbon nanoparticles translocate directly into the circulation in humans? Am J Respir Crit Care Med, 173: 426-431

Möller, W., Felten, K., Sommerer, K., Scheuch, G., Meyer, G., Meyer, P., Haussinger, K., Kreyling, W.G. (2008). Deposition, retention, and translocation of ultrafine particles from the central airways and lung periphery. Am J Resp Crit Care Med, 177:426-432.

Nemmar, A., Hoet, P.H.M., Vanquickenborne, B., Dinsdale, D., Thomeer M, Hoylaerts, M.F. (2002). Passage of inhaled particles into the blood circulation in humans. Circulation; 105:411–4.

Oberdörster, G., Sharp, Z.,Atudore, V. ,Elder, A. , Gelein, R. ,Kreylin, W. (2004).Translocation of inhaled ultrafine particle to the brainI. Inhal Toxicol 16(6/7):437-445

Roth, c., Scheuch, G. and Stahlhofen, W., (1993) , Clearance of the human lungs for ultrafine particles, J.Aerosol Sci. . Vol. 24. Suppl. 1. Pp S95 – S96.

Semmler, M., Seitz, J., Erbe, F., Mayer, P., Heyder, J., Oberdörster, G., Kreyling, W.G. (2004). Long-term clearance kinetics of inhaled ultrafine insoluble iridium particles from the rat lung, including transient translocation into secondary organs. Inhal Toxicol, 16:453-459.

Semmler-Behnke, M., Takenaka, S., Fertsch, S., Wenk, A., Seitz J., Mayer, P., Oberdörster, G., Kreyling, W.G. (2007). Efficient elimination of inhaled nanoparticles from the alveolar region: Evidence for interstitial uptake and subsequent reentrainment onto airways epithelia. Environ Health Perspect, 115:728-733.

Tran CL., Graham M. and Buchanan D., (2001). A bio mathematical model for rodent and human lung describing exposure, dose, and response to inhaled silica, Institute of Occupational Medicine, Research Report TM/01/04 April 2001

APPENDICES

APPENDIX A1

Deposition fraction calculated for rat lung models

A.1.1 Deposition fraction for experiment conducted by Oberdörster et al. (2004)

Table A1.1. Experimental exposure conditions (Oberdörster et al. 2004)

Particle type	^{13}C
Particle diameter	37 nm (CMD) with GSD=1.66
Aerosol concentration	170 μg / m^3
Duration of exposure	6 hours
Breathing scenario	Inhalation
Length of follow up	7 days

The parameters given in Table A1.1 were specified in MPPD. MPPD can produce multiple plots with deposition fraction in each lobe and airway generation. Fig. A1.1 shows the deposition fraction in Head, Tracheobronchial and Pulmonary region. Individual airway deposition fraction from detailed report produced by MPPD was used to differentiate the deposition fractions in the tracheobronchial and bronchiolar regions. Similar to the human lung model, rat lung model has 9 generations in the tracheobronchial region and 10 to 16 generations in the bronchiolar region and 17 to 41 generations in the alveolar region. Deposition fraction in each region was calculated by adding the deposition fraction in each airway generation. Table A1.2 shows the deposition fraction in each region.

The amount of nanoparticle deposited in each lung region following the inhalation exposure was calculated using the deposition formula given in Eqn. A 1.1

D=concentration*ventilation rate*daily exposure in hr.*deposition fraction (A 1.1)

Ventilation rate = Tidal volume*breathing frequency per min.*60 (in m^3/hr.)

= $2.1*10^{-6}$ (m^3) *102*60 per hr.

= 0.012852 m^3/ hr.

Deposition in extra-thoracic region, D1 = 170 * 0.012852 * 6 * 0.097

= 1.3 μ g

Deposition in tracheobronchial region, D2 = 170 * 0.012852 * 6 * 0.0181

= 0.2373 μ g

Deposition in bronchiolar region, D4 = 170 * 0.012852 * 6* 0.0448

= 0 .5873 μ g

Deposition in alveolar region, D7 = 170 * 0.012852 * 6 * 0.22

= 2.884 μ g

Total initial deposition in lung = 5.01 μ g

Table A1.2. Deposition fraction in each region

Region	Deposition fraction	Initial deposition (μ g)
Head	0.097	1.3
Tracheobronchial	0.0181	0.2373
Bronchiolar	0.0448	0 .5873
Alveolar	0.22	2.884

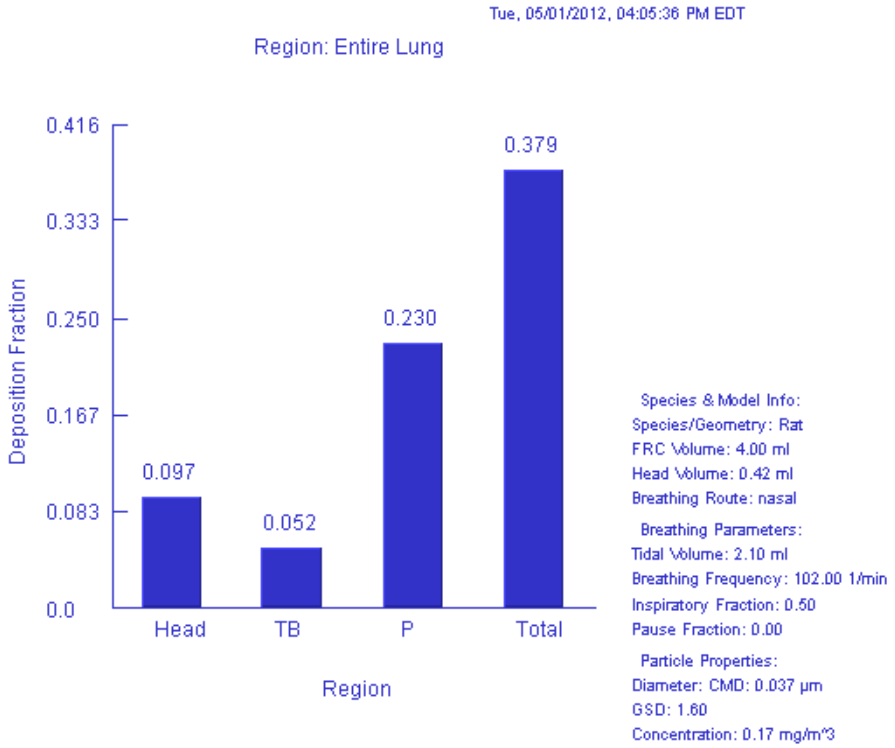

Fig. A1.1. MPPD plot showing deposition fraction in the Head, Tracheobronchial and Pulmonary region

A.1.2 Deposition fraction for experiment conducted by Semmler et al. (2004)

The parameters given in Table A1.3 were specified in MPPD. MPPD can produce multiple plots with deposition fraction in each lobe and airway generation. Fig. A1.2 shows the deposition fraction in Tracheobronchial and Pulmonary region. Individual airway deposition fraction from detailed report produced by MPPD was used to differentiate the deposition fractions in the tracheobronchial and bronchiolar regions. Similar to the human lung model, rat lung model has 9 generations in the tracheobronchial region and 10 to 16 generations in the bronchiolar region and 17 to 41 generations in the alveolar region. Deposition fraction in each region was calculated by adding the deposition fraction in each airway generation. Table A1.4 shows the deposition fraction in each region.

Table A1.3 Experimental exposure conditions (Semmler et al. 2004)

Particle type	Iridium (^{192}Ir)
Particle diameter	15 - 20 nm (CMD)
Aerosol concentration	0.2 mg / m^3
Duration of exposure	1.25 hours
Breathing scenario	Endotracheal
Length of follow up	6 months
Breathing frequency	45 / min
Inspiratory fraction	75-80 %

The amount of nanoparticle deposited in each lung region following the inhalation exposure was calculated using the deposition formula given in Eqn. A1.2

D=concentration*ventilation rate*daily exposure in hr.*deposition fraction (A1.2)

Ventilation rate = Tidal volume*breathing frequency per min.*60 (in m^3/hr.)

= $2.1*10^{-6}$ (m^3) *45*60 per hr.

= $5.67 * 10^{-3}$ m^3/ hr.

Deposition in tracheobronchial region, D2 = $0.2 * 5.67 * 10^{-3} * 1.25 * 0.156$

= 0.22113 μ g

Deposition in bronchiolar region, D4 = $0.2 * 5.67 * 10^{-3} * 1.25 * 0.268$

= 0 .37989 μ g

Deposition in alveolar region, D7 = $0.2 * 5.67 * 10^{-3} * 1.25 * 0.323$

= 0.4578525 μ g

Total initial deposition in lung = 1.06 μ g

Table A1.4. Deposition fraction in each region

Region	**Deposition fraction**	**Initial deposition (μ g)**
Tracheobronchial	0.156	0.22113
Bronchiolar	0.268	0 .37989
Alveolar	0.323	0.4578525

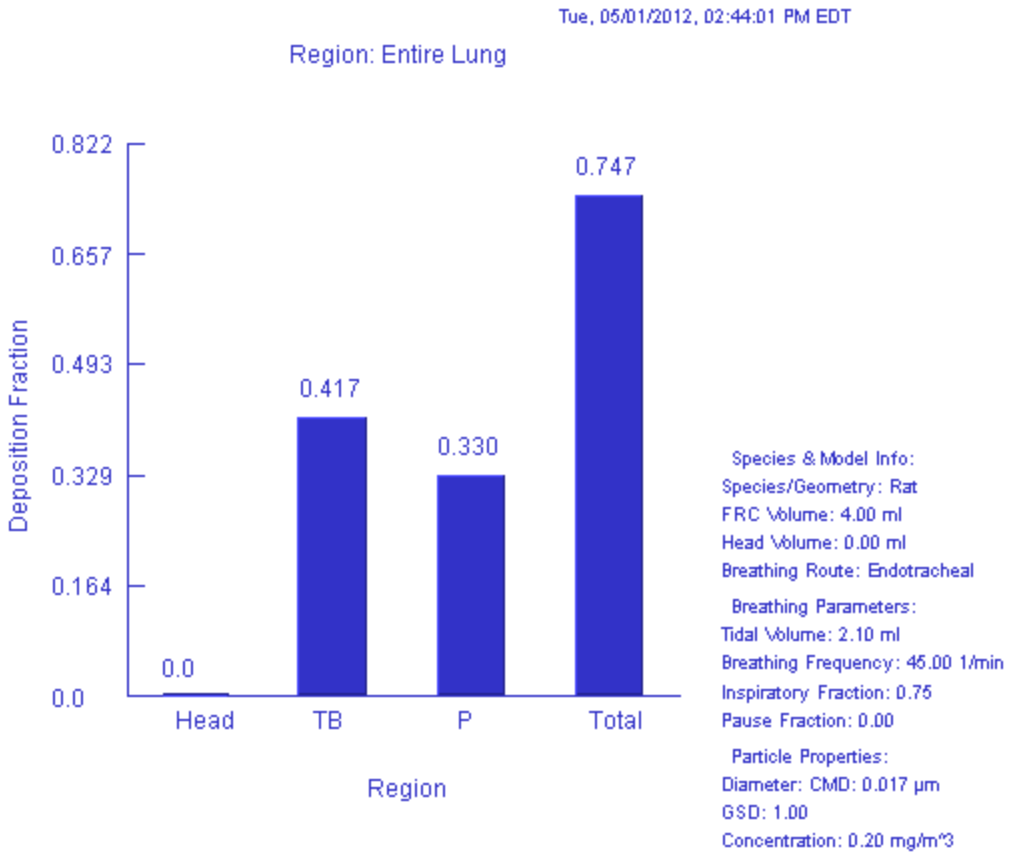

Fig. A1.2. MPPD plot showing deposition fraction in Tracheobronchial and Pulmonary region

A.1.3 References

Oberdörster, G., Sharp, Z. ,Atudore, V. ,Elder, A ., Gelein, R. ,Kreylin, ,W. (2004).Translocation of inhaled ultrafine particle to the brainI. Inhal Toxicol 16(6/7):437-445

Semmler, M., Seitz ,J., Erbe, F., Mayer, P., Heyder, J., Oberdörste,r G., Kreyling, W.G. (2004). Long-term clearance kinetics of inhaled ultrafine insoluble iridium particles from the rat lung, including transient translocation into secondary organs. Inhal Toxicol, 16:453-459.

APPENDIX A2

Deposition fraction calculated for human lung models

The amount of nanoparticle deposited in each lung region following the inhalation exposure was calculated using the deposition formula given in Eqn. A2.1 The deposition fraction data are taken from the CFPD simulation results.

D=concentration*ventilation rate*daily exposure in hr.*deposition fraction (A2.1)

Ventilation rate (vr) = Tidal volume*breathing frequency per min.*60 (in m^3/hr.)

= $1000*10^{-6}$ (m^3) * breathing frequency per min *60 per hr.

Deposition in extra-thoracic region, D1 = conc. * vr * duration * DF in head

Deposition in tracheobronchial region, D2 = conc. * vr * duration * DF in TB region

Deposition in bronchiolar region, D4 = conc. * vr * duration * DF in bronchiolar region

Deposition in alveolar region, D7 = conc. * vr * duration * DF in alveolar region

Deposition fraction in human lung was calculated using CFPD simulations. Weibel (1963) human lung model has 9 generations in the tracheobronchial region and 10 to 16 generations in the bronchiolar region and 17 to 23 generations in the alveolar region. Deposition fraction in each region was calculated by adding the deposition fraction in each airway generation. A

tidal volume of 500 ml was assumed for both exposures. For Semmler et al., (2004) exposure, a breathing frequency of 7.5 breath/minute was used, since the experimental exposure on rat was done with nearly half the normal breathing frequency. For Oberdörster et al., (2004), a normal breathing frequency of 15 breath/minute was used. Table A2.1 and Table A2.2 show the deposition fraction in each region for the exposure conditions from Oberdörster et al., (2004) and Semmler et al., (2004).

Table A2. 1. Deposition fraction (from chapter 3) and initial deposition in each region for the exposure conditions from Oberdörster et al., (2004)

Region	**Deposition fraction**	**Initial deposition (μ g)**
Head	0.004437	2.03658
Tracheobronchial	0.00767	3.521
Bronchiolar	0.0791	36.31
Alveolar	0.3748	172.0332

Table A2. 2. Deposition fraction (from chapter 3) and initial deposition in each region for the exposure conditions from Semmler et al., (2004)

Region	**Deposition fraction**	**Initial deposition (μ g)**
Tracheobronchial	0.015866331	0.894375
Bronchiolar	0.144438125	8.1
Alveolar	0.691891677	38.925

A.2.1 References

Oberdörster, G., Sharp, Z., Atudore, V., Elder, A., Gelein, R., Kreylin,W. (2004).Translocation of inhaled ultrafine particle to the brainI. Inhal Toxicol 16(6/7):437-445

Semmler, M., Seitz ,J., Erbe, F., Mayer, P., Heyder, J., Oberdörste,r G., Kreyling, W.G. (2004). Long-term clearance kinetics of inhaled ultrafine insoluble iridium particles from the rat lung, including transient translocation into secondary organs. Inhal Toxicol, 16:453-459.

APPENDIX A3

Direct Numerical Simulation and Hybrid CFD-PBPK model for Lung Fluid Particle Dynamics

A3.1 Direct Numerical Simulation for Lung Fluid Dynamics

The air flow through the airways is complex with multiple secondary flows and vortices. The extra-thoracic airways which include nasal, oral, pharynx, larynx passages have complex geometrical shapes which produce transitional turbulent flows. Transitional turbulent flows are always hard to predict. But understanding the flow behavior in the airways is vital, since the transport and deposition of inhaled aerosols particles depend on the characteristics of the flow.

Many researchers have focused on using turbulence models in order to capture the transitional turbulence in the airways. The most common turbulence model used for lung flow simulations are Reynolds Averaged Navier Stokes (RANS) model with two equations (Stapleton et al., 2000; Matida et al., 2004; Ma and Lutchen, 2008). Low-Reynolds Number (LRN) k-ω model and Shear Stress Transport (SST) model can produce better result for flows with transitional turbulence. Zhang and Kleinstreuer (2003) analyzed the flow transition from laminar to turbulence in a straight tube with 75% constriction and an oral airway with partial occlusions using four widely used RANS turbulence models, namely LRN k$-\varepsilon$ model, renormalization group (RNG) k$-\varepsilon$ model, LRN k$-\omega$ model and Menter k$-\omega$ model. They found that LRN k$-\omega$ model with appropriate damping functions and turbulence constants can produce accurate transitional turbulence. Zhang and Kleinstreuer

(2011) confirmed that LES and SST k-ω model do not have measurable differences in predicting laminar, transitional and fully turbulent flows. But Matida et al., (2006) concluded that the RANS model does not capture the airway flow characteristics accurately. The Eddy Interaction Model (EIM), used to find the fluctuating component of velocities (assumes fluctuating velocities to be isotropic, an assumption that is inappropriate, especially near the walls where strong anisotropic turbulent structures develop) has been reported to be inaccurate when the aerosol deposition results were compared with the experimental deposition results. Since transitional turbulence has significant effect on particle deposition, more accurate turbulence models focusing on transitional turbulence are needed for aerosol deposition. It was found using in-vitro experimental studies that the aerosol particles are deposited in the upper airways due to both inertial impaction and turbulent diffusion mechanisms. Hence, researchers have employed accurate turbulence models like Large Eddy Simulation (LES) (Matida et al., 2006; Jayaraju et al., 2008; Jin et al., 2007) and Direct Numerical Simulation (DNS) (Lin et al., 2007) in an attempt to obtain a more accurate prediction of aerosol deposition in the human upper airways. DNS provides actual instantaneous fluid velocities whereas LES provides filtered instantaneous fluid velocities. LES has accuracy in between DNS and RANS. LES is based on the hypothesis that the relevant scales in turbulent flows can be separated into large-scale and small-scale (sub-grid) components. In LES the larger scales of the flow are resolved and the smaller scales are modeled. For this purpose, the Navier–Stokes equations are subjected to a filtering procedure, with which the smaller scales are filtered out. These unresolved scales are then

modeled via an appropriate sub grid-scale (SGS) modeling term, and this modeling term is incorporated into the equation for the resolved scales.

In DNS, the Navier-Stokes equations are solved numerically without using any traditional turbulence models. DNS requires accurate numerical methods of higher order to approximate differential equations and there by fully capture a wide range of length and time scales. The classical finite difference, finite volume, finite element and spectral methods have been often used in DNS. The grid for the geometry determines the resolution of the scale. A large number of grid points are required to resolve small spatial scales. Since the required number of grid points increases faster than the square of the Reynolds number, DNS is at present feasible only at low or moderate Reynolds numbers. Also DNS requires use of very small time steps for time advancement; otherwise the error associated with small scales will be higher. Specifying boundary conditions is another difficulty associated with DNS modeling. Turbulent inflow and outflow boundary conditions must be specified which needs generation of random fluctuating components by some other methods.

The information regarding the smallest length, time and velocity scales should be known for the successful simulation using DNS. This information is crucial in order to develop space grid and choose time steps of adequate scales. It can be acquired by applying Kolmogorov turbulence scale. The Kolmogorov scale, η is given by

$$\eta = (\nu^3/\varepsilon)^{1/4}$$

where ν is the kinematic viscosity and ϵ is the rate of kinetic energy dissipation.

The number of grid points *N* in each direction required for DNS of homogeneous isotropic turbulence will then be of the order $N \sim (Re_T)^{9/4}$ where $Re_T = u_T L/\nu$, where u_T represents frictional velocity, L is typical length scale.

Number of time steps required is given by $N_{time} = t_{total} / \Delta t$ where $\Delta t = 0.003L/ (\sqrt{Re_T} * u_T)$

It shows that a highly refined mesh is needed to resolve all the turbulent scales and since the simulation is transient, the resulting data at each time step must be stored, which results in high computational cost. In the upper airways, the laryngeal jet produces turbulent structures which influences the airflow and particle transfer. Also in the nasal region, due to high turbulent dispersion, increased aerosol deposition has been reported. Hence a DNS model for turbulence can provide accurate results for the aerosol transport and deposition in the airways by capturing all the turbulent scales, but the computational expenses makes it less feasible.

A3.2 Hybrid CFD-PBPK model

Pharmacokinetic models can be used to estimate the transfer of inhaled aerosols into the tissues and blood circulation system (systemic compartments) in conjunction with the CFD model. The hybrid models are important in cases in which the deposited aerosols are not rapidly cleared from the tissue. The concentration of aerosols in the tissue can affect its further deposition from the carrying medium and hence the transport of aerosols through air, tissue and blood must be modeled simultaneously. The modeling approach is similar to the one used for modeling less soluble, less reactive vapor, in which the wall concentration will always be greater than zero. For vapors with high reactivity and solubility, the assumption of

wall concentration to be zero has been found to be accurate. The CFD models are used to simulate the transport and deposition of nanoparticles through air. The output from the CFD modeling analysis can then be used as initial conditions for pharmacokinetic model.

The diffusion of deposited particles in to the systemic system depends on the conducting airway tissue structure. The conducting airways consist of the nasal, oral, pharyngeal and tracheobronchial airways. The walls of the conducting airways are covered with a protective mucus layer. Mucus layer composed of a sol phase of low viscosity and a blanket of an overlaying gel phase of high viscosity. The mucus layer is hovered over the ciliated epithelium tissue. The thickness of the epithelium layer varies with the generation number of the conducting airways. The epithelium layer is followed by a sub-epithelium layer which is highly vascularized. Modeling the transfer of particles through the airway tissue to the systemic system should take in to account the diffusion of particles through these layers. Also mucus transport of the particles may be influencing the diffusion of the particles through the mucus layer which needs to be analyzed. Figure 1 represents a PBPK multilayer tissue model showing the transport and diffusion of particles. The mucus model can again be subdivided to gel layer and sol layer based on the viscosity, since the diffusion of particles depends on the medium. Based on the model shown in Fig.1, there are three interfaces namely air-mucus, mucus-epithelium, epithelium-sub-mucosa or blood.

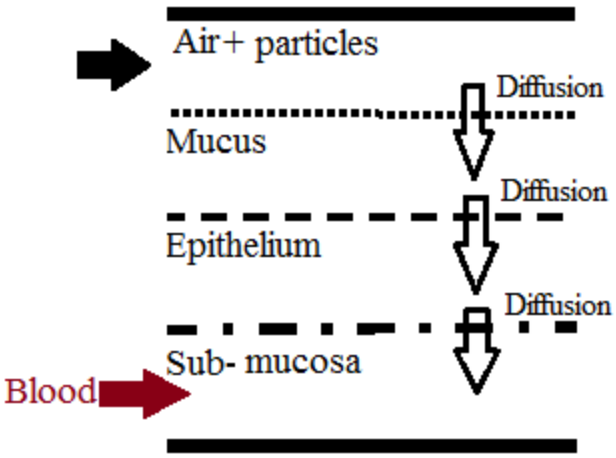

Fig. A3.1. PBPK multilayer tissue model showing the transport and diffusion of particles.

The major processes affecting the transfer of particles from air to blood system are convection and diffusion. Convection can be modeled using Navier-Stokes mass and momentum equations. Since the flow through the conducting airways is highly complicated, highly accurate turbulence models should be used to predict the transport of particles through air. The diffusion of the particles is always interconnected with the convection, which produces the concentration gradient leading to molecular diffusion. The diffusion of particles through the walls of the conducting airways can be modeled using mass transfer diffusion equation. Since the concentration of the particles in air, mucus, tissue and blood are interconnected, depends on the diffusion coefficients in each layer, the mass transfer diffusion equations should be solved simultaneously. Tian et al. (2010) reported that the absorption of vapors by the airway tissue and blood depends on the inhalation cycle and hence a transient simulation must be employed instead to steady state assumption.

The airflow can be modeled using the flowing equations.

$$\frac{\partial \bar{u}_i}{\partial x_i} = 0 \tag{A3.1}$$

$$\frac{\partial \bar{u}_i}{\partial t} + \bar{u}_j \frac{\partial \bar{u}_i}{\partial x_j} = -\frac{1}{\rho}\frac{\partial \hat{p}}{\partial x_i} + \frac{\partial}{\partial x_j}[(\nu + \nu_t)(\frac{\partial \bar{u}_i}{\partial x_j} + \frac{\partial \bar{u}_j}{\partial x_i})] \tag{A3.2}$$

Where $\bar{u}_i$ is the time-averaged velocity in three coordinate directions, i.e., i=1, 2, and 3, $\hat{p}$ is the modified time-averaged pressure term, ρ is the fluid density, and ν is the kinematic viscosity and ν_t is the turbulent viscosity.

Zhang et al., (2006), Zhang and Kleinstreuer (2011) and Zhang et al., (2012) have modeled the transport and deposition of organic compounds using a hybrid CFD-mass transfer model, incorporating the absorption of compounds by the mucus layer on the airway surface (Keyhani et al. 1997). Assuming that there are no particle reactions and metabolisms (the reaction terms are neglected), the mass transport equation representing diffusion of particles through mucus and tissue layers can be modeled using the following equations.

$$\frac{\partial C_a}{\partial t} + \frac{\partial}{\partial x_j}(u_j C_a) = \frac{\partial}{\partial x_j}[D_a \frac{\partial C_a}{\partial x_j}] \tag{A3.3}$$

$$\frac{\partial C_m}{\partial t} = D_m \frac{\partial^2 C_m}{\partial {x_j}^2} \tag{A3.4}$$

$$\frac{\partial C_e}{\partial t} = D_e \frac{\partial^2 C_e}{\partial {x_j}^2} \tag{A3.5}$$

Where C_a, C_m, C_e are the concentration of particles in air, mucus and epithelium and D_a, D_m, D_e are the diffusion coefficients in air, mucus and epithelium respectively. Chemical reactions and local metabolism in the respiratory tract can increase absorption by acting as a sink to drive the concentration gradient. Systemic metabolism can also drive the

concentration gradient in the respiratory tract tissues by determining the arterial blood concentration. But if the particles are less reactive and insoluble, the reactive terms can be neglected.

The sub-mucosal layer is highly vascularized. Also it has been reported that vapor particles have similar transfer rates through the layers of airway tissue (Schroeter et al., 2008). Hence further subdivision of the epithelial and sub-mucosal layers may not be required. Instead the blood flow clearance in the sub-mucosal layer can be modeled using appropriate boundary conditions. Schroeter et al., (2008) and Tian et al. (2010) used a zero concentration boundary condition at the sub-mucosal layer representing complete removal (perfect sink) of organic vapors by the blood circulation. Corley et al., (2012) used a zero flux boundary condition instead of zero concentration for the removal of acrolein by blood circulation.

Estimating the flux transfer at the interfaces is a major concern. The popular way of equating the fluxes at the interface has been found effective for vapor (or soluble particles), since the partition coefficients (air-mucus partition coefficient, mucus-tissue partition coefficient and tissue –blood partition coefficient) can be easily estimated. But for insoluble particles the data available regarding the partition coefficients are much less.

Frederick et al. (1998) used the hybrid CFD-PBPK model to simulate the absorption of acidic vapors by the nasal airway tissue and to estimate the regional tissue dose. They extrapolated the model from rodent nasal airway to human nasal airway. They used the CFD model to estimate the mass transfer coefficient which represents the diffusion of acid vapors through air-mucus interface. They used the concept of mass transfer resistance to calculate the overall mass transfer coefficient which combines the mass transfer coefficients through air and

mucus phase (Cohen-Hubal et al., 1997; Asgharian et al., 2011). The mucus phase mass transfer coefficient was derived from the diffusivity of the compound and thickness of the mucus layer as described by Bush et al. (1998). Similar hybrid CFD-PBPK models were found to accurately predict the absorption and diffusion of organic compounds (Kimbell et al., 1997; Kepler et al., 1998; Conolly et al., 2000; Georgieva et al., 2003). Since the vapors are highly reactive and soluble with tissue, most of the vapor models used a mass transfer reaction-diffusion equation with a Michaelis-Menten elimination term. Schroeter et al., (2008) developed a three layered hybrid CFD-PBPK model to predict the nasal dosimetry of inhaled acrolein. Following the article, Corley et al., (2012) used the model to compare the vapor dosimetry in rat, monkey and human nasal airway. Asgharian et al., (2011) proposed a transient vapor uptake model by simplifying the saturable elimination pathway model. Zhang et al., (2012) used the saturable elimination pathway model to predict the vapor deposition during cigarette smoke inhalation. Tian et al., (2010) developed a multi-layer tissue model, without the reaction terms, to predict the absorption of inhaled vapors in the conducting airways. They derived the analytical transient solutions for the mass transfer diffusion equations in the mucus and tissue layers. Since the reaction of particles is not considered in this model, this model can be used to predict the diffusion of insoluble particles through the airway tissue to the blood circulation system.

A.3.3 References

Cohen-Hubal, E. A., Schlosser, P. M., Conolly, R. B., and Kimbell, J. S. (1997). Comparison of inhaled formaldehyde dosimetry predictions with DNA–protein cross-link measurements in the rat nasal passages. Toxicol. Appl. Pharmacol. 143:47–55

Conolly, R. B., Lilly, P. D., and Kimbell, J. S. (2000). Simulation modeling of the tissue disposition of formaldehyde to predict nasal DNA–protein cross-links in Fischer 344 rats, rhesus monkeys, and humans. Environ. Health Perspect. 108(suppl. 5):919–924.

Corley, R. A., S. Kabilan, A. P. Kuprat, J. P. Carson, K. R. Minard, R. E. Jacob, C. Timchalk et al. (2012). Comparative Computational Modeling of Airflows and Vapor Dosimetry in the Respiratory Tracts of Rat, Monkey, and Human. Toxicological Sciences 128, no. 2: 500-516.

Frederick, C. B., Bush, M. L., Lomax, L. G., Black, K. A., Finch, L., Kimbell, J. S., Morgan, K. T., Subramaniam, R. P., Morris, J. B., and Ultman, J. S. (1998). Application of a hybrid computational fluid dynamics and physiologically based inhalation model for interspecies dosimetry extrapolation of acidic vapors in the upper airways. Toxicol. Appl. Pharmacol. 152:211–231.

Jayaraju S.T., Brouns M., Lacor C., Belkassem B., Verbanck S. (2008). Large eddy and detached eddy simulations of fluid flow and particle deposition in a human mouth-throat. J. Aerosol Sci. 39:862–75

Jin, H.H., Fan, J.R., Zeng, M.J., Cen, K.F. (2007). Large eddy simulation of inhaled particle deposition within the human upper respiratory tract. Journal of Aerosol Science 38, 257–268

Kepler, G. M., Richardson, R. B., Morgan, K. T., and Kimbell, J. S. (1998). Computer simulation of inspiratory nasal airflow and inhaled gas uptake in a rhesus monkey. Toxicol. Appl. Pharmacol. 150:1– 11.

Keyhani K, Scherer PW, Mozell MM. (1997). A numerical model of nasal odorant transport for the analysis of human olfaction. J Theor Biol 186:279–301.

Kimbell, J. S., Godo, M. N., Gross, E. A., Joyner, D. R., Richardson, R. B., and Morgan, K. T. (1997). Computer simulation of inspiratory airflow in all regions of the F344 rat nasal passages. Toxicol. Appl. Pharmacol. 145:388–398.

Lin, C.-L., Tawhai, M. H., McLennon, G., and Horrman, E. A. (2007). Characteristics of the Turbulent Laryngeal Jet and Its Effect on Airflow in the Human Intra-Thoracic Airways. Respir. Physiol. & Neurobiol. 157:295– 309.

Ma, B., and Lutchen, K. R. (2008). CFD Simulation of Aerosol Deposition in an Anatomically Based Human Large-Medium AirwayModel. Ann. Biomed. Engineer. 37:271–285.

Matida EA, Finlay WH, Lange CF, Grgic B. (2004). Improved numerical simulation of aerosol deposition in an idealized mouth-throat. J. Aerosol Sci. 35:1–19.

Matida, E.A., Finlay, W.H., Breuer, M., Lange, C.F. (2006). Improving prediction of aerosol deposition in an idealized mouth using large eddy simulation. Journal of Aerosol Medicine 19, 290–300.

Schroeter, J. D., J. S. Kimbell, E. A. Gross, G. A. Willson, D. C. Dorman, Y. M. Tan, and H. J. Clewell. (2008). Application of physiological computational fluid dynamics models to, predict interspecies nasal dosimetry of inhaled acrolein. Inhal. Toxicol. 20:227–243.

Stapleton, K.W., Guentsch, E., Hoskinson, M.K., Finlay,W.H. (2000). On the suitability of k−ε turbulence modeling for aerosol deposition in the mouth and throat: A comparison with experiment. Journal of Aerosol Science 31, 739–749.

Tian, G., and P. W. Longest. (2010). Transient absorption of inhaled vapors into a multilayer mucus–tissue–blood system. Ann. Biomed. Eng. 38:517–536.

Zhang Z., Kleinstreuer C., Feng Y.. (2012). Vapor deposition during cigarette smoke inhalation in a subject-specific human airway model. Journal of Aerosol Science, 53,:40–60

Zhang Z., Kleinstreuer C., (2011). Deposition of naphthalene and tetradecane vapors in models of the human respiratory system. Inhalation Toxicology, 23 (2011), pp. 44–57

Zhang Z., Kleinstreuer C., (2011). Laminar-to-turbulent fluid-nanoparticle dynamics simulations: model comparisons and nanoparticle-deposition applications. International Journal for Numerical Methods in Biomedical Engineering, 27 (2011), pp. 1930–1950

Zhang, Z., and C. Kleinstreuer. (2006). Transport and uptake of MTBE and ethanol vapors in a human upper airway model. Inhal. Toxicol. 18:169–184.

Zhang, Z., Kleinstreuer, C. (2003). Low-Reynolds-number turbulent flows in locally constricted conduits: a comparison study. AIAA Journal; 41:831–840.

GLOSSARY

Acinus - the region where gas exchange occurs.

Aerodynamic diameter - the diameter of a sphere with unit density that has aerodynamic behavior identical to that of the particle in question.

Alveolar macrophages - macrophages found in the pulmonary alveolus.

Alveoli - small balloon-like structures where oxygen exchange in the lungs takes place.

Asthma- is a chronic (long-term) lung disease that inflames and narrows the airways.

Bronchi - passage of airway in the respiratory tract that conducts air into the lungs.

Bronchioles – airways that connects bronchi to acinus.

CFPD – Computational Fluid Particle Dynamics.

Clearance – removal of particles from lung regions either by transporting or by migration of particles.

CMD – count mean diameter.

Cunningham slip correction factor - used to account for non-continuum effects when calculating the drag on small particles.

Cytotoxicity - toxic to cells.

Emphysema - disease of the lung tissue caused by destruction of structures feeding the alveoli.

Endocytosis - process by which cells absorb molecules by engulfing them.

Fibrosis- formation of excess fibrous connective tissue in an organ or tissue.

ICRP - International Commission on Radiological Protection.

Inflammation - complex biological response of vascular tissues to harmful stimuli, such as pathogens, damaged cells, or irritants.

Interstitial granuloma - tiny collection of immune cells known as macrophages.

Interstitial macrophages - macrophages move through interstitial spaces.

Larynx- connects the inferior part of the pharynx with the trachea.

Mucociliary transport or mucociliary escalation – non-immunological defense mechanism involving ciliary action and flow of mucus from bronchioles, through the bronchi and trachea to the larynx, by which particulate matter is removed from the respiratory tract.

Perihilar region - area of the lung around the hilum which includes the bronchus.

Phagocytosis - cellular process of engulfing solid particles by the cell membrane.

Pharynx - part of the throat situated immediately inferior to the mouth and nasal cavity.

Surfactant lining layer – liquid lining of the alveoli of the lungs which reduces the force needed to inflate the lungs and allows comfortable, quiet breathing.

Trachea- (windpipe) is a tube that connects the pharynx or larynx to the lungs.